LONDON'S GLOBAL UNIVERSITY

Nano- and Micro-structures for organic/hybrid photonics and optoelectronics

Valentina Robbiano

A dissertation submitted for the degree of Doctor of Philosophy

Department of Physics and Astronomy and London Centre for Nanotechnology

University College London

London, December 2016

I, Valentina Robbiano, confirm that the work presented in this thesis is my own. Where information has been derived from other sources and work which has formed part of jointly-authored publications has been used I confirm that this has been indicated in the thesis.

Supervisor: Prof. Franco Cacialli,

Department of Physics and Astronomy and London Centre for Nanotechnology, University College London

Second Supervisor: Dr. Ioannis Papakostantinou

Department of Electronic and Electrical Engineering, University College London

Acknowledgments

My research was funded by the European Commission Seventh Framework Program (FP7/2007-2013) Marie Curie Initial Training Network CONTEST under Grant agreement PITN-GA-2012-317488.

First I would like to thank Prof. Franco Cacialli for giving me the opportunity to work on this interesting project and for the guidance throughout my PhD. I would also like to acknowledge Dr. Ioannis Papakostantinou, my second supervisor, for his valuable input during the transfer viva and for the constructive feedbacks on this dissertation.

Another big thanks goes to the external collaborators that helped me a lot during these three years and to all the members of the CONTEST project. In particular, Prof. Paolo Lugli, Simone Colasanti, Engin Cagatay and Alaa Abdellah from TUM, for being so welcoming with me during my secondment there and for the good work done together; Prof. Giuseppe Barillaro, Lucanos Strambini and Salvatore Surdo from UNIPI, for letting me get in touch with the interesting world of silicon photonics, and Prof. Davide Comoretto from UNIGE, for the constant help in whatever is related to photonics.

The biggest thank goes to all my colleagues: Luca Santarelli, Ludovica Intilla, Giuseppe Paterno', Alessandro Minotto, Andrea Zampetti, Giulia Tregnago, Nico Seidler, Keith Fraser, Francesco Bausi, Giuseppe Carnicella, Tecla Arcidiacono and Gianfranco Cotella, to the MsC students, and to everyone who has worked in the group: Emanuele Marino, Giovanni Polito, Tiziana Fiore, Shimpei Goto, Martina Dianetti. I truly enjoyed my time with you at UCL. I would also like to express my deep gratitude to Prof. Shabbir Mian (Apollo) for the help and all the scientific stuff I learnt from him.

I thank my family for the support they give me every day of my life. This is dedicated to all of you.

Last, but not least, I want to thank who has been wonderful with his continuous help and support. Everything is perfect when you are by my side.

Abstract

In this work I present nano- and micro-patterning techniques useful especially in photonics and optoelectronics. In fact, these structures give the possibility to tailor the photophysical and electrical properties of organic and hybrid active materials, spanning from well-known conjugated polymers, to organo-halaide perovskite that nowadays are gaining a lot of interest due to their high performances in photovoltaic devices.

The first part is dedicated to the study of the optical properties of conjugated polymers embedded/infiltrated into photonic crystals. In particular, I will show how it is possible to prepare these composite materials and tune their optical properties. The preparation technique has been improved, leading to a promising simple, widely available and low cost preparation of both organic and hybrid photonic structures. The optical properties have been investigated via both steady-state and time-resolved optical techniques. I believe that results obtained are a valuable feedback for future application such as low-threshold optically pumped lasers.

In the second part, I will present the application of nanostructured layers in optoelectronic devices. I will show how nanostructured architectures are used to obtain efficient organo-halide perovskite solar cells. This nanostructure induced an increased light absorption due to a controlled light scattering and a controlled microscopic morphology of perovskite films, opening up a wide range of possible investigations, from charge transport optimization to optical enhancements for photovoltaic, light emitting and lasing devices.

Finally, I’ve studied the preparation of nanostructured conductive thin films for flexible transparent electrodes suitable for optoelectronic devices. Furthermore, I’ve observed that by introducing a layer of a polyamine derivative it has been possible to tune the work function of these electrodes, therefore changing (lowering) the injection barriers for charge at the interface between the semiconductor and the electrode.

Contents

List of figures 6

List of tables 13

List of publications 14

Introduction 16

Thesis overview 17

1 – Nano- and Micro-structures 19

1.1 Photonic Crystals 19

1.1.1 Photonic band formation 19

1.1.2 Scale Invariance of Maxwell’s equation 24

1.1.3 Bragg-Snell’s Law 25

1.1.4 Density of states 27

1.2 Transparent and conductive nanostructured thin films 29

1.2.1 CNTs 29

1.2.2 Metal nanostructures 31

1.3 Nano- micro-structuring techniques 34

1.3.1 Top-down 34

1.3.2 Bottom-up 36

2 – Organic semiconductors and Organo-halide perovskite 37

2.1 Electric Properties 37

2.1.1 Semiconducting behaviour and charge transport 40

2.1.2 Work function 41

2.2 Optical properties 45

2.2.1 Photoluminescence properties and energy transfer 47

2.2.2 Time correlated single photon counting (TCSPC) 50

2.3 Organo-Lead Halide Perovskite 52

2.3.1 Perovskite-based photovoltaic devices 53

3 – Polymer-silicon hybrid photonic structures 58

3.1 Hybrid photonic structures for light emission 59
3.2 Experimental details 61
3.3 Morphological characterization 63
3.4 Optical characterization 65
3.5 Conclusion 72

4 – Spectroscopy of synthetic opals 73

4.1 Synthetic opals 73
4.2 Polyrotaxanes 77
4.3 Experimental details 78
4.4 Bare opals investigation 80
4.5 Infiltrated opals investigation 85
4.6 Conclusion 88

5 – Nanostructured titania for efficient perovskite solar cells 89

5.1 Nanostructures for optoelectronic 90
5.2 Experimental details 91
5.3 Morphological and optical characterization 93
5.4 Photovoltaic devices 98
5.5 Conclusion 102

6 – Transparent electrodes: preparation, characterization and work-function engineering 103

6.1 Transparent conductive electrodes 104
6.2 Experimental details 105
6.3 Electrical and optical characterization 107
6.4 Temperature behaviour 110
6.5 Work function engineering 113
6.6 Conclusion 116

Conclusion and Outlooks 117

References 119

List of figures

1.1 Schemes of 1D, 2D and 3D PhCs, Reproduced from ref. [16].

1.2 Dispersion relations for free electrons and inside a periodic potential (top) and for photons in vacuum and inside a periodic dielectric (bottom), taken from ref. [3].

1.3 Scheme of the dispersion relation of a homogeneous medium (dashed line) and a 1D photonic crystal (solid line). Reproduced from ref. [3].

1.4 Scheme of the diffraction process of two incident beams in a one-dimensional crystal.

1.5 Scheme of the diffraction model of one-dimensional photonic crystal.

1.6 Schematic illustration of the density of states of the radiation field in free space (dashed blue line) and (a) in a photonic crystal featuring a stop-band (red line) and (b) in a photonic crystal featuring a full band-gap (green line).

1.7 Schematic illustration of a SWCNT (a) and (b) of a MWCNT, with their typical dimensions. Taken from ref. [28].

1.8 (a) Sketch of an electrophoretic cell and photos of SWCNTs solution in before and 4, 16, and 24 h after the application of 30V (taken from ref. [37]) and (b) Separation of semiconducting SWCTs starting from a mixed metallic semiconducting solution obtained via ultracentrifugation method. The separation can be observed both in the photo and in the absorbance spectra. Adapted from ref. [38].

1.9 Average optical transmittance in the visible range as function of the t electrical resistivity for Cr and Ni films compared with ITO anneal and not annealed. Reproduced from ref. [45].

1.10 (a) Sketch of the sample geometry, lines in the network are not to scale, (b) SEM image of a network showing the high uniformity over a large area (inset) individual Ag wires with a scale bar of 500 nm., (c) SEM image showing the contact area of the wire network and the electrical contact pads. (d) AFM image network shown in (b) (inset) extracted line profile. Image taken from [47].

1.11 SEM images showing AgNW mesh deposited via drop-casting (a) and spin-coating (b). Taken from ref. [50] and ref. [53].

1.12 A scanning electron micrograph of the micro-bull obtained by photopolymerisation, the scale bar is 2 micrometres long. Taken from ref. [64].

1.13 (a) A scanning electron micrograph of an electrochemical micromachined microsystem (MEMS) taken from ref. [70] and (b) a porous silicon microcavity taken from ref. [71].

1.14 (a) TEM cross-sectional image of an L-b-L assembled multilayer. Adapted from ref. [75] (b) image of a polymer inverse opal, revealing the optimal replication process (inset) detail of one hollow sphere, taken from ref. [83].

2.1 (a) sp^3 hybridisation, where 4 σ bonds (in blue) are formed with an angle of 109.5° between the bonding orbitals (b) sp^2 hybridisation shows a trigonal-planar geometry with an angle of 120° between the three σ bonds, the remaining π bonds (in green) are perpendicular to the σ ones (c) in the sp hybridisation there are only two σ bonds with an angle of 180° between them.

2.2 (a) Scheme of the sp^2 hybridisation in an ethylene molecule (b) Scheme of the energy splitting of 2p orbitals into a bonding and an antibonding orbital. Increasing the CH_2 units leads to an increase in the degeneration of energy levels resulting in two quasi-continuous bands, namely the highest occupied molecular orbital (HOMO) and the lowest unoccupied molecular orbital (LUMO).

2.3 (a) An undimerised polyacetylene chain (with a complete delocalisation of the electron wavefunction) and equal distance *a* between the atoms of the chain. The corresponding band structure shows that the band is half-filled up to the Fermi energy (EF) (b) Peierls dimerisation of polyacetylene, where the distance between the atoms of the chain is different if it is a single or double bond. The corresponding band structure shows the formation of an energy gap at the edge of the Brillouin zone.

2.4 Electronic energy level diagram of a solid showing the various energies relevant to the definition of the work function.

2.5 Orientation of the dipoles induced by the adsorbate: (a) the adsorbate is polarised with the positive pole towards the vacuum side causing a decrease in ϕ and (b) with the negative pole pointing towards the vacuum side, causing am increase in ϕ.

2.6 Electric circuit of the Zisman's KP set-up.

2.7 Jablonski diagram illustrating the different electronic and vibrational levels in an organic molecule and, the different optical transitions.

2.8 Scheme of Morse potential energy curves with vibrational energy levels indicated for each state. It illustrates the Franck-Condon principle and the origin of the symmetrical shape of absorption and emission spectra in organic molecules. The difference between the maxima of the absorption and fluorescence spectra is the Stokes' shift.

2.9 Schematic illustration of H- and J-aggregates (exemplified for a dimer) for a π-conjugated molecule (monomer). The ground state of the monomer is indicated as E_0 and lowest excited state as E_1. Depending on the orientation of the interacting dipoles, E_1 splits in two different ways: (a) for a head-to-tail coupling (H-aggregate), the parallel orientation will be at higher energy, while the energy of the antiparallel orientation will be lower than the monomer level E1; (b) for cofacial coupling (J-aggregates), the dipole is coupled in one dimension, with the same oriented at lower energy and the opposite oriented at higher energy than the monomer level E_1. Full arrows depict allowed (strong) transitions, and dashed arrows forbidden (or weak) ones.

2.10 Electronics scheme for TCSPC, taken from [93].

2.11 Three-dimensional schematic representation of perovskite structure ABX_3 (A = CH_3NH_3,B = Pb, and X = Cl, I, Br), taken from [97].

2.12 Equivalent electric circuit for a real solar cell.

2.13 J-V curve (in red) of a real device. The operating point with the maxima power is identified by pair (Jmax; Vmax).

2.14 (a) Schematic mesostructured device architecture (on the left) and cross-sectional SEM image of the device structure, taken from ref. [98].The transparent electrode is the fluorinated-tin oxide (FTO), on top of it there is a compact layer of titania (TiO_2) and the mesoporous oxide. The perovskite is the photoactive layers, and it is infiltrated into the mesoporous scaffold. Than the structure is capped with the hole transporter (in this case it is the spiro-OMeTAD) and the cathode. (b) Cross-sectional SEM of a planar heterojunction device. In particular this is the inverted architecture, with the transparent cathode (ITO) in the bottom. Taken from ref. [104].

2.15 Schematic energy diagram of a solar cell in direct configuration, using FTO as transparent electrode, TiO_2 as ETL, Organo-Lead Perovskite ($(CH_3NH_3)PbI_3$) as active layer, Spiro-OMeOTAD as HTL and a generic metallic contact.

3.1 TEM/STEM images of rugate filter with reference peak (After infiltration) at 515 nm. (a) Bright-field TEM image of the rugate filter (inset: photo of the same rugate filter). (b) bright-field STEM overview image of the PhC (c) High Angle Annular Dark-Field zoom of the internal structure (d) SEM image of a FIB-milled cross-section of the rugate filter at 515 nm detailing the pore structure, with pore sizes on the order of 50 nm or so. Bright areas on the edge of the solid Si pillars are associated with regions of more intense charging, and are thus assigned as rich in oxidised silicon, with a typical thickness of 10 nm or so.

3.2 2D-FFT transform (inset: frequency profile extracted from the 2D-FFT, the distance between the lines is found to be 6.67 μm-1).

3.3 Bright-field TEM images taken at 12000 magnifications with 0.5 s exposure in the top and bottom part of the rugate filter.

3.4 Reflectance spectra of the tuned (a) and detuned (b) rugate filter before (red line) and after (blue line) the oxidation process.

3.5 (a) PL spectrum of a neat film of F8BT on a compact silicon substrate, and (b and c) reflectance spectra for the PhCs before (blue) and after polymer infiltration (red). The infiltration leads to a red-shift of the photonic stop-band (and thus of the reflectance peak) of about 12±1 nm. Note that the vertical scales for (b) and (c) are different, i.e 40% and 100% reflectance, respectively. Inset: cartoon illustrating the inferred cross-section of the rugate filter (D is the inter-planar spacing determined by the period of the anodic etching current); the polymer layer is not filling the pores of the rugate filters, but there is just a layer on the walls of the cavities (see main text for discussion). The structure of the sample used to measure the F8BT PL is also shown.

3.6 (a) PL spectra (solid lines) collected at different incidence angle (from 0° to25° with step of 5°) of the exciting beam for F8BT infiltrated into the tuned PhC and at 0° for the F8BT infiltrated into the detuned PhC (dashed line). I used a CW laser, emitting at 405 nm, as excitation source. I can observe the PL peak dispersion moving from 518 nm at 0° to 506

nm at 25°. (b) Ratio between the PL spectra from the tuned and detuned PhC at different angles, as in (a) above.

3.7 Radiative decay of the F8BT PL measured by time-correlated single-photon counting, TCSPC (371 nm excitation) and recorded either within the stop-band (528 nm, top panel) and at the high-energy edge (518 nm, bottom panel) for a neat F8BT film on Si, as well as for F8BT infiltrated into the tuned and detuned filters, as indicated in the plots legends.

4.1 SEM image of the opal structure (left) and photo of opals made with different microspheres diameter (right), the diameter (in nm) is indicated below the opals. The reflected color changes as function of the dimension, according to Bragg-Snell's law.

4.2 Right: photonic band structure of an opal made with dielectric spheres ($\varepsilon=13$). The stop-band is present along certain crystallographic directions (e.g. the Γ-L direction) but not for every direction, thus it is not a complete photonic band-gap. Inset: FCC lattice structure; taken from ref. [3]. Left: symmetry point in the Brillouin zone for a FCC lattice; taken from ref. [137].

4.3 Photonic band structures and corresponding DOS and reflectance spectrum at normal incidence. Adapted from ref. [137].

4.4 Density of states at different angles and for different orientations. Taken from ref. [137].

4.5 Chemical structures of the cyclodextrin-threaded conjugated polyrotaxanes with poly(4,4'-diphenylene-vinylene) (PDV.Li) core with naphthalene stoppers (average number of repeat units n = 10) and its optical properties (photoluminescence quantum efficiency, PLQE, and OLES external quantum efficiency, EQE) as function of the threading ratio. Reproduced from ref. [157].

4.6 (a) Scheme of the vertical deposition technique used to prepare the opals and (b) the experimental set-up.

4.7 SEM micrographs of an opal film incorporating PDV.Li$\subset\beta$-CD: (a) cryo-cleaved wall surface showing the internal structure of the opal, (b) film cross-section. Strong contrast between the sphere and the interstices is observed, confirming that the latter are not filled up by the conjugated polyelectrolytes (the density of the conjugated moiety and of the spheres being comparable). Inset: Photography of the diffraction pattern from the opals. Images were collected using the SEM mode of a dual beam Carl Zeiss XB1540 "Cross-Beam" focussed-ion-beam microscope and the cross section was obtained via cryo-cleaving an opal film. Adapted from ref. [110].

4.8 Reflectance spectra collected from opal made with microspheres with a diameter of (a) 200 nm, (b) 220 nm, (c) 370 nm and (d) 430 nm. Inset: scheme of the mapping.

4.9 Reflectance (blue line) and transmittance (red line) spectra of an opal prepared with microspheres diameter = 220 nm.

4.10 Angle-resolved transmittance spectra for the opal made with microspheres diameter 430 nm for (a) p- and (b) s-polarised light.

4.11 Colored contour-plot of the transmittance spectra for the opal made with microspheres diameter 430 nm for (a) p- and (b) s-polarised light. Transmittance percentage is shown in color scale.

4.12 Transmittance spectra of the opals as a function of incidence angle for (a) 200 nm, (b) 220 nm and (c) 370 nm microspheres diameter. The Bragg-Snell law analysis of the spectra appears in (d) where the lines are linear regressions. Taken from ref. [146].

4.13 Reflectance spectra of the bare opal made with microsphere diameter 200 nm (red) and infiltrated (black) with the polyrotaxanes. There is no difference between the spectral positions of the reflectance peaks.

4.14 Normalized reflectance spectra (coloured lines) of the bare opals and normalized PL emission (black solid line) of polyrotaxanes inside a thermally annealed opal and of a spin-coated thin film (black dashed line). The annealing was necessary to keep the material chemical properties but avoiding the photonic contribution.

4.15 PL (black), reflectance (red) and transmittance (green) spectra collected at normal incidence for spray-coated opals made with beads having diameter 200 nm (a) and 430 nm (b).

4.16 (a) Angle resolved PL emission for infiltrated opals made with microspheres diameter 200 nm (a). The enhancement and suppression effects depend on the incident angle. This effect can be better appreciated in (b) where I plot the PL ratio between the thin film and the photonic structure at various angles.

5.1 (a) Scheme of the device prepared with the ordered nanostructure, (b) with the "standard" titania mesoporous scaffold, and (c) with the perovskite coated on top of the compact titania layer.

5.2 (a) Preparation steps for patterned titania photonic scaffolds: (1) PS microspheres monolayer is obtained via self-assembling and transferred onto the FTO/c-TiO2, (2) drop-casting of the oxide precursor solution onto the PS microsferes template. Complete filling of the gaps of the monolayer is obtained leaving the samples drying overnight, (3) titania microspheres replica structure forms after a three-steps annealing described in the experimental section. AFM images (scalebars are 3 μm) show: (b) a typical highly-ordered monolayer of PS microspheres with a diameter of 370 nm, and the calcinated TiO2 monolayers obtained from PS microspheres with various diameter, in particualr: (c) 220 nm (inse in blue box: a zoomed images on the layer, the scale bar is 1 μm), (d) 270 nm and (e) 430 nm.

5.3 (a) Ar-milled XPS profile of the microspheres titania layer onto FTO/cTiO2 substrates. Dr. Tiziana Fiore from University of Palermo for the measurement is thankfully acknowledged for these measurements. (b) FIB-milled SEM micrograph (scalebar is 400 nm) of the titania hollow spheres monolayer.

5.4 XRD spectra of the titania nanostructures and the titania mesoporous layer sintered onto FTO substrates and of the bare FTO. Anatase peaks of TiO2: 2 theta 25.37°, fluorine-doped tin oxide (FTO) substrate peaks: 2 theta = 26.4°, 37.6°.These measurements were taken by G. M. Paterno’ from our group.

5.5 Transmittance spectra of the titania structure synthesized onto the FTO substrates.

5.6 AFM (tapping mode) images of the perovskite layer synthesized onto the nanostructured titania starting from (a) spheres having a diameter of 370 nm, (b) the mesoporous titania layer and (c) on compact titania layer.

5.7 XRD spectra of the perovskite layer sintered onto FTO/cTiO2 (black line), FTO/cTiO2/mesoporous (red line), and FTO/cTiO2/nanostructure (blue line for the microspheres with 370 nm diameter, green line for the microspheres with 430 nm diameter) substrates. Broader peaks (full width half maximum, FWHM, inset) for the perovskite prepared onto the mesoporous and nanostructured films. These measurements were taken by G. M. Paterno' from our group.

5.8 Electrical characterization and device performance analysis: (a) J−V curves of the devices both under illumination (darker curves) and in dark (lighter curves). The arrows highlight the enhanced Jsc and Voc obtained for the cells prepared with the nanostructured titania layer. (b-e) Box-plot of the devices performance: (b) power conversion efficiency (PCE), (c) Fill Factor (FF), (d) open circuit voltage (Voc), and (e) short-circuit current density (Jsc).

5.9 (a-d) One-diode model fitting (R2>0.97) for each titania scaffolds. (e) Series resistance (f) and shunt resistance for devices obtained from the fitting of the current density – voltage curve.

5.10 Hysteresis measurement of FTO/c-TiO2/370nm drop/Perovskite/Spiro-OmeTAD/Au.

6.1 (a) Spray-coating set-up and (b) schematic illustration of the components.

6.2 (a) Transmittance spectra (solid lines) for the various films deposited onto soda lime glass slides compared to the transmittance of the bare glass slide (black dashed line) and ITO onto glass (red dotted line). (b) Sheet resistance measured using a four points probe for the various thin films.

6.3 (a-d) Atomic force microscopy topographies (tapping mode) of (a) AgNWs, (b) 5x AgNWs-SWCNTs, (c) 7x AgNWs-SWCNTs, (d) SWCNTs thin films. Height scale has been kept equal for each sample. (e) Roughness of the films (included for an ITO film), that represents the standard deviation of surface heights calculated from AFM data and (f) Peak-to-valley distances for the thin films.

6.4 (a) Transmittance spectra for the films deposited onto soda lime glass slides (blue and light blue lines) and PET foils (red and light red lines) for the two thickness tested. (b) Sheet resistance measured using a four points probe for films prepared onto soda lime glass slide and PET foil. The value obtained for the film onto glass slide (for the thick sample) is comparable to previous results, thus suggesting an optimal reproducibility of the preparation method. Adapted from ref. [189].

6.5 AFM images of the CNTs networks with increasing densities, namely 12 CNT/μm^2, 18 CNT/μm^2 and 24 CNT/μm^2. Adapted from ref. [32].

6.6 Measured (circles) and calculated (solid lines) relative resistance (defined as the ratio between the initial resistance and the measured one at different temperature) of three CNTs networks with different densities. The resistance decreases by increasing the temperature for the denser networks. Instead, for the network with 12 CNTs/µm2 we observe the presence of a minimum in the resistance. I thank Simone Colasanti for the simulation. Taken from ref. [32].

6.7 Temperature dependency of the resistance for a network with 16 CNTs/µm2 measured and simulated in air (red) and under nitrogen (blue). The different behavior of the network could be attributed to a different oxygen desorption from the CNTs in the two environments. I thank Simone Colasanti for the simulation. Taken from ref. [32].

6.8 WF measured (a) on the thin films before (black circle) and after different PEI deposition and/or thermal treatments. (b) Difference between the WF after each treatment and the pristine values. Inset: PEI chemical structure.

List of tables

3.1 Temporal decay constants (τ1, τ2) extracted from least square fits of the PL decay curves with their relative weight (I1, I2).

4.1 Thickness of the opals made with different micorspheres diameters.

List of publications

1 Valentina Robbiano, Alaa Abdellah, Luca Santarelli, Aniello Falco, Sara El-Molla, Lyubov V Titova, David N Purschke, Frank Hegmann, Franco Cacialli, Paolo Lugli, *"Analysis of sprayed Carbon nanotube films on rigid and flexible substrates"*, **Proceeding of Nanotechnology (IEEE-NANO)**, 650-654, (2014).

2 Valentina Robbiano, Francesco Di Stasio, Salvatore Surdo, Shabbir Mian, Giuseppe Barillaro, Franco Cacialli, *"Hybrid-Organic Photonic Structures for Light Emission Modification"*, in Organic and Hybrid Photonic Crystals, **Springer International Publishing**, 339-358 (2015).

3 Giovanni Polito, Salvatore Surdo, Valentina Robbiano, Giulia Tregnago, Franco Cacialli, Giuseppe Barillaro, *"Two-Dimensional Array of Photoluminescent Light Sources by Selective Integration of Conjugated Luminescent Polymers into Three-Dimensional Silicon Microstructures"*, **Advanced Optical Materials**, 1: 894–898 (2013).

4 Francesco Di Stasio, Luca Berti, Shane O. McDonnell, Valentina Robbiano, Harry L Anderson, Davide Comoretto, Franco Cacialli, *"Fluorescent polystyrene photonic crystals self-assembled with water-soluble conjugated polyrotaxanes"*, **APL Materials**, 1, 042116 (2013).

5 Simone Colasanti, Valentina Robbiano, Florin C. Loghin, Ahmed Abdelhalim, Vijay D. Bhatt, Alaa Abdellah, Franco Cacialli, Paolo Lugli, "*Experimental and Computational Study on the Temperature Behavior of CNT Networks*", **IEEE Transactions on Nanotechnology**, 15 (2016) 171-178.

6 Simone Colasanti, Florin C. Loghin, Ahmed Abdelhalim, Vijay D. Bhatt, Alaa Abdellah., Paolo Lugli, Valentina Robbiano, Franco Cacialli "*Experimental and computational study on the temperature behavior of CNT networks*", **Proceeding of Nanotechnology (IEEE-NANO)**, 1445-1448. (2015).

7 Gina Mayonado, Shabbir Mian, Valentina Robbiano, Franco Cacialli, "*Investigation of the Bragg-Snell law In photonic crystals*", **Proceeding of BFY Conference**, 60-63, (2015).

8 Giuseppe Barillaro, Giovanni Polito, Salvatore Surdo, Valentina Robbiano, Giulia Tregnago, Franco Cacialli, *"Synergic Integration of Conjugated Luminescent Polymers and Three-Dimensional Silicon Microstructures for the Effective Synthesis of Photoluminescent Light Source Arrays"*, in Sensors, **Springer International Publishing**, 319: 243-247 (2015).

9 Luca Nucara, Vincenzo Piazza, Francesco Greco,Valentina Robbiano, Valentina Cappello, Mauro Gemmi, Franco Cacialli, Virgilio Mattoli, *"Ionic Strength Responsive Sulfonated Polystyrene Opals*", **accepted to ACS Applied Material & Interfaces**.

10 Giuseppe M. Paternò, Valentina Robbiano, Keith J. Fraser, Christopher Frost, Victoria García Sakai, Franco Cacialli, "*Neutron Radiation Tolerance of Two Benchmark Thiophene-Based Conjugated Polymers: the Importance of Crystallinity for Organic Avionics*", **accepted to Scientific Reports**.

11 Valentina Robbiano, Salvatore Surdo, Giancarlo Canazza, G. Mattia Lazzerini, Shabbir Mian, Davide Comoretto, Giuseppe Barillaro, Franco Cacialli, *"C-Si hybrid photonic structures by infiltration of conjugated polymers into porous silicon rugate filters"*, **in preparation**.

12 Valentina Robbiano, Giuseppe M. Paternò, Giovanni F. Cotella, Tiziana Fiore, Martina Dianetti, Francesca Brunetti, Bruno Pignataro, Henry J. Snaith, F. Cacialli, *"Nanostructured titania for efficient perovskite solar cells"*, **in preparation**.

Introduction

In the last 30 years, there has been an increasing interest in the development of novel micro- and nano-structure to control the interaction between light and matter, as well as to exploit novel optical and electrical properties. The aim of this thesis is the investigation of functional nanostructures for optoelectronic devices. One important class of nano-structure are the photonic crystals.

The concept of a photonic crystal (PhC) was introduced in 1987 with the independent studies of Yablonovitch [1] and John [2] on the inhibition of the spontaneous emission and light localization effects. These relate to structures whose periodicity in refractive index would enable to control, suppress, or enhance the propagation of photons, in analogy with the already well-established possibility to control electron propagation in “electronic” crystals, in which the periodicity of the electronic potential results in allowed and forbidden energy bands for the electrons. As well-described by Joannopolous and collaborators in their book [3], this is due to the possibility to re-write Maxwell equations in terms of a single master equation, in which the dielectric function plays a similar role to the potential in Schrödinger's equation.

The spectral position of the photonic gap can thus be modulated by varying two parameters: the materials of the components of refractive index and the pitch of the dielectric pattern. The materials used to create this type of structures can be both inorganic and organic. In the past years, the potential of these technologies has been considered with increasing attention from academia, industry and institutions that aim to develop a new technology based on photonic nanostructures for the exchange and processing of optical signals instead of electrical.

Indeed, the field of nano-structures and photonic crystals has then developed in a variety of directions, often dictated by the hurdles of fabrication of structures whose periodicity needs to be on the same lengthscale as that of the wavelength of the light one desires to control. In fact, they exhibit a variety of properties that can be exploited in a many optoelectronics applications, such as optical fibres [4], sensors [5], solar cells [6], light-emitting diodes [7] and lasers [8].

Conjugated semiconducting polymers have been widely used as active materials in all these applications. This is mainly due to their versatile processing, wide colour tuneability (from near-infrared (NIR) to near ultraviolet (UV)), high solid-state photoluminescence efficiency and strong optical absorption (up to ~10^5 cm^{-1}) [9, 10]. Since the discovery of their electrical conductivity in 1977 [11], they have attracted increasing attention due to interesting optoelectronics properties and processing advantages for the realization of optoelectronic devices such as light-emitting diodes [12], and photovoltaic devices [13].

The fundamental optical and electrical properties of organic semiconductors do not derive from the crystal structures, as for inorganic semiconductors, but they arise from the energy levels of the molecules that form the polymers chain and their intermolecular interactions. This fundamental difference is the main advantage of the organic systems compared to inorganic ones, for novel applications in the field of optoelectronics. In fact, the optoelectronic properties of the organic semiconductors can be simply tailored by molecular design, obtaining the desired electrical and optical properties.

More recently, organo-halide perovskite, have attracted great interest by obtaining in a short time span significant increase in the power conversion efficiency (PCE) of photovoltaics devices [14]. In fact, this metallo-organic system has demonstrated huge potential, joining the good optoelectronic properties of metals to the ease of fabrication typical of organic materials [15].

Thesis overview

The aim of the project is to prepare and characterise novel nano- and micro-structured architectures using different techniques and to assess their potential for being implemented into optoelectronic devices and components. As will be shown in the following chapters, these structures show optical and electrical properties which are significantly different from bulk materials, giving a new insight on how the nanoscale ordering affects their physical properties.

This thesis is divided into six chapters. The first two chapters give a general introduction on nano- and micro-structures and organic-hybrid semiconductors, the experimental techniques used and their applications in optoelectronic devices. The description and discussion of experimental results are presented in the four following chapters. Brief descriptions of the content of these chapters are given as follows:

In Chapter 3, I present an example of hybrid one-dimension photonic crystal, specifically silicon rugate filters infiltrated with a luminescent polymer. I characterise their internal structure and their optical properties.

In Chapter 4, the optical properties of synthetic opals, a particular class of three-dimension photonic crystals, are shown. Such structures enable emission modification of a supramolecular engineered conjugated polymer self-assembled inside them.

In Chapter 5 I present how it is possible to improve the efficiency of organo-halide perovskite solar-cells using colloidal lithography to enhance light-trapping and boost perovskite crystallization.

In Chapter 6, I show the morphological, electrical and optical characteristics of carbon nanotubes and silver nanowires thin films obtained using spray-coating deposition, which can be exploited as transparent conductive electrodes. Furthermore, I show how it is possible to tune their work function to lower the injection barrier at electrode/active layer interfaces in optoelectronic devices.

Finally, a summary of the results obtained as well as an outlook on future work is given.

Chapter 1

Nano- and Micro-structures

In this chapter I will present two categories of nano- and microstructures suitable for light and charge managing: photonic crystals (PhCs) and nanostructured conductive thin films. In the first part, the focus is given to photonic crystals and their optical properties. PhCs are functional materials that can provide a variety of optical effects ranging from optical switching to the modification of the emission spectra of active materials. In the second part I will discuss the fundamental properties of nanostructured material suitable for transparent conductive electrodes. These structures, widely applied in optoelectronic and electrochemical devices, need to combine high electrical conductivity and high optical transparency in the visible spectrum.

1.1 Photonic Crystals

1.1.1 Photonic band formation

Photonic crystals are composite materials made by media with different dielectric function (ε) or refractive index (n), periodically ordered in 1, 2 or 3 dimension (Fig. 1.1). The path width of such structures is comparable to UV-Vis-NIR wavelengths[3]. The definition of photonic crystal was introduced in 1987, with the pioneering and independent studies of Yablonovitch [1] and John [2] on the inhibition of the spontaneous emission and on the localization of the light. This stimulated early research on synthetic photonic crystals.

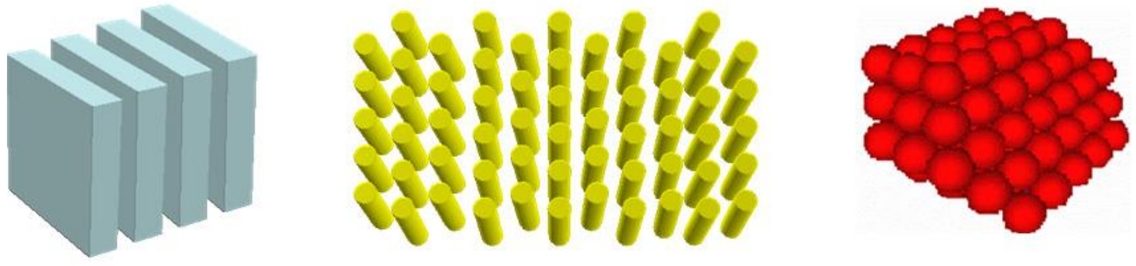

Figure 1.1 Schemes of 1D, 2D and 3D PhCs, Reproduced from ref [16].

The dielectric periodic pattern of the PhC behaves for the photons similarly to the periodic potential in a semiconductor for electrons. In fact it modifies the linear dispersion relation of the photon, (Fig. 1.2) generating frequencies band for which the propagation of light through the crystal is inhibited (photonic stop-band) and regions where the propagation of light is allowed (photonic bands) (Fig. 1.2).

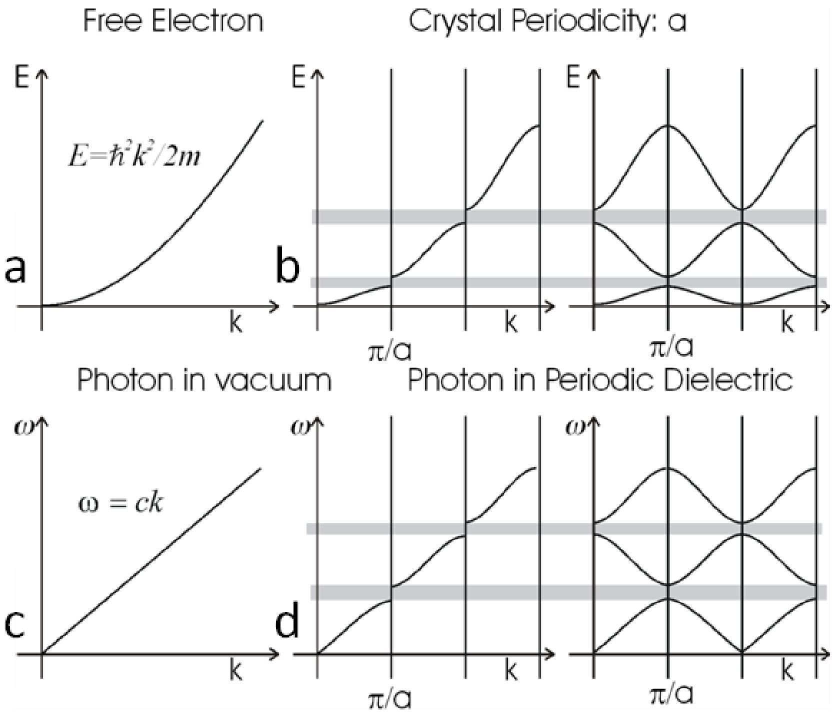

Figure 1.2 Dispersion relations for free electrons and inside a periodic potential (top) and for photons in vacuum and inside a periodic dielectric (bottom), taken from ref. [3].

To study the optical properties of a photonic crystal one should describe and solve the propagation of the electromagnetic radiation into a medium with a periodic dielectric constant ($\varepsilon\,(\mathbf{r}) = \varepsilon\,(\mathbf{r}+\mathbf{R})$, where $\mathbf{R}$ is the PhC periodicity). In this way it is possible to identify, as function of the dielectric parameters and geometry of the crystal itself, the permitted and prohibited modes.

This problem can be solved by means of Maxwell's equations:

$$\nabla \cdot \mathbf{B} = 0 \qquad \nabla \times \mathbf{E} + \frac{1}{c}\frac{\partial \mathbf{B}}{\partial t} = 0 \tag{1}$$

$$\nabla \cdot \mathbf{D} = 4\pi\rho \qquad \nabla \times \mathbf{H} - \frac{1}{c}\frac{\partial \mathbf{D}}{\partial t} = \frac{4\pi}{c}\mathbf{J}$$

As we are dealing with dielectric materials, Maxwell's equations can be simplified by making the following assumptions:

- There are no currents or free charges and the media are not magnetic (ρ=0, **J**=0, and μ=0, so **B**=**H**);
- We approximate the electric field in the linear regime: $\mathbf{D}(\mathbf{r}) = \varepsilon(\mathbf{r})\mathbf{E}(\mathbf{r})$);
- The material is macroscopic and isotropic, so $\varepsilon(\mathbf{r},\omega)$ is a scalar dielectric function;
- Any explicit frequency dependence could be ignored $\varepsilon(\mathbf{r},\omega) = \varepsilon(\mathbf{r})$;
- $\varepsilon(\mathbf{r})$ could be considered purely real and positive, ignoring any absorption effects.

Considering the linearity of Maxwell's equation, it is possible to separate the time and spatial dependence of $\mathbf{E}$ and $\mathbf{H}$ by expanding them in a set of harmonic modes at angular frequency (ω).

In this way one obtains:

$$\nabla \cdot \mathbf{H}(\mathbf{r}) = 0 \text{ and } \nabla \cdot \mathbf{D}(\mathbf{r}) = 0 \tag{2}$$

$$\nabla \times \left(\frac{1}{\varepsilon(\mathbf{r})}\nabla\times\mathbf{H}(\mathbf{r})\right) = \left(\frac{\omega}{c}\right)^2 \mathbf{H}(\mathbf{r}) \tag{3}$$

The first equations (2) indicate that the electromagnetic waves are transverse, i.e. the field oscillates in a plane orthogonal to the propagation direction. That means, if we have a plane wave $\mathbf{H}(\mathbf{r}) = \boldsymbol{a}e^{(i\boldsymbol{k}\cdot\mathbf{r})}$, with $\boldsymbol{k}$ wave-vector, Eq. 2 requires that $\boldsymbol{a} \cdot \boldsymbol{k} = 0$. On the other hand, equation 3 (known as Helmholtz's equation or master equation) describes the propagation of electromagnetic radiation in a medium with dielectric constant $\varepsilon(\mathbf{r})$. Together, these two equations enable the determination of $\mathbf{H}(\mathbf{r})$. Furthermore, by defying the operator $\boldsymbol{\Theta}$ as:

$$\boldsymbol{\Theta}\mathbf{H}(\mathbf{r}) = \nabla \times \left(\frac{\mathbf{1}}{\varepsilon(\mathbf{r})} \nabla \times \mathbf{H}(\mathbf{r})\right) \tag{4}$$

the Helmholtz's equation, which describes the propagation of light in a photonic crystal, is reduced to an eigenvalue problem:

$$\boldsymbol{\Theta}\mathbf{H}(\mathbf{r}) = \left(\frac{\omega}{c}\right)^2 \mathbf{H}(\mathbf{r}) \tag{5}$$

A photonic crystal has continuous translational symmetry in the directions in which the medium is homogeneous and a discrete translational symmetry in the directions in which the medium is periodic. In general, a system that has continuous translational symmetry is such that it remains unchanged when shifted by a distance $\mathbf{d}$. $\mathbf{T_d}$ is defined as translation operator which, acting on a generic function $\boldsymbol{f}(\mathbf{r})$, shifts the argument by $\mathbf{d}$. In a photonic crystal, we have: $\mathbf{T_d}\varepsilon(\mathbf{r}) = \varepsilon(\mathbf{r} + \mathbf{d}) = \varepsilon(\mathbf{r})$. Since $\mathbf{T_d}$ is defined as a symmetry operator of the system, one could then apply $\mathbf{T_d}$ to an eigenstate $\mathbf{H}$ of $\boldsymbol{\Theta}$. A mode with the functional form $e^{\boldsymbol{ikz}}$ is an eigenfuntion in a system with continuous translational symmetry along a z-direction:

$$\mathbf{T_d}e^{ikz} = e^{ik(z+\mathbf{d})} = e^{ik\mathbf{d}}e^{ikz} \tag{6}$$

Plane waves are eigenfunctions of $\mathbf{T_d}$ and e^{ikz} are the eigenvalues. It is then possible to classify the modes by using the wave vector $\boldsymbol{k}$. Therefore, in a homogeneous medium the modes must have the form:

$$\mathbf{H}_{\boldsymbol{k}}(\mathbf{r}) = \mathbf{H_0}e^{\boldsymbol{ik\cdot r}} \tag{7}$$

Where $\mathbf{H_0}$ is any constant vector. These plane waves are solutions of the Helmholtz equation with eigenvalues $\left(\frac{\omega}{c}\right)^2 = \boldsymbol{k}^2$ and imposing he transversality requirement , $\boldsymbol{k} \cdot \mathbf{H_0} = 0$.

In a PhC the discrete translational symmetry means that the system is periodic and the basic step length is an integer that is be equal to the lattice constant of the crystal itself, defined as **R**.

When $\varepsilon(\mathbf{r}) = \varepsilon(\mathbf{r}+\mathbf{R})$, the solutions, eigenstates of both operators $\mathbf{T_d}$ and $\mathbf{\Theta}$, should be plane waves modulated by a periodic function :

$$\mathbf{H}_{\boldsymbol{k}} = e^{i\boldsymbol{k}\cdot r}\boldsymbol{u}_{\boldsymbol{k}}(\mathbf{r}) \tag{8}$$

where $\boldsymbol{u}_{\boldsymbol{k}}(\mathbf{r})$ is a periodic function on the lattice: $\boldsymbol{u}_{\boldsymbol{k}}(\mathbf{r}) = \boldsymbol{u}_{\boldsymbol{k}}(\mathbf{r}+\mathbf{R})$.

This result is known as the Bloch - Floquet theorem and is analogous to the Bloch theorem on the electronic eigenstates in a crystal. Because of the periodic boundary condition, the wavevector which identifies the modes can be selected within the range $-\pi/a < \boldsymbol{k} < +\pi/a$ (Brillouin zone), which contains non-redundant values of $\boldsymbol{k}$. For each $\boldsymbol{k}$ the Helmoltz equation admits as solutions $\omega = \omega_n(\boldsymbol{k})$, where n, the band index that increases with the frequency of the mode.

The consequence of that discrete translational symmetry is that the resolution of the fundamental equation for the propagation of the electromagnetic radiation in a periodic medium leads to modes having $\boldsymbol{k}_z = \boldsymbol{m}\,2\pi/a$, with **m** integer, and therefore have the same eigenvalues (i.e.they are degenerate modes).

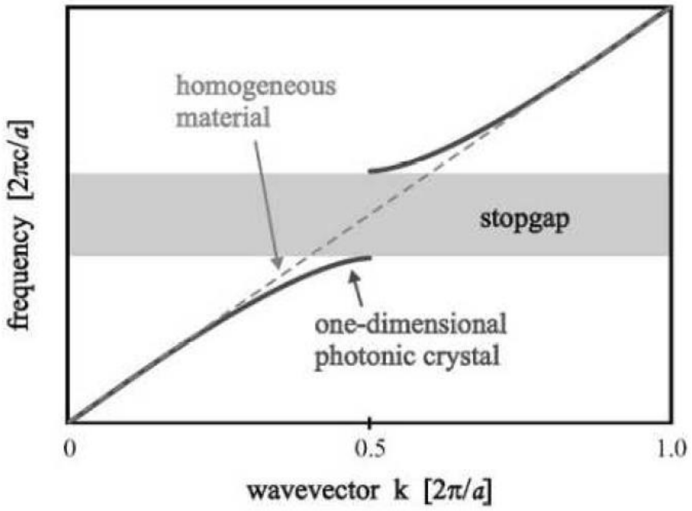

Figure 1.3 Scheme of the dispersion relation of a homogeneous medium (dashed line) and a 1D photonic crystal (solid line). Reproduced from ref. [3].

For a homogeneous material the dispersion curve is continuous (Fig. 1.3). For a crystal, indeed, the curve has a similar trend for small $\boldsymbol{k}$, but it presents a maximum and a minimum at the point $\boldsymbol{k} = 1/2$ (in (2π/a units). Radiation with frequency values within the forbidden band cannot propagate inside the crystal. Such a region can be defined as photonic stop-band when it extends alongside one crystallographic direction (i.e. 1D PhCs), whereas for higher dimensionality systems (i.e. 2D and 3D PhCs) it is usually called as photonic band-gap.

1.1.2 Scale Invariance of Maxwell's equation

An important feature of the electromagnetic field in dielectric media is the absence of a fundamental length, like the Bohr radius for the electronic states. Consequently, unlike what happens in atomic physics, where systems that only differ in their overall spatial scale have very different physical properties, for photonic crystals there is no fundamental constant with the dimensions of length, i.e. the master equation is scale invariant. This permits to study structures in any convenient scale and then extend the results in every other region of interest.

Let's assume that we want to evaluate the harmonic modes of angular frequency ω in a medium with dielectric constant $\varepsilon'(\mathbf{r}) = \varepsilon(\mathbf{r}/\mathrm{s})$, in which s is a scale parameter, i.e. in which all dimensions have been rescaled by 's'. Then in the master equation we have then to rescale by that factor and we will have $\boldsymbol{r}' = \boldsymbol{r}\mathrm{s}$ and $\nabla' = \nabla\mathrm{s}$.

We then obtain:

$$\mathrm{s}\nabla' \times \left(\frac{1}{\varepsilon(\mathbf{r}'/s)} \mathrm{s}\nabla' \times \mathbf{H}\left(\mathbf{r}'/\mathrm{s}\right) \right) = \left(\frac{\omega}{cs}\right)^2 \mathbf{H}(\mathbf{r}'/\mathrm{s}) \tag{9}$$

But is $\varepsilon(\mathbf{r}'/\boldsymbol{s})$ is $\varepsilon'(\mathbf{r})$. If we divide by the 's' factor we then obtain:

$$\nabla' \times \left(\frac{1}{\varepsilon(\mathrm{r}')} \nabla' \times \mathbf{H}\left(\mathbf{r}'/\mathrm{s}\right) \right) = \left(\frac{\omega}{c}\right)^2 \mathbf{H}(\mathbf{r}'/\mathrm{s}) \tag{10}$$

This is just the master equation again, with $\mathbf{H}'(\mathbf{r}') = \mathbf{H}(\mathbf{r}'/\mathrm{s})$ and frequency $\omega' = (\omega/\mathrm{s})$. This means that the harmonic modes and its frequency of an expanded or compressed system ($\mathrm{s} \lesseqgtr 1$) can be simply obtained by rescaling the Helmholtz's equation.

Another interesting property linked to invariance of scale is the to lack of a fundamental value for the dielectric constant, in addition to the lack of a fundamental length, as stated before. In fact, by multiplying the dielectric constant for the factor s, the photonic bands are simply rescaled by a factor $s^{-1/2}$. From this it follows that, for a system composed of two types of materials with dielectric constants ε_1 and ε_2, the photonic band structure depends only on the dielectric contrast $\Delta\varepsilon$.

1.1.3 Bragg-Snell’s Law

By considering the PhC as a one-dimensional planar structure, with interplanar distance *D,* it is possible to use Bragg’s law for coherent and incoherent scattering from a crystal lattice.

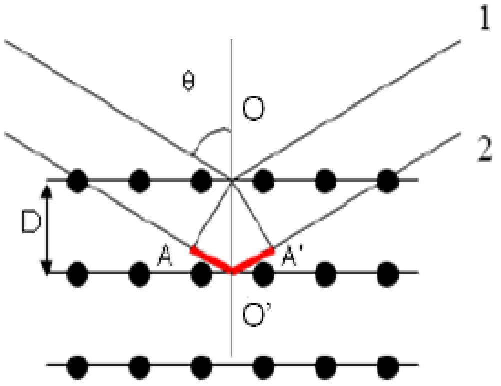

Figure 1. 4 Scheme of the diffraction process of two incident beams in a one-dimensional crystal.

According to Bragg's law [17] there is constructive interference between two beams when their optical path difference (given by the sum $AO' = A'O' = D\cos\theta$) is equal to an integer number m of wavelengths:

$$m\lambda = 2D\cos\theta \tag{11}$$

with λ the wavelength of the incident beam and θ the angle of the incidence light measured with respect to normal to the surface.

This equation is valid until $\lambda < \mathrm{D}$ and if the incidence light is specularly reflected. Since the periodicity path in PhC is much greater than the interatomic spacing, refractive indices on the media should be considered and Snell’s law ($n_i \sin\theta_i = n_t \sin\theta_t$) has to be applied.

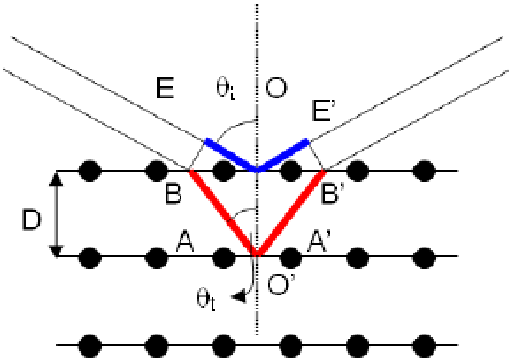

Figure 1. 5 Scheme of the diffraction model of one-dimensional photonic crystal.

Where θ_i and θ_t are the incidence and refraction angles and n_i and n_t are the refractive indices of the two media. By setting air as one of the medium ($n_i = 1$) we obtain

$$\sin\theta_i = n_{eff}\sin\theta_t \tag{12}$$

where n_{eff} is the effective refractive index of the PhC. This is calculated by using the Lorentz-Lorenz equation, where the refractive indices of the media are weighted by their volume fraction f_n:

$$\frac{n_{eff}^2-1}{n_{eff}^2+2} = \sum_n f_n \frac{n_n^2-1}{n_n^2+2} \tag{13}$$

The optical path is equal to the geometric path multiplied by the effective refractive index:

$$m\lambda = 2\left(n_{eff}BO' - EO\right) \tag{14}$$

with

$$BO' = \frac{D}{\cos\theta_t} = \frac{Dn_{eff}}{\sqrt{n_{eff}^2-\sin^2\theta}} \tag{15}$$

and

$$EO = BO\sin\theta = \frac{D\sin^2\theta}{\sqrt{n_{eff}^2-\sin^2\theta}} \tag{16}$$

as obtained by straightforward geometrical considerations.

The Bragg-Snell's law is then obtained from Eq. 12 by substituting BO' and EO with the solutions of the equations above (13 and 14):

$$m\lambda = 2\left(n_{eff}BO' - EO\right) = 2\left(\frac{Dn_{eff}^2}{\sqrt{n_{eff}^2 - \sin^2\theta}} - \frac{D\sin^2\theta}{\sqrt{n_{eff}^2 - \sin^2\theta}}\right) = 2D\sqrt{n_{eff}^2 - \sin^2\theta} \qquad (17)$$

Where λ is the spectral position of the photonic stop-band that depends on the angle of the incident light θ, the interplanar spacing between the media D and the refractive indices and volume fraction of the media (contained in $\mathrm{n}_{\mathrm{eff}}^2$).

1.1.4 Density of states

The density of state (DOS) of a system is the number of allowed state per unit interval of frequency ω[18]. The optical properties of an emitter strongly depend of the DOS, according to the Fermi's golden rule. The density of states of the radiation field in the volume V of free space, D(ω), is proportional to ω^2:

$$D(\omega) = \frac{\omega^2 V}{\pi^2 c^3} \qquad (18)$$

The density of states in the uniform material is obtained by replacing c by $v = c/n$ in this equation. In a PhC, within the photonic-gap no modes are allowed, and therefore the density of states (defined as the number of possible modes per unit frequency) is zero.

The optical properties of atoms and molecules strongly depend on D(ω). A way to control and modify D(ω), and in turn the emission properties and radiative rate of emitters, is to use photonic crystals.

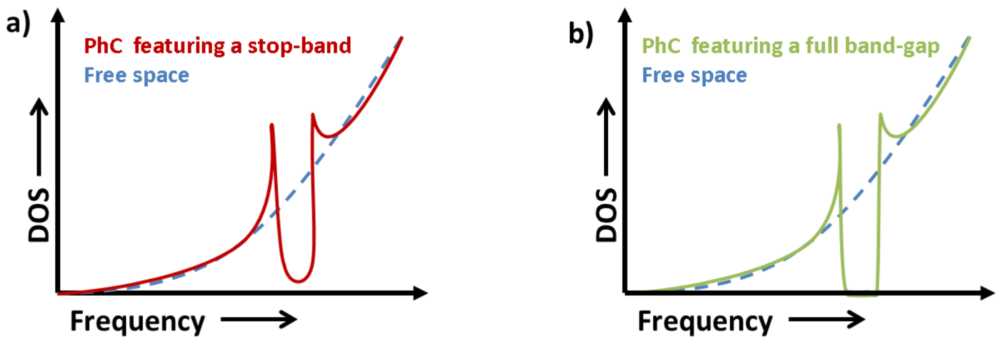

Figure 1.6 Schematic illustration of the density of states of the radiation field in free space (dashed blue line) and (a) in a photonic crystal featuring a stop-band (red line) and (b) in a photonic crystal featuring a full band-gap (green line).

In particular, when an active material is embedded into a PhC, its optical properties are strongly affected by the periodical dielectric environment, which alter the dispersion properties of photons (i.e. photonic density of states, p-DOS)[19]. Indeed, the p-DOS diminishes within the photonic band gap thus suppressing light-emission. On the other hand, at the edges of the photonic band gap, the p-DOS increases [20], i.e. a light-emission enhancement is observed. Both enhancement and suppression of the emitted light are accompanied by an increase and decrease of the radiative rate, respectively. Such an effect on the radiative rate can be used to modify, for example, the photoluminescence spectrum of the embedded material. In fact, as discussed in Chapter 2, the photoluminescence quantum yield is function of the emission lifetime (τ), which depends on the DOS via the Fermi's golden rule [21]:

$$R_{i\rightarrow f}(\omega) = \frac{2\pi}{\hbar}|\langle f|H'|i\rangle|^2\rho(\omega) \tag{19}$$

where R is the transition probability from an initial state *i* to a finale state *f* and is related to the mean lifetime τ (R = 1/τ), ρ is the density of final states and $|\langle f|H'|i\rangle|^2$ is the matrix element of the perturbation H' between the final and initial states. This matrix element depends on the coupling between the initial and final stated of the system.

1.2 Transparent and conductive nanostructured thin films

Nowadays, great efforts have been made to replace indium tin oxide (ITO). So far ITO has been commonly used in many applications but it has some drawbacks, such as the high cost, the scarcity of indium and the brittleness[22] that limit its application mainly in flexible devices. Innovative nanostructured materials, such as carbon nanotubes (CNTs) and metal nanowires have been demonstrated to be good candidate to replace ITO as transparent conductive electrodes (TCE) in optoelectronic devices. In this regard, the two most important parameters are the TCE sheet resistance and optical transparency[23]. In particular, an optimized electrode typically transmits >80% in the visible spectral range and its sheet resistances (R_{sheet}) should be less than 20 Ω/□ [24].

1.2.1 CNTs

CNTs were first synthesized in 1991 by Iijima and Ichihashi [25, 26] at NEC laboratories in Japan. Since their discovery, CNTs have been extensively studied thanks to their outstanding electrical and mechanical properties. In fact, their unique characteristics, in addition to their nanoscale size, enabled them to be used in a variety of applications.

Carbon nanotubes can be thought of as a rolled-up sheet of graphite, closed at each end. They can be multi-walled or single-walled. A single-walled carbon nanotube (SWCNT) consists of just one layer of graphite and it has a diameter around 1nm, while a multi-walled nanotube (MWCNT) has multiple concentric layers and it can have an outer diameter ranging from 2.5nm to 30nm [27] (Fig. 1.7).

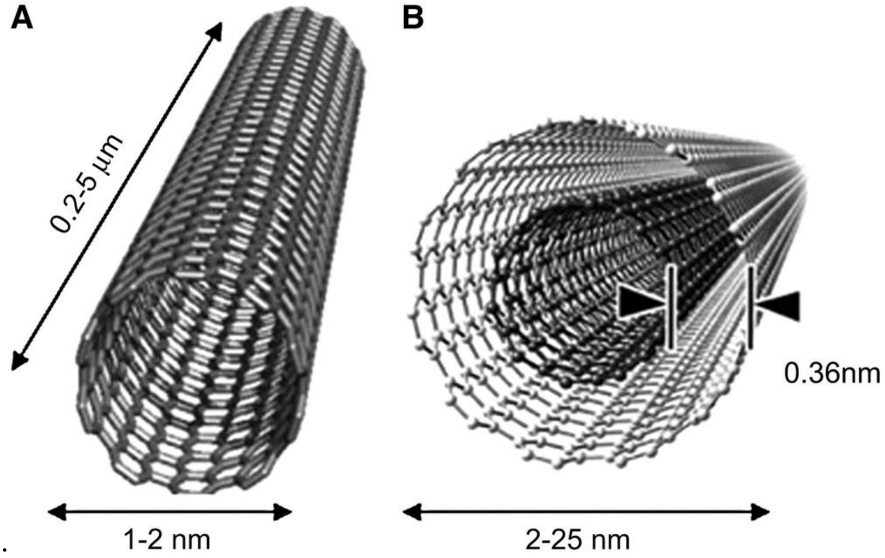

Figure 1.7 Schematic illustration of a SWCNT (a) and (b) of a MWCNT, with their typical dimensions. Taken from ref. [28].

Carbon nanotubes can be either conducting or semi-conducting along their tubular axis [29-31]. Some nanotubes appear to exhibit ballistic conduction along the tube, which is a characteristic of a quantum wire [27, 32]. Ballistic conduction or transport is when electrons are able to flow without colliding into impurities or being scattered by phonons.

Despite such fascinating properties, significant challenges emerged for CNTs films. In fact, transport mechanisms are still not completely clear, especially at the junction between two tubes. In addition, considering that commercially available CNTs are often a mixture of nanotubes with different electrical properties, the study of these films is a non-trivial task. Typically, these junctions between nanotubes have high resistance in the range of 200 kΩ - 20 MΩ [33]; hence, the conductivity of CNT films is reduced drastically compared to that of a single CNT that have a carrier mobility of ~10,000 $cm^2V^{-1}s^{-1}$ [34]. Some approaches have been introduced to reduce the sheet resistance of the CNT films such as treating CNTs with acid and using longer CNTs [35]. The semiconductor nanotubes have much lower conductivity than the metallic tubes [33] and so do not contribute much to the conductivity. Furthermore, they absorb light and so reduce transparency. In addition, metal/semiconductor junctions in CNT films create high contact resistance due to Schottky barrier formation, resulting in higher sheet resistance [33]. Separating metal and semiconductor CNTs or producing metallic only CNT are still serious challenges [36]. Although some methods have been introduced to separate metal nanotubes, most of them are not yet suitable for large-scale technological processes.

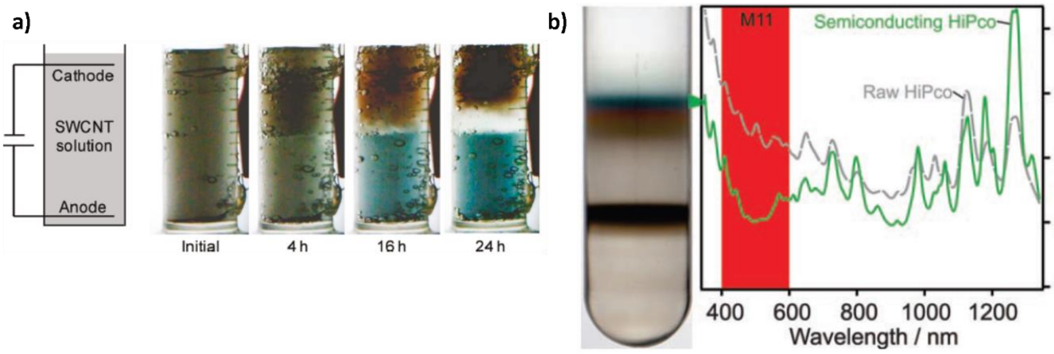

Figure 1.8 (a) Sketch of an electrophoretic cell and photos of SWCNTs solution in before and 4, 16, and 24 h after the application of 30V (taken from ref. [37]) and (b) Separation of semiconducting SWCTs starting from a mixed metallic semiconducting solution obtained via ultracentrifugation method. The separation can be observed both in the photo and in the absorbance spectra. Adapted from ref. [38].

The most efficient methods, with examples reported in Fig. 1.8, rely on density-gradient ultracentrifugation [38-40], which separates nanotubes dispersed in a solution with a surfactant exploiting the difference in their density, and vertical electrophoresis, where an aqueous solution of mixed SWCNTs is separated into metallic and semiconducting nanotubes simply applying an electric field along the cell [37, 41, 42].

1.2.2 Metal nanostructures

Metal nanostructures are an appealing alternative to ITO and many other transparent electrodes since metals have the highest conductivity of all types of materials. On the other hand, the major drawback of metallic materials is the very low transparency of metals to visible light. The only possible way to fabricate transparent electrodes using metallic structures is to use nanostructured materials. Metal nano-grids, ultra-thin metal films (of less than 10 nm thickness) and random networks of metal nanowires are three of the most used structures to make transparent electrodes [35].

Metal films can be used as transparent electrodes when they are sufficiently thin, usually less than few tens on nm, at which point they become transparent to visible light [43-45]. In fact, the biggest trade-off in using these materials is that films need to be thin enough to transmit sufficient light without becoming discontinuous and start to suffer from poor electrical conductivity. The main issue is that for metal such Ag and Au, the conductivity would be good at thicknesses for which the transmission remains high. This is due to the intrinsic instability of ultra-thin films, where there is a tendency to coalescence of mostly un-connected grains, which generally prevents their application as transparent electrodes.

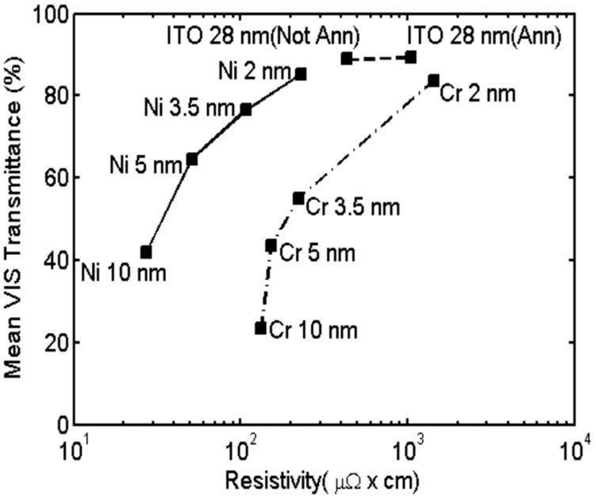

Figure 1.9 Average optical transmittance in the visible range as function of the t electrical resistivity for Cr and Ni films compared with ITO anneal and not annealed. Reproduced from ref. [45].

Figure 1.9 illustrates the sheet resistances and transparencies of Cr and Ni thin films of various thicknesses [45]. In addition to the low transparency and conductivity values, metallic thin film deposition happens at ultrahigh vacuum by DC sputtering, which has a high manufacturing cost [35].

Metal nano-grids consist of ordered metal strip lines and are normally patterned by complex fabrication processes such as nanoimprint lithography [46] and electron beam lithography [35, 47]. The main advantage of these structures compared to thin films is that the total transmission is dramatically increased. In fact, whereas through the metal strips the transmittance is almost zero, in the gaps between them the transmittance is 100%. Therefore, the total transmittance, defined by the percentage of the total area that is covered by the metal grid, can reach values similar to the one of ITO [47]. However, this increase in transparency comes at the price of an increased surface roughness.

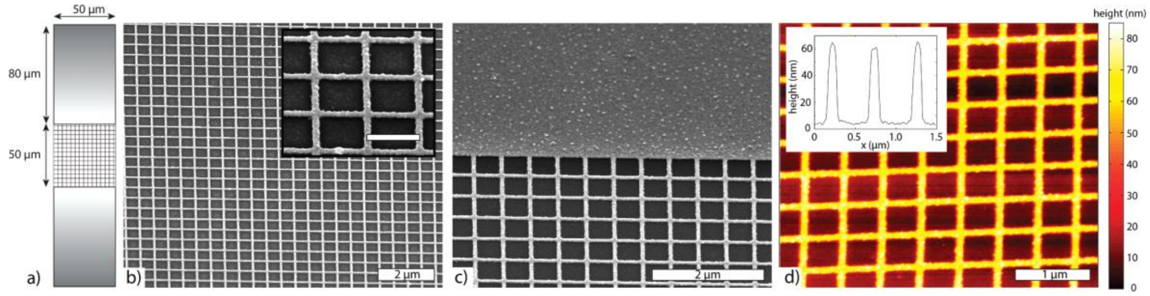

Figure 1.10 (a) Sketch of the sample geometry, lines in the network are not to scale, (b) SEM image of a network showing the high uniformity over a large area (inset) individual Ag wires with a scale bar of 500 nm., (c) SEM image showing the contact area of the wire network and the electrical contact pads. (d) AFM image network shown in (b) (inset) extracted line profile. Image taken from [47].

Figure 1.10 shows an example of a nano-grid structure. Although in terms of sheet resistance and transparency these structures are competing with the performance of ITO [47] , on the other hand the high surface roughness, the difficult fabrication methods and the costly patterning techniques strongly limit them to be used is optoelectronic devices.

A final class of transparent electrodes consisting of a random network of metal nanowires have recently been realized and used in devices [48-50] .These nanowires network, shown in figure 1.11, keep the advantages of patterned metal structures in terms of sheet resistance and transparency, and combine that with the low cost and solution processable fabrication method. In fact, films can be easily prepared using simple and inexpensive deposition methods [51] like drop casting [50], vacuum filtration [52], spin-coating [53], spray-coating [54], and roll-to-roll process [55], and, interestingly, the preparation methods are compatible with plastic substrates in producing flexible electrodes. In fact, the main advantage of nanowire is that films are mechanically flexible

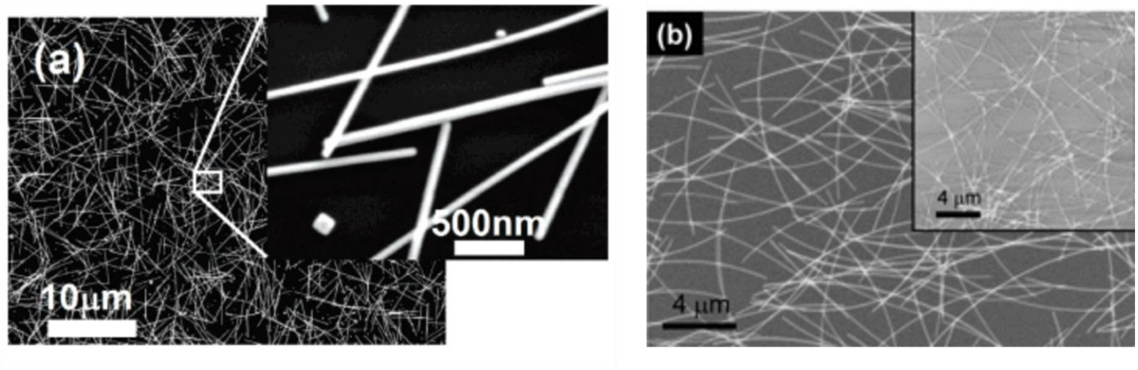

Figure 1.11 SEM images showing AgNW mesh deposited via drop-casting (a) and spin-coating (b). Taken from ref. [50] and ref. [53].

Among the various metal that can be exploited in the preparation of nanowires (Ag, Cu and Au) [51], silver is one of the most promising since it does not tend to oxidise, it has high DC conductivity and a relatively low cost compared with other alternatives. So far, silver nanowire electrodes show superior performance compared to graphene and CNTs [48].

Copper nanowires are also being used for transparent conductors since copper is cheaper than silver and has high conductivity. Reported copper (and copper-based) nanowire transparent electrodes show superior performance than CNTs and comparable to silver nanowires and ITO [51].The main concern of using copper nanowires is their instability in air due to the fact that copper reacts with atmospheric oxygen and thus need to be passivated to prevent oxidation when used as electrodes. [56, 57].

1.3 Nano- micro-structuring techniques

The field of nanostructures and photonic crystals has developed in a variety of directions, often dictated by the hurdles of fabrication of structures whose periodicity needs to be on the same lengthscale as that of the wavelength of the light one desires to control or the desired surface roughness [58]. This places some stringent requirements, as one needs to generate patterns with typical dimensions/periodicities of the order of a few hundreds of nanometres. Typical fabrication methods can be dived into two major classes: top-down and bottom-up approaches.

1.3.1 Top-Down approaches

So far, the development and production of nanostructures has been generally focused on top-down nanofabrication[59-62] making use of lithographic techniques such as electron-beam and focused ion-beam patterning (FIB). These are very expensive, and being essentially “serial” suffer from significant limitations in terms of either surface areas or sample throughput, in addition to being limited to the fabrication of mainly two-dimensional structures. Another major drawback is that the photonic effects are strongly inhibited by the residual surface roughness, thus spoiling the overall Q-factor of the cavities[63]. One technique that has shown more promise is the laser-assisted photopolymerisation/activation of a cross-linker, to generate 3D nanostructures[64, 65] (figure 1.12) but for the as-prepared structures one needs some extremely careful control of the mechanical relaxation effects of the structures after the polymerization to avoid distortion of the architectures and to ensure adherence to the intended pattern.

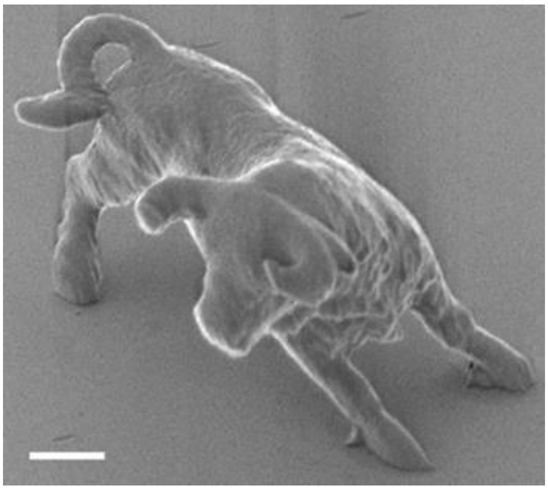

Figure 1.12 A scanning electron micrograph of the micro-bull obtained by photopolymerisation, the scale bar is 2 micrometres long. Taken from ref. [64].

In addition, and somewhat in between the two approaches detailed above, we find a host of "non-conventional" top-down methods that are not "serial" (as e-beam and FIB) thereby allowing fabrication of structures over large (several square cm) areas. These methods consist for example in the spin-coating of polymers[66, 67] and the electrochemical micromachining of porous silicon[68-71]. Whereas spin-coating has been mainly used just to fabricate polymeric multilayers (e.g. full-plastic distributed Bragg reflectors), electrochemical micromachining, that consists of a controlled electrochemical etching of porous silicon (Fig. 1.13), is a far more versatile technique and enables the preparation of inorganic PhCs and microstructures with different dimensionalities (1D rugate filters, DBRs, micorcavities and 2D arrays and micrtosustems) with sub-micrometre accuracy[72, 73].

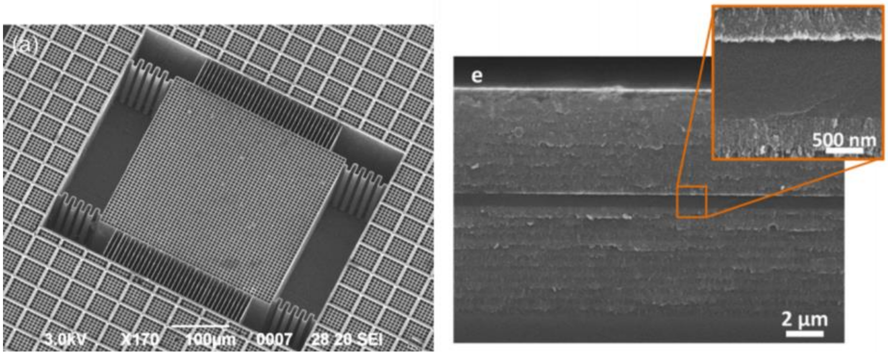

Figure 1.13 (a) A scanning electron micrograph of an electrochemical micromachined microsystem (MEMS) taken from ref. [70] and (b) a porous silicon microcavity taken from ref. [71].

1.3.2 Bottom-up approaches

By contrast, bottom-up approaches exploit the collective self-assembly of suitably-sized building blocks (typically colloidal dielectric microspheres or charged polyelectrolytes). This provides a much easier, faster, and low cost alternative to top-down methods in preparing photonic crystals and nanostructures, enabling the preparation nanostructured multilayers exploiting the so-called layer-by-layer deposition (i.e. deposition of charged polymera/precursor that can regulates itself in terms of thickness and resulting in reproducible deposition with layers thicknesses of around 1-5 nm[74, 75]) and of both 2D (close-packed microspheres monolayers [76, 77]) and, more interestingly, 3D (artificial opals [78-81] and inverse opals [82, 83]) structures. Since this is not a "serial" approach, it has the scope and potential to generate significantly larger samples. However, self-assembly methods lead to structures with a relatively high density of defects[84] that limit their application in optical devices.

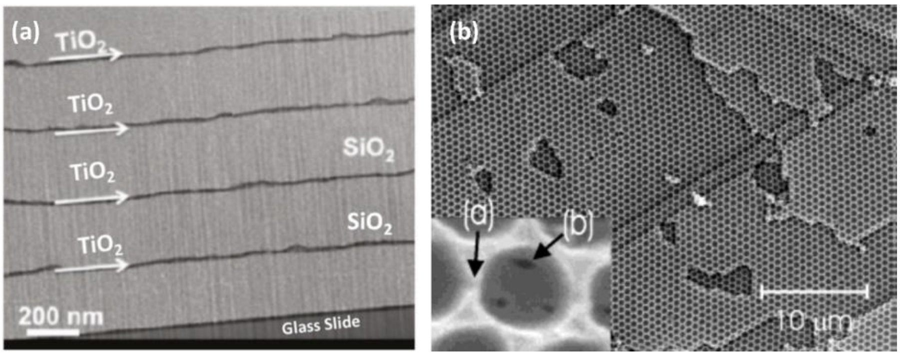

Figure 1.14 (a) TEM cross-sectional image of an L-b-L assembled multilayer. Adapted from ref. [75] (b) image of a polymer inverse opal, revealing the optimal replication process(inset) detail of one hollow sphere, taken from ref. [83].

Chapter 2
Organic semiconductors and Organo-halide perovskite

Since the discovery of the electrical conductivity in doped polyacetylene in 1977 by Shirakawa, McDiarmid and Heeger [11], there has been great effort in the study and development of conductive and semiconductive polymers. In fact, this class of material has many advantages compared to the inorganic ones, in particular they are easily processed, the cost is relatively low and they can also be flexible and lightweight. For all these reasons, organic semiconductors have been exploited in optoelectronic devices such as organic light-emitting diodes (OLEDs) [12], organic photovoltaic cells (OPV) [13] and organic field-effect transistors [85].

2.1 Electrical properties

The electrical properties of the organic semiconductors (OS) arise from the sp^2 hybridisation of the carbon atom constituting the conjugated system [86].

The electronic configuration of a carbon atom is $1s^2$ $2s^2$ $2p^2$.According to this, only two electrons in the p orbital are available to form bonds with another atom. But, thanks to the hybridisation between atomic orbitals, carbon atoms can have four valence electrons and thus form four bonds with adjacent atoms. The hybridisation of carbons can be sp^3, sp^2 and sp^1 (Fig. 2.1).

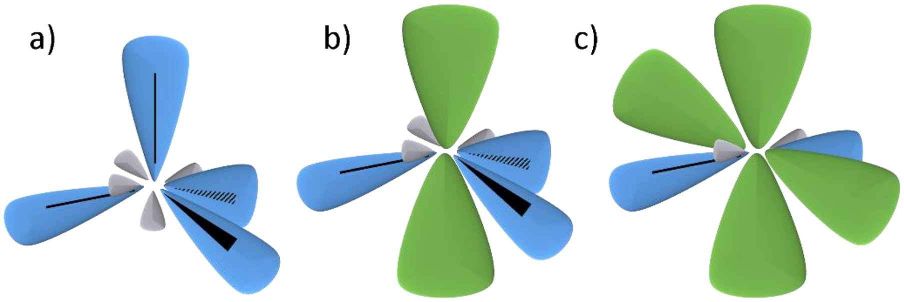

Figure 2.1 (a) sp^3 hybridisation, where 4 σ bonds (in blue) are formed with an angle of 109.5° between the bonding orbitals (b) sp^2 hybridisation shows a trigonal-planar geometry with an angle of 120° between the three σ bonds, the remaining π bonds (in green) are perpendicular to the σ ones (c) in the sp hybridisation there are only two σ bonds with an angle of 180° between them.

In saturated polymers the 2s and the 3 2p orbitals fused together to make four, equal energy sp^3 hybrid orbitals and every carbon is bonded to four neighbouring atoms, therefore molecular orbitals are fully saturated. Polyethylene is a typical saturated polymer, in which the carbon atoms have four σ-bonds, two with neighbouring carbons and two with hydrogen atoms. Saturated polymers are insulators because to promote an electron from a bonding to an anti-bonding orbital requires an energy $E = 8$ eV or more.

In a conjugated system the carbons are sp^2 hybridized: the 2s orbital is mixed with two of the 3 available 2p orbitals, forming three sp^2 orbitals per each carbon, plus one free p orbital. This results in the formation of 3 coplanar bonds made with the sp^2 hybrid orbitals (also called σ bond), with an angle of 120° between them, with the adjacent atoms. The remaining 2p orbital, which is not hybridized, is perpendicular to the sigma bond and it is defined as $2p_z$. When two $2p_z$ from two neighbouring carbon atoms overlap, a π orbital is formed, resulting in the creation of a double bond.

In particular, we define conjugated the (macro)molecules where there is an overlap of the p-orbitals along the chain due to an alternation of single and double bond between two adjacent carbon atom and this alternation creates (semi)delocalised states along the (macro)molecule chains.

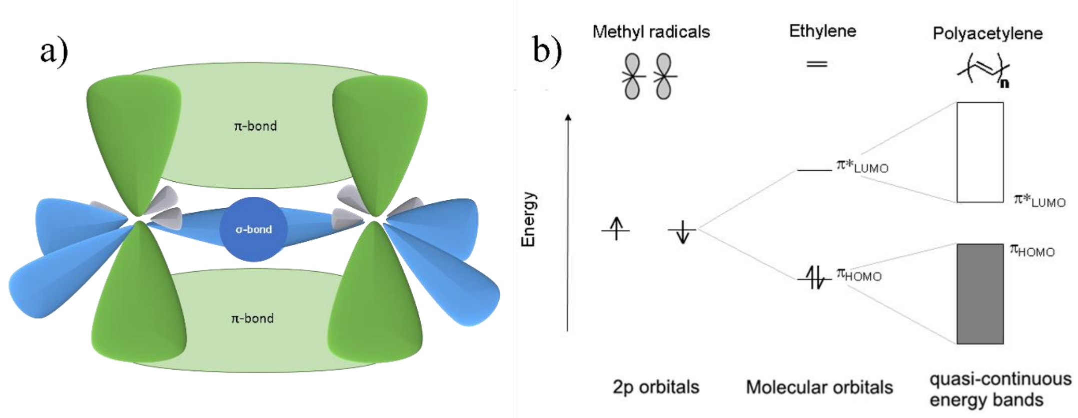

Figure 2.2 (a) Scheme of the sp^2 hybridisation in an ethylene molecule (b) Scheme of the energy splitting of 2p orbitals into a bonding and an antibonding orbital. Increasing the CH_2 units leads to an increase in the degeneration of energy levels resulting in two quasi-continuous bands, namely the highest occupied molecular orbital (HOMO) and the lowest unoccupied molecular orbital (LUMO).

The simplest conjugated system is constituted by two carbon atoms hybridized sp^2 (ethene molecule CH_2=CH_2, figure 2.2(a)), the overlap of two $2p_z$ leads to the formation of a molecular bond and the splitting into a bonding and antibonding molecular orbitals.

The π orbital is lower in energy than the original $2p_z$ orbital while the π* orbital is higher in energy than the atomic orbital. For this reason, in the ground state, the two electrons coming from the $2p_z$ orbitals of two carbon atoms will occupy theπ orbital. Thus, the bonding orbital π is called the highest occupied molecular orbital (HOMO) whereas the anti-bonding orbital π* is called the lowest unoccupied molecular orbital (LUMO).

Increasing the number of carbon atom (for example in the case of the polyacetylene polymer, $(CH)_n$, that is the simplest case in terms of geometry) results in a quasi-continuous bands of occupied and unoccupied states that leads to the semiconducting properties (figure 2.2(b)). The number of alternated single-double bonds in a polymer is defined as conjugation length, and it affects the energy spacing between the HOMO and LUMO levels and thus both the electrical and optical properties of the polymer. This conjugated are characterised by strong intramolecular electronic interaction, but weakly coupled to each other.

2.1.1 Semiconducting behaviour and charge transport

At the beginning, conjugated polymers were expected to have a metallic behaviour instead of a semiconducting one. In fact, we can consider the polyacetylene chain (figure before) a 1D crystal of N atoms with a periodicity a. In this system there should be a complete delocalisation of the electron wavefunction on the entire polymer that would lead to a minimisation of the molecular energy. Since the volume of 1 electronic state in the k-space is V = 2π/Na, and we can accommodate 2N electrons in the volume of the Brillouin zone (V_{BZ} = 2 π /a), by calculating the ratio V_{BZ}/V = 2(2 π /a)/(2 π /Na) = 2N, we can expect an half-filled band (only N electrons are available), i.e. a metallic behaviour.

However, since the single and double bonds have different lengths (in particular double bonds are shorter than single ones), Peierls distortion (or dimerization) occurs. As a consequence, there is a doubling of the unit cell that will reduce the Brillouin zone to half, which, in turns, generates a gap formation right at the Fermi energy, leading to a semiconducting behaviour [87].

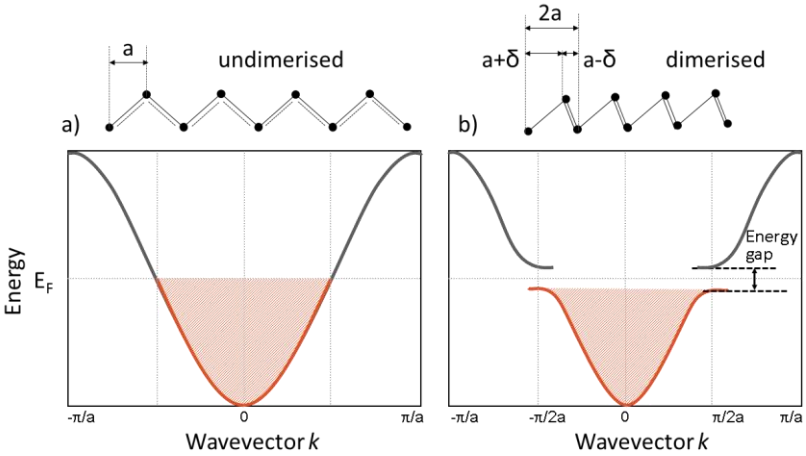

Figure 2.3 (a) an undimerised polyacetylene chain (with a complete delocalisation of the electron wavefunction) and equal distance *a* between the atoms of the chain. The corresponding band structure shows that the band is half-filled up to the Fermi energy (EF) (b) Peierls dimerisation of polyacetylene, where the distance between the atoms of the chain is different if it is a single or double bond. The corresponding band structure shows the formation of an energy gap at the edge of the Brillouin zone.

In contrast to inorganic semiconductors, due to the weak overlap of electron density of the chromophores, charges are strongly localised. Electron and hole are strongly bound by Coulomb attraction with a typical binding energy of 0.3 eV to 1 eV. Such electron-hole pairs can be described as neutral quasi-particles called Frenkel excitons, in contrast to Wannier-Mott excitons, that are typical for inorganic semiconductors, which are characterised by much lower binding energies (typically a few meV) and that can be delocalised over tens of the lattice constant in inorganic materials. These charged or neutral excited states can be formed, caused by redox reactions, or charge injection.

The charged quasi-particles, which are defined as polarons, induce also a lattice deformation, which leads to the formation of localised states within the forbidden gap, i.e. a charge is self-trapped by the deformation it induces in the polymer chain. However, polarsons can move both along the polymer chains and across them. As a consequence, charge transport might only happen via hopping mechanism between these states and it is strongly dependent on the order of the structures. In fact, it can vary from 10^{-6}-10^{-3} cm^2/Vs for disordered structures, up to 0.1-30 cm^2/Vs for more crystalline ones [85], with some exceptional cases even reaching several hundreds cm^2/Vs for certain single molecules [88].

2.1.2 Work function

The work function is the difference between the vacuum level and the Fermi energy, which is in turn defined as the energy with probability 1/2 to be occupied, according to the Fermi-Dirac statistics. For a metal this also coincides with the minimum energy required to extract an electron to just outside the material. More precisely, the electron is removed from the highest potentially occupied electronic energy level in the solid, the Fermi level E_F, to the vacuum level, E_{vac}, which is the energy level of an electron positioned at rest outside the solid, at a distance sufficient for the electron to experience the full impact of the surface dipole (figure 2.4). The work function was first defined in this way by Wigner and Bardeen in 1935 [89].

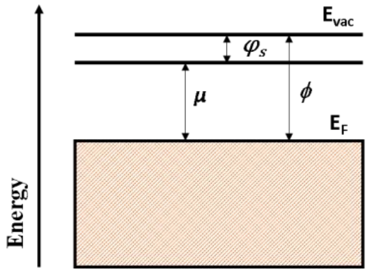

Figure 2.4 Electronic energy level diagram of a solid showing the various energies relevant to the definition of the work function.

The work function (ϕ) can be thought of as made up of two contributions: the chemical potential μ, which depends on bulk property and the surface potential φ_s which is a surface-dependent part. The chemical potential is the energy difference between before and after the removal of the electron from the solid. The surface component depends strongly on the condition of the surface the solid and it arises from the presence of a surface dipole layer. This dipole layer is due to the fact that a surface does not present an infinite potential barrier to the electrons within a solid. Although the electrons are bound in the solid, the electronic wave-functions might have non-zero amplitude in the proximity outside the surface [90]. This probability of an electron to exist outside the surface is balanced by the corresponding excess positive charge remaining in the solid thus giving rise to the surface dipole and the voltage across this layer is the surface potential mentioned before.

The presence of surface adsorbate, i.e. molecules or polymers caused by chemisorption or physisorption, induces changes in the surface potential, $\Delta\varphi_s$, and, thus in the work function. The magnitude and sign of $\Delta\varphi_s$ depends on the electronegativity of the molecules involved and on the orientation of the surface dipoles. In particular, if the adsorbate has an electronegativity, χ_{ads}, higher than that of the substrate, χ_{sub}, it attracts electrons, leading to a decrease in the surface potential decreases and the work function increases, on the other hand, if χ_{ads} is lower than χ_{sub} the surface potential increases and the work function decreases. Orientation of adsorbate-induced dipoles and the respective work function change and in particular, when the adsorbate is polarised with the positive pole towards the vacuum side results a decrease inϕ, per contra, when it is polarised with the negative pole pointing towards the vacuum side, ϕ increases (figure 2.5).

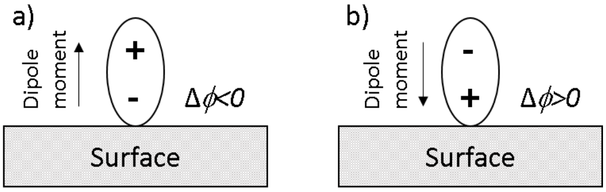

Figure 2.5 Orientation of the dipoles induced by the adsorbate: (a) the adsorbate is polarised with the positive pole towards the vacuum side causing a decrease in ϕ and (b) with the negative pole pointing towards the vacuum side, causing am increase inϕ.

Among the numerous characterization methods and techniques for determining the materials work functions, Kelvin probe (KP) is one of the most powerful tools for reliable work function measurements. KP measures the work function differences between a conducting sample and a reference tip in a non-contact, truly non-invasive way.

The KP technique relies on the existence of a potential difference between the surfaces of two different metals electrically connected. It is named after Lord Kelvin who reported an experiment based on the transport of “electricity” between two dissimilar metals in 1898 [91]. He described the movement caused by Coulomb repulsion within a gold-leaf electrometer when he brought zinc and copper plates into close proximity while the plates were electrically connected.

In fact, when metals are connected, the electrons start flowing from the metal with the lower work function to the one with the higher work function, until the electrochemical potential (Fermi Energy) in both connected metals is the same. Such alignment of the Fermi levels produces this movement of charges and in turn induces the appearance of a potential difference between the two metals, called the contact potential difference, V_{cpd}. This is equal to the initial work function difference existing before contact between the probe (i.e. the reference electrode) (ϕ_1) and the sample (ϕ_2). Hence, the measurement is based on compensating the contact potential difference with an externally applied voltage.

In 1932, Zisman published an improved method for quantifying the potential difference between two metal plates [92]. Here, the probe is vibrating just above a sample electrode. The output voltage varies periodically as the probe vibrates, and the peak-to-peak voltage depends upon the difference between the contact potential difference and the external voltage. The basic electrical circuit of the Kelvin probe is shown in figure 2.6.

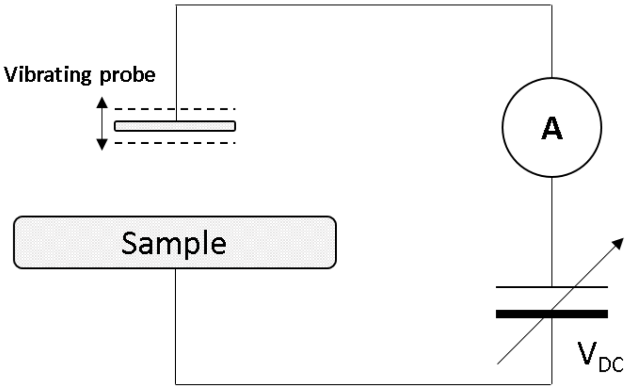

Figure 2.6 Electric circuit of the Zisman's KP set-up.

The probe consists of a flat circular electrode (the reference electrode) suspended above and parallel to a stationary electrode (the sample) separated at a distance d_0, thus creating a simple capacitor.

$$C_k = \frac{\varepsilon_0 \varepsilon_{air} A}{d_0} \tag{20}$$

where C_k is the capacity of the system, ε_0 is the permittivity of free space, ε_{air} is the dielectric constant of air, A is the area of each metal plate, and d_0 is the distance between the two electrodes.

As the probe tip vibrates, the distance between them varies as:

$$d(t) = d_0 + B\sin(\omega t) \tag{21}$$

where d_0 is the initial mean distance between electrodes before vibration, and B and ω are respectively the amplitude and the frequency of the reference electrode vibration.

Hence, the vibration of the capacitor induces an alternative current *i(t)* to flow between electrodes when both electrodes are connected due to the movement of the capacitive charges on the capacitor plates:

$$i(t) = V_{cpd}\frac{\partial C}{\partial t} = -V_{cpd}\frac{\varepsilon_0 \varepsilon_{air} AB\omega\cos(\omega t)}{(d_0 + B\sin(\omega t))^2} \tag{22}$$

and by applying an external voltage V_{DC} we find that:

$$i(t) = (V_{DC} - V_{cpd}) \frac{\varepsilon_0 \varepsilon_{air} AB\omega \cos(\omega t)}{(d_0 + B\sin(\omega t))^2} \quad (23)$$

In Zisman's method, the V_{cpd} is then obtained when the current going through the capacitor goes to zero and $V_{DC} = V_{cpd}$. Consequently, the work function of the sample electrode can be obtained by:

$$\phi_2 = \phi_1 - eV_{DV} \quad (24)$$

where e is the electron charge and considering that the work function of the probe ϕ_1, has to be known.

2.2 Optical properties

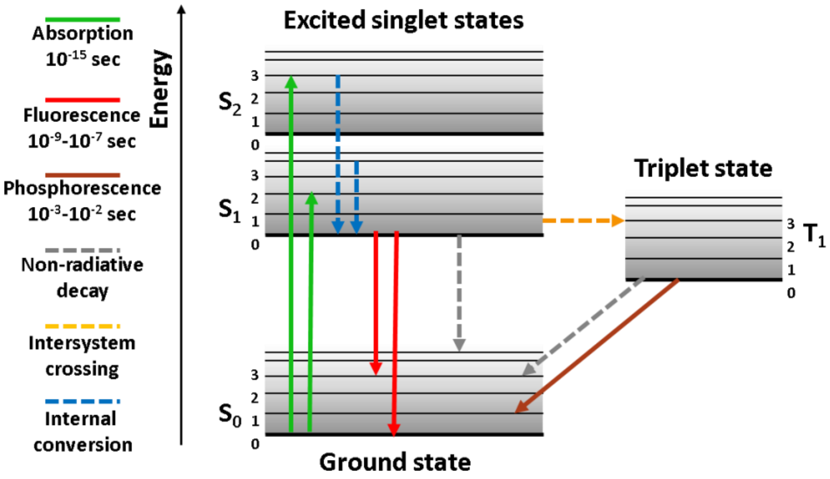

Figure 2.7 Jablonski diagram illustrating the different electronic and vibrational levels in an organic molecule and, the different optical transitions.

The optical properties of organic semiconductors can be easily described using the Jablonski diagram (figure 2.7) [93]. This illustrates the most important electron transitions. The ground state is a singlet state (i.e. where total spin quantum number S=0 and therefore the spin multiplicity is 2S+1=1) and it is indicated as S_0. The singlet excited electronic energy states are indicated as S_1 and S_2. Each electronic state is divided into vibronic states. The triplet excited state (where total spin quantum number S=±1 and the spin multiplicity is 2S+1=3) is indicated as T_1.

Absorption is the vertical transition from the ground state to the singlet excited state. This is a fast process and typically occurs in a fs regime. After absorption, electrons promoted to S_2 relax to S_1 by internal conversion. Due to a fast internal conversion (ps regime), the electrons quickly relax to the lowest excited state in S_1, from where the emission can take place. This is consistent with Kasha's rule, which states that return to the ground state is most likely to take place from the lowest vibrational level of the first excited state. In fact, fluorescence consists of the radiative transition from the lowest excited singlet state to the ground state, i.e. from S_1 to S_0 and it occurs on nanosecond timescale.

The transitions between singlet and triplet states are not allowed in the dipole approximation. However, such transitions, known as intersystem crossing (ISC), become allowed because of the coupling of the electron spin with the orbital angular momentum. The radiative transition from T_1 to ground state is not spin-allowed and therefore the emission occurs typically over microsecond to milliseconds and it is defined phosphorescence.

The Morse potential energy curve (figure 2.8) is a model that describes the potential energy of molecules. It takes into account the anharmonicity of real bonds due to bond breaking and to the repulsion between nuclei. The Morse curves for the ground state S_0 and the excited S_1 have different geometries. In particular, in the excited state the nuclei are more distant (since it is an anti-bonding state) and the curve is less deep and larger (due to a reduced strength of the bonding).

This statement, together with the Kasha's rule and the Franck-Condon principle (that states that the nuclei do not move during the electronic transitions), explains the symmetrical shape of absorption and emission spectra. Furthermore, the electronic transition will be more likely to happen between two vibrational levels whose wavefunctions overlap more significantly.

Typically, the maximum of absorption and emission do not spectrally overlap (Stokes' shift) due to different transition probability between absorption and fluorescence [93].

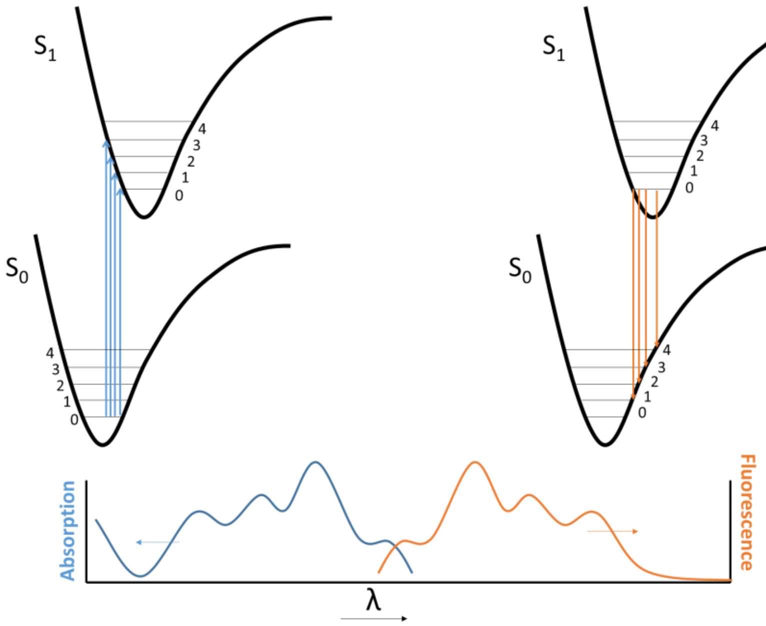

Figure 2.8 Scheme of Morse potential energy curves with vibrational energy levels indicated for each state. It illustrates the Franck-Condon principle and the origin of the symmetrical shape of absorption and emission spectra in organic molecules. The difference between the maxima of the absorption and fluorescence spectra is the Stokes' shift.

2.2.1 Photoluminescence properties and energy transfer

The fluorescence lifetime and quantum yield are perhaps the most important characteristics of a fluorophore. The fluorescence lifetime (τ) of a fluorophore is defined as the average time between its excitation and return to the ground state and it is particularly sensitive to the environment [93]. It can be expressed in terms of the radiative (k_r) and non-radiative (k_{nr}) rate decay to S_0 according to:

$$\tau = \frac{1}{k_r + k_{nr}} \tag{24}$$

Another important parameter is the emission quantum yield (*Q*) that is defined as the ratio of the number of photons emitted to the number absorbed. It is again given in term of radiative and non-radiative decay rate:

$$Q = \frac{\mathrm{k_r}}{\mathrm{k_r + k_{nr}}} \tag{25}$$

Thus, *Q* and τ, along with the absorption and emission spectra, are important parameters to investigate the photophysics of organic semiconductors.

The photoluminescence intensity (i.e. the photoluminescence quantum yield) can be decreased by different of processes. Such decrease in intensity is called quenching and they occur by different mechanisms. The two general kind of quenching are collisional (dynamic), and static quenching. Collisional quenching takes place when the chromophore in the excited-state is deactivated after being in contact with some other molecule (the quencher) without being chemically altered. In this case the chromophore is returned to the ground state during a diffusive encounter with the quencher. Typical molecules that can act as collisional quenchers include oxygen, halogens, heavy atoms and electron-deficient molecules. The mechanism of quenching varies with the fluorophore–quencher pair. For instance, O_2 is one of the most known quencher, and the quenching is due to a diffusion-controlled process between the oxygen molecule and the exited fluorophore, decreasing the overall photoluminescence [94]. The interaction with heavy atoms occurs due to spin–orbit coupling and intersystem crossing to the triplet state [93].

Fluorescence quenching can also occur via static quenching. This mechanism consists in the formation non-emitting complexes between the chromophore and the quencher. This process is defined static since it occurs in the ground state and does not depend on the diffusion or molecular collisions. Another mechanism that leads to photoluminescence quenching, and that does not involve the presence of an external quencher, is molecular aggregation. Aggregation is typically caused by intermolecular Van der Waals-like forces and it results in distinct changes in the absorption and emission spectrum compared to the isolated molecules. The resulting aggregates will have different optical properties depending on the relative orientation of the monomers and their transition moment. In particular, the two possible aggregation geometries consist in cofacial and head-to-tail aggregation of monomers, leading to the formation of H-aggregates and J-aggregates, respectively.

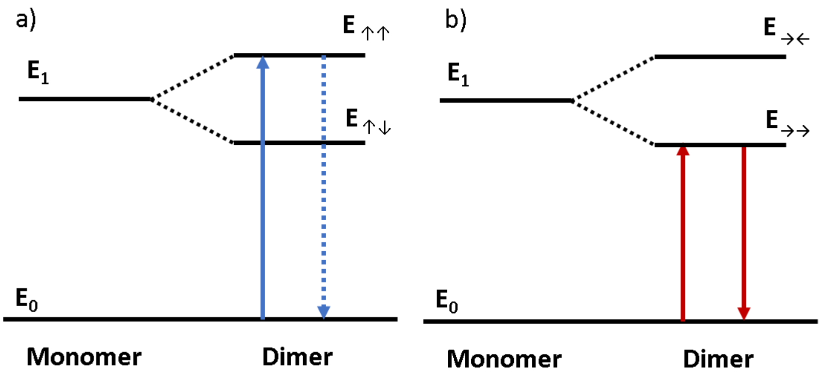

Figure 2.9 Schematic illustration of H- and J-aggregates (exemplified for a dimer) for a π-conjugated molecule (monomer). The ground state of the monomer is indicated as E_0 and lowest excited state as E_1. Depending on the orientation of the interacting dipoles, E_1 splits in two different ways: (a) for cofacial coupling (H-aggregate), the parallel orientation will be at higher energy, while the energy of the antiparallel orientation will be lower than the monomer level E1; (b) for head-to-tail coupling (J-aggregates), the dipole is coupled in one dimension, with the same oriented at lower energy and the opposite oriented at higher energy than the monomer level E_1. Full arrows depict allowed (strong) transitions, and dashed arrows forbidden (or weak) ones.

H-aggregates (figure 2.9(a)) lead to a quenching of the photoluminescence due to unfavourable level splitting. Furthermore, their oscillator strength resides mainly at the top of the exciton band, causing a blue-shift of the optical absorption and intraband relaxation of the excited state results in low or absent photoluminescence [95, 96]. On the other hand, the J-aggregates (figure 2.9(b)) are assemblies of chromophores in which the optically allowed exciton resides at the bottom of the band and they show a red-shift of the optical absorption and high photoluminescence quantum yield [95, 96]. H-aggregates are commonly found in conjugated polymer/molecules thin-films, causing an overall decrease of the photoluminescence quantum yield.

After the photoexcitation, that results in the formation of an electronic excited state on a chromophore, the energy can be transferred to other chromophores via resonance energy transfer (RET) [93].The most important RET mechanisms are the trivial transfer, the Förster fluorescence resonance energy transfer (FRET) and the Dexter energy transfer and can be expressed as:

$$D^* + A \rightarrow D + A^* \tag{26}$$

Where D and A are the donor and the acceptor in the ground state, respectively, and the * indicates the molecule in the excited state.

In the trivial transfer the donor emits a photon that is subsequently absorbed by the acceptor. This process can be long range and its rate depend mainly on the spectral overlap between the emission spectrum of the donor the optical absorption of the acceptor, the photoluminescence quantum yield and extinction coefficient respectively and their relative concentration.

FRET is only for spin-allowed transitions (singlets). The energy transfer process can occur via a resonant dipole-dipole interaction between two point dipoles. Again, the transfer efficiency depends on the spectral overlap between the donor and acceptor, and inversely on the sixth power of the distance between them. Typically, in conjugated polymers the Förster transfer range (defined as Förster radius) is in the order of 10 nm or less.

Dexter transfer involves an electron exchange between the donor and the acceptor. The electron in the excited state from the donor is exchanged for a ground-state electron from the acceptor. Due to its electron exchange nature, the process needs the overlap of the wavefunctions of the chromophores involved and, as a consequence, the transfer efficiency strongly depends on the distance between the donor and acceptor.

In this case there is no dipole-dipole interaction and it is independent of the spin of the electrons involved in the interaction, therefore it occurs both for triplets and singlets.

2.2.2 Time correlated single photon counting (TCSPC)

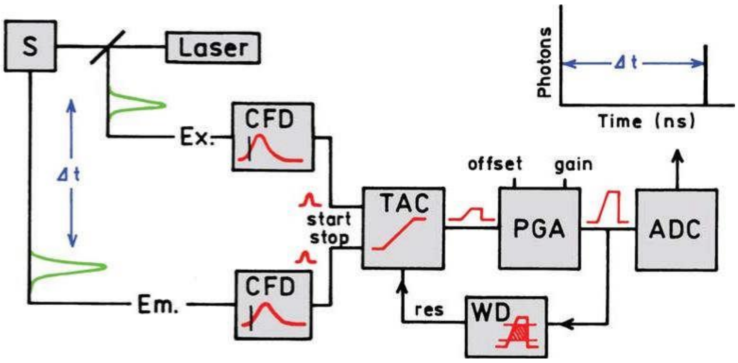

Figure 2.10 Electronics scheme for TCSPC, taken from [93].

The time-correlated single-photon counting (TCSPC) technique is a powerful tool for the measurement of the photoluminescence life [93].This technique is based on the assumption that for low-level, high-repetition-rate signals, the light intensity is so low that the probability of detecting one photon in one excitation pulse is less than 1, with a typical detection rate of 1 photon per 100 excitation pulses. During the measurements the sample is repetitively excited with a pulsed light source (in the order of ps) with a high repetition rate. The system then measures the delay time of each photon emitted by the sample under analysis against the excitation pulse, and, after many cycles, it builds a probability histogram of the photons emitted intensity versus time.

A typical example of a TCSPC electronic schematic is reported in figure 2.10. The experiment starts with the excitation pulse (LASER) that simultaneously excites the sample (S) and sends a signal to the electronics. The signal is passed through a constant fraction discriminator (CFD), which accurately measures the arrival time of the two pulses. Then, the signal coming from the electronic ("start" signal) passes through a to a time-to-amplitude converter (TAC), which generates a voltage that increases linearly with time. As soon as a photon is emitted by the sample ("stop" signal) the TAC is stopped. The arrival time of this pulse is accurately measured using the CFD, which sends a signal to the TAC that now contains a voltage proportional to the delay time between the excitation and the emission signals. Eventually, the voltage is amplified by a programmable gain amplifier (PGA) and converted to a numerical value by the analog-to-digital converter (ADC). The ADC stores each the value for each events and finally the probability histogram is generated summing multiple "start" - "stop" cycles.

A window discriminator (WD) acts as a filter for the generated voltage, suppressing all the signals that does not fall inside a given range, and prevents false readings.

The instrument response function (IRF) of the instruments represents the instrumental response with a zero lifetime emitting sample. It depends on the excitation pulse width and on the timing accuracy of the electronic components.

The final histogram can be fitted by an exponential function to obtain the PL radiative lifetime:

$$\mathrm{I}(t) = \mathrm{I}_0 + \sum_{i=1}^{n} \mathrm{I}_\mathrm{i} e^{-\left(t/\tau_i\right)} \tag{27}$$

Where n is the number of exponential, I_0 a background constant, I_i pre-exponential factors and τ_i lifetime values. The system used in this thesis was an Edinburg Instruments F900-red TCSPC, with pulsed laser-diode (λ_{ex} = 371 nm) with a pulse width of ~60 ps and a cooled photomultiplier tube coupled with a monochromator as detector.

2.3 Organo-Lead Halide Perovskites

The name perovskite identifies the family of minerals that can be described by the generic formula ABX_3; where A is the cation (Ca,Mg,Cs), B is a metallic cation (Ti,Pb,Sn.) and X is the anion (O_2^-, Cl^- I^-;Br^-). The Organo-Metal Halide Perovskite is obtained when in a classical perovskite compound, A is replaced by organic cations, which often, thanks to its reduced size, consists in methylammonium (CH_3NH_2). The ABX_3 tetragonal perovskite-type structure, illustrated in figure 2.11, consists of an extended framework of corner-sharing PbX_6 octahedra (X can be typically Cl, I, Br, or a mix) with the methylammonium cation (MA, $CH_3NH_3^+$) occupying the central A site and surrounded by 12 nearest-neighbour halogen ions [97, 98].

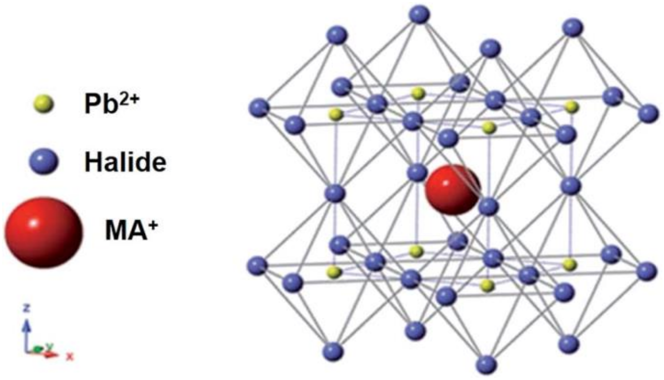

Figure 2.11 Three-dimensional schematic representation of perovskite structure ABX_3 (A = CH_3NH_3,B = Pb, and X = Cl, I, Br), taken from [97].

The crystallographic stability [99] strongly depend on the size of the three ions and it can be defined by two factors: the tolerance factor *t* [100], defined as the ratio between the distance A-X to the distance B-X in an idealized solid-sphere model, and an octahedral factor μ, defined as the ratio R_B/R_X [99]. In particular:

$$t = \frac{R_B+R_X}{\sqrt{2}(R_A+R_x)} \tag{28}$$

where R_A, R_B and R_X are the ionic radii of A, B and X site elements. For halide perovskites (X = F, Cl, Br, I), generally $0.81 < t < 1.11$ and $0.44\ \mu < 0.90$ [99]. The ideal cubic perovskite structure appears in a few cases for t-value very close to unity 1. The physical properties of the perovskites depend crucially on the details of these distortions. For the organic–inorganic halide perovskite, the cation A is the MA with R_A = 0.18 nm, the anion X is a halogen like I, Br and Cl (R_X = 0.220 nm, 0.196 nm and 0.181 nm, respectively), usually in a mixed halide material, and the cation B has universally been Pb (R_B = 0.119 nm).

2.3.1 Perovskite-based photovoltaic devices

The generation of current in a solar cell, defined as the "light-generated current", involves two key processes. The first process is the absorption of incident photons by the photoactive material to create electron-hole pairs and then the separated charges have to be collected.

Every solar cell is characterized by its short circuit current (J_{sc}) and its open circuit voltage (V_{oc}). The J_{sc} is the maximum photocurrent due to the direct connection of the opposite contacts without any load between them, the second is the maximum potential applied (due to an opportune load) to the cell for which the generated photocurrent (J_{photo}) is perfectly balanced by the dark current (J_0), which is the diode leakage current density in the absence of light. Subsequent to the absorption of photons there is the generation of photocurrent, where an electron-hole pair is first generated and then separated and collected by the electrodes.

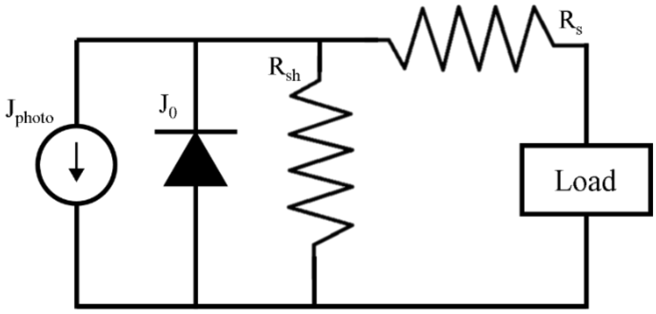

Figure 2.12 Equivalent electric circuit for a real solar cell.

In real cells, whose equivalent electric circuit is reported in figure 2.12, it is important to take into account all the possible recombination channels due to presence of trap states, defects or imperfect interfaces and that cause a diminishing of the net current. Such recombination can be described as series resistance (R_s) and shunt resistance (R_{sh}). In particular, R_s represents the resistance during the movement of current to reach the collecting zone and the entity of R_s depending to mobility of the charges in the crossed mediums and their thickness. Otherwise R_{sh} describes the quantity of charges that recombines before are collected. The entity of both R_s and R_{sh}, depending to characteristics of crossed layer, as purity or intrinsic electronic properties. The most fundamental equation that describes the behavior of solar cells is the diode model:

$$J(V) = J_{photo} - J_0 e^{\left[\frac{q(V+JR_S)}{nk_BT} - 1\right]} - \frac{VR_S}{R_{sh}} \tag{29}$$

where J is the current density measured at the cell electrodes, V is the voltage measured across the cell, J_{photo} is the photogenerated current density, J_0 is the reverse saturation current density, q is the elementary charge, R_s is the series resistance, R_{sh} is the shunt resistance, k_B is the Boltzmann constant, T is the absolute temperature, and n is the ideality factor.

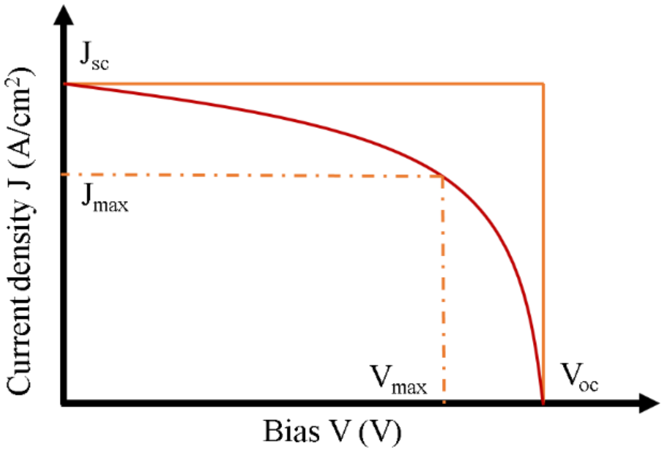

Figure 2.13 J-V curve (in red) of a real device. The operating point with the maxima power is identified by pair (Jmax; Vmax).

The performance of a photovoltaic device can be expressed in term of efficiency. In particular, the external quantum efficiency (EQE) is the ratio of the number of carriers collected by the solar cell to the number of photons of a given energy E incident on the solar cell and therefore it is correlated to the J_{sc}:

$$Jsc = q \int s \, EQE \, dE \tag{30}$$

where s is the incident spectrum, and q is the elementary charge.

Another way to indicate the performance of a photovoltaic is with the ratio between the maximum output power (P_{max}) and the power of the incoming irradiation (P_{in}), defined as the power conversion efficiency:

$$\eta = Pmax/Pin \tag{31}$$

The electrical power delivered in every operating point is given by P = JV, whose maximum (P_{max}) occurs at specific potential V_{max} and current J_{max} (figure 2.13). In ideal case, i.e. excluding both R_s and R_{sh}, these values correspond to V_{oc} and J_{sc}

The difference between the real power P_{max} that can be extracted by the solar cell and the ideal power is the fill factor (FF):

$$FF = V_{max}J_{max}/V_{oc}J_{sc} \tag{32}$$

As a consequence, the FF is affected by the series and shunt resistances, which in turn are affected by the carrier mobility and balance, interface recombination, and film morphology [101, 102].

A basic device structure of solar cell features an active layer, which is responsible of absorbing the incoming light and generate the free charges, sandwiched between a transparent and a metallic electrode. In particular, in the case of the perovskite-based solar cells, the devices can be assembled in two different structures: the planar heterojunction and the meso-superstructured. As shown in figure 2.14(a), the various layers for the latter are: the transparent electrode (the anode), that most commonly is a layer of fluorinated-tin oxide (FTO) sputtered on a glass substrate; the electron transporting layer (ETL) that consist in an oxide semiconductor (e.g. titania) having a band alignment to favor the transfer of electrons to the anode; a mesoporous oxide scaffold, to enhance light absorption due to scattering; the perovskite, i.e. the light harvester medium that creates carriers following to the absorption of photons and finally the hole transporting layer (HTL), that has specular activity with respect to electron transport layer described before, and the metal contact. On the other hand, in a planar junction perovskite solar cell (figure 2.14(b)), a several hundred nanometer thick absorber layer is sandwiched between the ETL and the HTL without any mesoporous scaffold. Since the hybrid perovskite has been shown to exhibit ambipolar charge transport [103], this architecture offers the advantage that can be built in direct and inverted structures, i.e. with the transparent anode with a structure like FTO/ETL/perovskite/HTL/metal, or with a transparent cathode, resulting in a structure like FTO/HTL/perovskite/ETL/metal, respectively

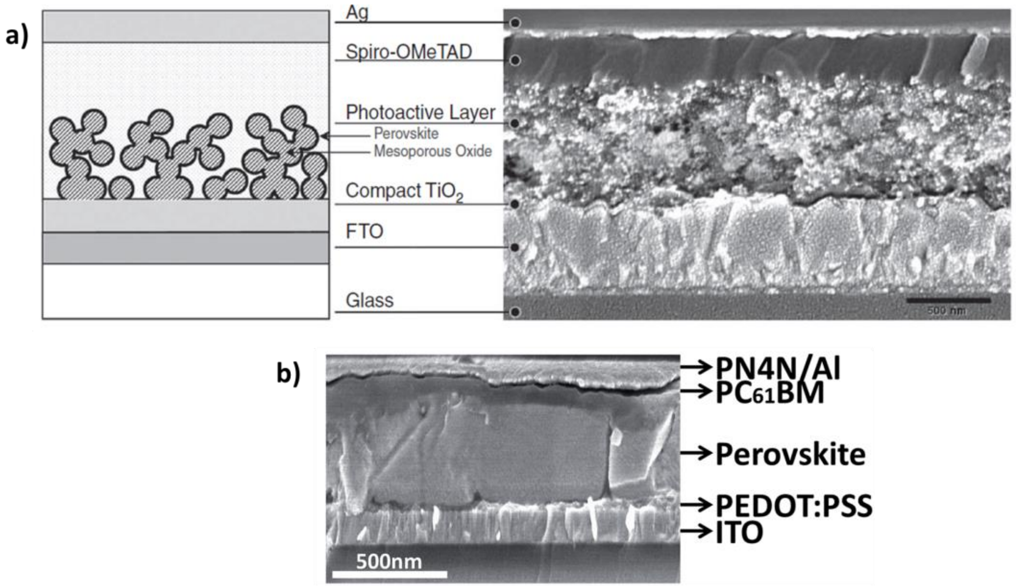

Figure 2.14 (a) Schematic mesostructured device architecture (on the left) and cross-sectional SEM image of the device structure, taken from ref. [98].The transparent electrode is the fluorinated-tin oxide (FTO), on top of it there is a compact layer of titania (TiO_2) and the mesoporous oxide. The perovskite is the photoactive layers, and it is infiltrated into the mesoporous scaffold. Than the structure is capped with the hole transporter (in this case it is the spiro-OMeTAD) and the cathode. (b) Cross-sectional SEM of a planar heterojunction device. In particular this is the inverted architecture, with the transparent cathode (ITO) in the bottom. Taken from ref. [104].

When a photon is absorbed by the perovskite, an exciton is generated and it propagates just until the interface perovskite/ETL. At this point the exciton is separated into an electron and a hole, which are collected respectively forward ETL and HTL. In order to have an optimal exciton dissociation into free charges, the energy levels of the various layers have to be properly aligned, such as the one showed in figure 2.15.

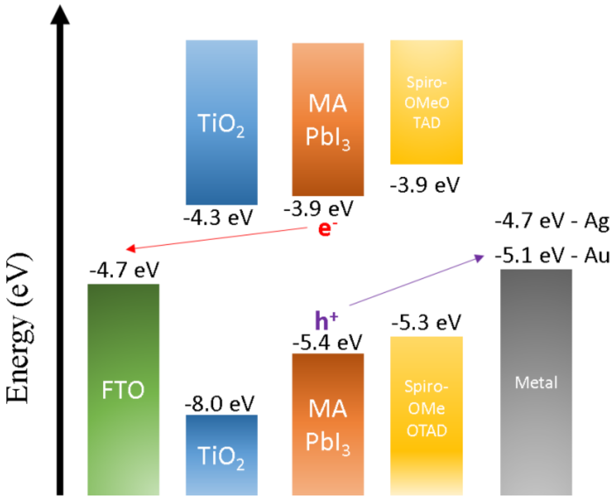

Figure 2.15 Schematic energy diagram of a solar cell in direct configuration, using FTO as transparent electrode, TiO_2 as ETL, Organo-Lead Perovskite ($(CH_3NH_3)PbI_3$) as active layer, Spiro-OMeOTAD as HTL and a generic metallic contact.

The J-V curves, both in dark, to evaluate the diode characteristics and under illumination, to obtain the device efficiency, of the photovoltaic cells are measured using a source-measure-unit connected to a computer and illuminating with a solar simulator (in our case the instrument was model Sun 3000 11016A from ABET Technologies).

Chapter 3

Polymer-silicon hybrid photonic structures

In this chapter I report on the modification of the photoluminescence (PL) and decay rates of a green-emitting commercial luminescent polymer (F8BT, poly[(9,9-di-n-octylfluorenyl-2,7-diyl)-alt-(benzo[2,1,3]thiadiazol-4,8-diyl)]) infiltrated into one-dimensional (1D) porous silicon photonic crystals (PS-PhCs), known as rugate filters, whose detailed inner morphology I analyse with the help of (scanning) transmission electron microscopy, (S)TEM, and scanning-electron microscopy, SEM, of focused ion-beam (FIB) milled sections. I observe both suppression (in the stop-band) and enhancement (at the high-energy band-edge) of the photoluminescence. Corroborating time-resolved measurements reveal a concomitant modification of the emission lifetime that is enhanced at the band-edge and suppressed within the stop-band, thus confirming a variation of the radiative decay rate of the excitations in such hybrid organic-inorganic photonic nanostructures. I also find that the photonic stop-band is red-shifted after polymer infiltration, due to the increased effective refractive index of the polymer-infiltrated nanostructured system. The presence of just one unbroadened peak in the reflectance spectra after infiltration suggests that infiltration extends for the whole depth of the rugate filters. I assign the alteration of the emission of F8BT to the modification of the density of photonic states within the photonic crystal. The following chapter is reproduced by permission of Springer (see ref. [58]).

3.1 Hybrid photonic structures for light emission modification

Photonic crystals provide perhaps the most powerful tool for manipulation of light generation and propagation, thereby potentially enabling the implementation of photonics as the most performing information and communication technology (ICT) platform. As such, PhCs have been intensely studied over the last three decades especially with a view to combining them with photoactive materials such as luminescent (macro)molecules and inorganic semiconductors,[105, 106] or with plasmonic nanostructures, so as to achieve directional modification of the fluorescence,[107-110] optically-pumped lasing,[67, 111] and optical switching[112, 113] among other aims. In this context, microcavities have been widely used to control and enhance the emissive properties of conjugated polymers [114-116]. Notably, porous silicon-based PhCs, such as rugate filters [117], have attracted significant interest since they provide a straightforward and technologically robust route to fabrication of optical nanostructures with significant levels of complexity, while at the same time building on an unrivalled silicon-based micro- and nano-technology. Indeed, this class of photonic systems has been used widely for optoelectronic [118], photonic [119], sensing [5, 120] and biological applications [121]. In particular, rugate filters are good candidates as vapor and liquid sensors [122-124], and as detectors for biological activities such as proteases [125, 126].

Several ways to fabricate hybrid polymeric-inorganic structures have been reported in the literature so far, but in most cases the preparation involved a “chemical approach”, namely: the growth of the target macro-molecules “in situ” by chemically reacting smaller monomers that can be easily infiltrated inside the pores [127]. This has been exemplified by either electrochemical deposition [128, 129] or in-situ chemical polymerization [130] of suitable monomers. Although the efficiency of such processes is relatively high (in terms of pore filling and/or monomer conversion), the applicability of this method is limited to a relatively narrow set of monomers, and therefore not generally applicable.

For this reason the preparation of hybrid Si-organic structures via a solution processable method, i.e. by directly infiltrating the polymer inside the pores starting from a solution, is more attractive [120]. This procedure requires a good optimization of the infiltration methodology to successfully infiltrate the polymer inside the pores, especially if pore sizes are comparable to the polymers gyration radii (typically a few nm), or to the size of aggregated/phase-separated macromolecular meso-structures (up to tens of nm).

Electrochemically etched pores are in the tens to few hundreds of nm diameter, depending on the etching parameters, thereby complicating the observation. However, gathering details on the diameter and chemical nature (e.g. following partial oxidation) of the pores, is particularly important with a view to infiltration of the latter with soft matter (e.g. luminescent materials, but also, in perspective, biologically-active (macro)molecules).

Interestingly, I found that pore-clogging was not a particularly significant problem in our hybrid PhCs obtained via infiltration of commercial poly(9,9'-dioctylfluorene-alt-benzothiadiazole), F8BT (Mw ~ 46 kDa) into porous silicon. Upon infiltration I observe shifts of the filters reflectance peaks that are consistent with coating of the inner walls of the pores to the whole depth that can be probed in such optical experiments. I consider that the ability to infiltrate the porous structures results from the particular relation between the limited polymers gyration radius (R_g, of the order of few nm) and the minimum pore sizes (approximately 10 times as large as R_g) for which I obtain direct insight by means of electron microscopy.

Importantly, I find that the luminescence of the infiltrated macromolecular luminophore is controlled by the photonic structure of the inorganic host, and shows an enhancement at the high-energy end, and suppression at the low-energy end, of the photonic band. In general, I consider that these polymer-infiltrated Si-based crystals powerfully exemplify an element of a potential tool library of a “C-Si hybrid photonic platform”. Such a platform could be developed for a multitude of applications, spanning from bio-sensors to high-capacity/high-speed data-handling devices (e.g. for “Big-Data”), in a complementary or even alternative fashion to Si/III-V hybrids.

3.2 Experimental details

Porous silicon rugate filters were prepared by Prof. G. Barillaro's group in University of Pisa, Information Engineering Department. Porous silicon rugate filters featuring a stop-band in reflectance either in the visible or near-infrared range were prepared by electrochemical etching of (100)-oriented, highly doped p-type silicon wafers (boron-doped, resistivity 0.0008–0.0012 Ω cm, from Siltronix Corp.) in a 3:1 (by vol.) solution of 48% (by vol.) aqueous hydrofluoric acid and ethanol (both from Sigma Aldrich). The electrochemical etching was performed in a home-made Teflon cell using a two-electrode configuration, with the silicon substrate acting as anode (working electrode) and a platinum ring immersed in the solution acting as cathode (and used as pseudo-reference electrode). A source-measure unit (Keithley 2410 Source Meter) was used to impose the desired etching current density and to monitor the voltage drop between the silicon sample and the pseudo-reference electrode. The hydrofluoric acid solution was stirred during the electrochemical etching so as to minimize hydrogen bubble formation on the sample surface and enhance etching uniformity.

A cosine-shaped current density waveform with peak-to-peak dynamics from 13.3 to 39.9 mA/cm^2, 50 repeats, and time period of 11 and 17.5 s was used to produce rugate filters with a stop-band in reflectance centred at 551 nm and 827 nm, respectively before oxidation, and shifting to 515 nm and 771 nm respectively after oxidation. Such an etching current density waveform produces mesostructured porous silicon samples with periodic porosity (values between 62.5 % and 69.5 %, with an average P_{avg} = 66%) and, in turn, with periodic refractive index (oscillating between n_{min} = 1.69 refractive index units, RIU, and n_{max} = 1.93 RIU – n_{eff} = 1.81 @ 551 nm, yielding a maximum contrast of 0.26 RIU, and between n_{min} = 1.61 RIU, and n_{max} = 1.83 RIU – n_{eff} = 1.72 @ 827 nm). I estimated the values of porosity and, in turn, of the effective refractive index from the experimental reflectivity spectra of porous silicon layers etched with constant current density of either 13.3 or 39.9 mA/cm^2. These correspond to minimum and maximum values of the cosine-shaped current density waveform used for rugate filter etching, respectively, according to the procedure described in the work by Ruminski *et al.*[122].

The effective refractive index has been determined by using the so called Bruggeman's model/equation. For the as-fabricated samples the effective refractive index has been calculated simply by considering the porosity of the samples, instead, for the oxidized samples, it was necessary to take into account a three component model, since I had to estimate the silicon oxide fraction to obtain the best fitting with the reflectance spectra. [123].

To improve the infiltration process and prevent emission quenching by the heavily-doped silicon layer, the rugate filters were partially oxidized into a tube furnace (ThermoLyne 21100) under pure-O2 (99.999%) at 600 °C for 30 min prior to infiltration.

F8BT infiltration into the cavities of the filters was obtained using a dip-coating procedure [131] by first submerging the rugate filter into a toluene solution of the polymer, and then by slowly extracting it. The procedure was carried out at a controlled lifting rate (0.01 mm/min) and temperature (29 °C). The excess polymer left onto the surface after dip-coating was removed using a cotton swab soaked with toluene.

Normal incidence and angle-resolved reflectance spectra were collected with an Ocean Optics S2000 spectrometer in combination with a fibre-coupled Ocean Optics HL-2000 tungsten halogen source. Steady-state angle-resolved photoluminescence measurements were carried out by using a 405nm CW laser diode (Thorlabs) and an Andor Shamrock 163i spectrometer coupled to an Andor Newton CCD camera cooled at -50 °C. Time-resolved PL measurements were carried out with a time-correlated single-photon counting, TCSPC, spectrometer (F900 Edinburgh instruments) with excitation provided by a pulsed laser diode (λ_{ex} = 371 nm, pulse-width ~ 60 ps).

FIB-SEM images have been taken by using a Carl Zeiss XB1540 "Cross-Beam" focused-ion-beam microscope, whereas ion-beam milling of the samples was carried out using Ar atoms. TEM-STEM images have been taken by using a Titan 80/300 TEM/STEM. This instrument is fitted with a monochromator to deliver spatial/energy resolution capabilities of 0.14 nm/0.5 eV (monochromator off) and 0.3 nm/0.12 eV (monochromator on).

3.3 Morphological characterization

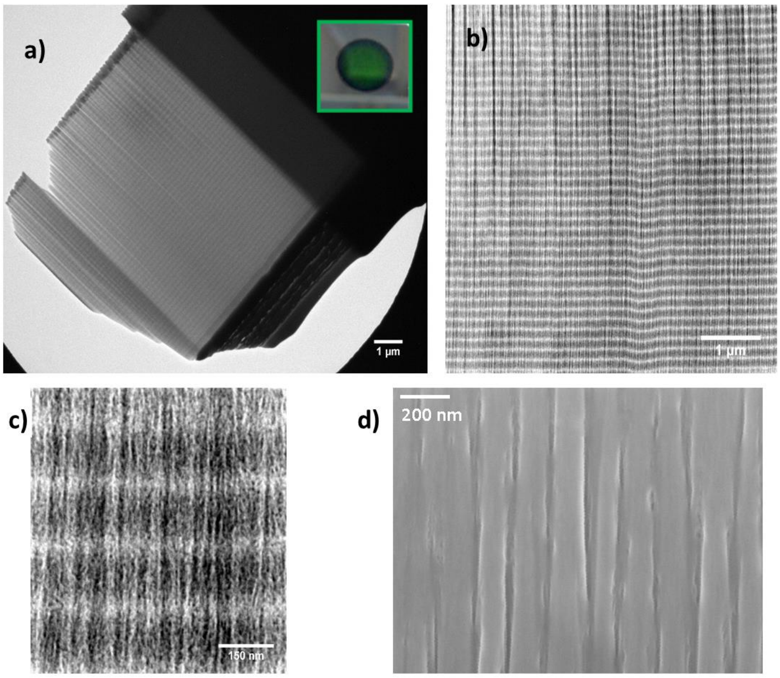

Figure 3.1 TEM/STEM images of rugate filter with reference peak (After infiltration) at 515 nm. (a) Bright-field TEM image of the rugate filter (inset: photo of the same rugate filter). (b) bright-field STEM overview image of the PhC (c) High Angle Annular Dark-Field zoom of the internal structure (d) SEM image of a FIB-milled cross-section of the rugate filter at 515 nm detailing the pore structure, with pore sizes on the order of 50 nm or so. Bright areas on the edge of the solid Si pillars are associated with regions of more intense charging, and are thus assigned as rich in oxidised silicon, with a typical thickness of 10 nm or so.

Figure 3.1 shows transmission electron microscope, TEM (a), and scanning TEM, STEM (b, c), cross-sectional images of the rugate filters with “initial” (i.e. before oxidation) stop-band at 551 nm, at different magnifications. Notably, the periodic modulation of the porosity of silicon along the direction perpendicular to the surface can be clearly observed as darker/brighter alternating regions in all TEM/STEM images (a, b, and c). The quality of the “overview” figure 3.1(a) is good enough to enable counting the total number of layers (50) and measuring the total thickness of the rugate filter (~ 7.6 μm). The sample has been covered with a Pt layer (darker layer on the top of the structure) to protect the structure during the ion etching carried out to obtain the slice for the TEM analysis. In figure 3.1(c) I report a zoomed-in STEM image of the photonic structure, which shows a clear asymmetry in the bright and dark regions in each period, thereby suggesting that the refracting index modulation is different from sinusoidal, despite the sinusoidal etching current. I consider that this is likely due to current density-dependent etching rates [132]. In figure 3.1(d) I report an SEM image of a FIB-milled cross-section where it is possible to observe the inner part of the pores. Along their thickness I note the presence of (somewhat discontinuous) brighter areas or spots that can be readily associated to relatively insulating regions (charging up and therefore appearing brighter in the images). The question arises as to whether such low-conductivity regions are to be identified with the Si oxide or with the infiltrated polymer. It is possible to interpret such areas as the oxidized inner layer of the cavities, because: (i) the "characteristic" thickness of 10 nm or so is consistent with what expected on the basis of the oxidation parameters and with Bruggeman's modeling of the oxidized but not infiltrated filter, (ii) the shift of the reflectivity peak of the filter upon infiltration (reported below) is only 12 nm or so, therefore consistent with a 2-3 nm thick polymer layer (which we cannot detect at the resolution of this image).

The interplanar spacing D by inspection of figure 3.1(b), is ~ 150 nm, consistent with the total thickness and the number of current periods. Such a value is further confirmed by 2-dimensional Fast Fourier Transform (2D-FFT) analysis of figure 3.1(b) reported in figure 3.2. The FFT peaks spacing is 6.67 μm-1 (corresponding to 150 nm). The presence of bright lines denotes a high uniformity of the (vertical) periods over the entire surface of the slice, but a much lower uniformity of the pillars and pores dimension.

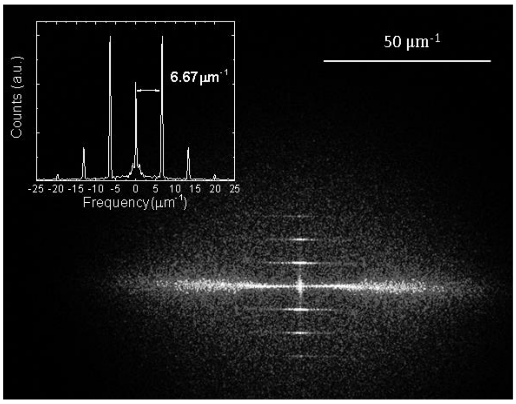

Figure 3.2 2D-FFT transform (inset: frequency profile extracted from the 2D-FFT, the distance between the lines is found to be 6.67 μm-1).

I also analyzed the structure of figure 3.1(a) along its depth at higher magnification. In figure 3.3 I present two TEM cross-sections taken at the same magnification (12000 magnifications) in the top (a) and in bottom (b) section of the rugate filter. Despite some small oscillations in the layers in the top part of sample, the interplanar distances appear nearly perfectly matched in both parts, as highlighted by the two parallel dashed lines. The only exception is the very last layer etched (in the bottom part of the sample) which is smaller than the other ones.

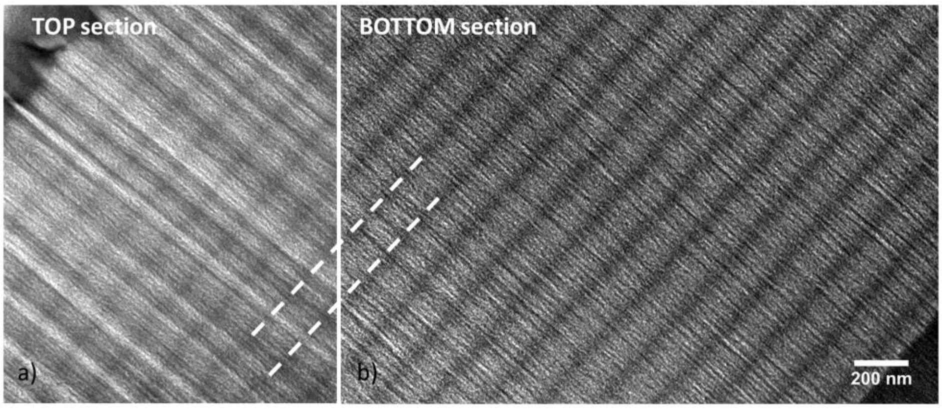

Figure 3.3 Bright-field TEM images taken at 12000 magnifications with 0.5 s exposure in the top and bottom part of the rugate filter.

3.4 Optical characterization

In figure 3.4 I report the reflectance spectra of both rugate filters (i.e. tuned (a) and detuned (b)) before (red line) and after the dry oxidation process (blue line). For the tuned sample (figure 3.4(a)), the reflectance peak is blue-shifted by ~33±1 nm due to the formation of an oxide layer and, in turn, a different effective refractive index. This is also confirmed by the lowering of the total reflectance induced by the lowering of the dielectric contrast. Considering this blue-shift and the determination of the interplanar spacing via STEM imaging analysis, according to the Bruggeman's equation, the silicon oxide fraction formed during the oxidation process should be ~10 nm. For the rugate filters with initial (i.e. before oxidation) stop-band at 827 nm (figure 3.4(b)) the blue-shift of the reflectance peak is about 56 nm. The intaplanar spacing D is found to be ~240 nm and it has been evaluated by the reflectance measurements and taking into account the thickness of the oxide determined for the "green" rugate filter.

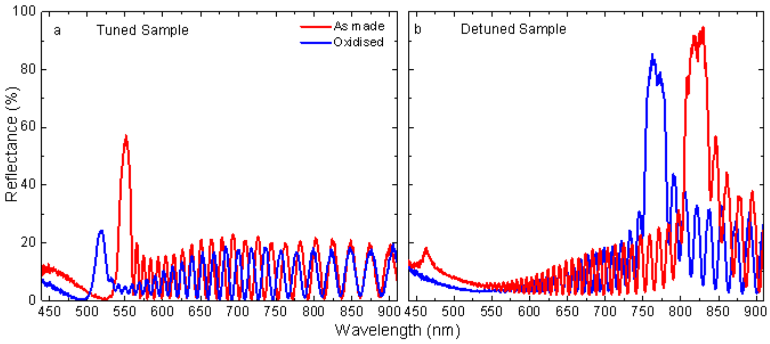

Figure 3.4 Reflectance spectra of the tuned (a) and detuned (b) rugate filter before (red line) and after (blue line) the oxidation process.

To determine the effect of the photonic structure on the F8BT spectrum I compared the optical properties of the filter with the stop-band centred at 515 nm (after oxidation, red-shifting by about 12 nm upon infiltration, thus providing significant spectral overlap with the F8BT PL, and hence referred to as “tuned” filter) with those of the “detuned” filter (stop-band centred at 771 nm, after oxidation, further red-shifting upon infiltration) that is used as a reference.

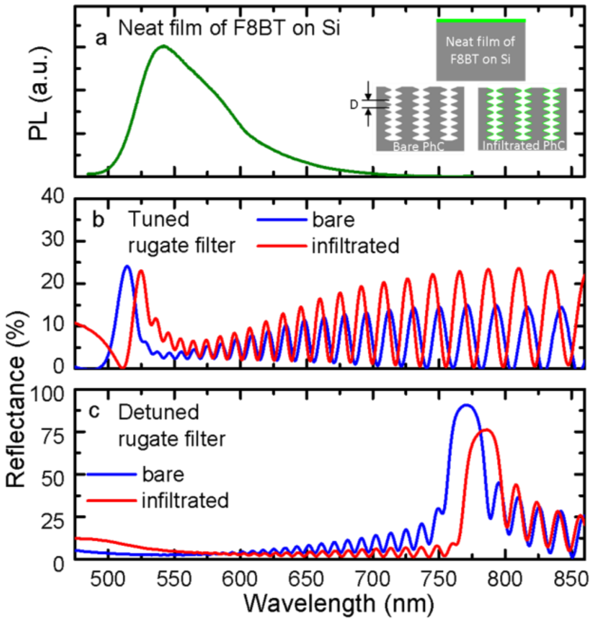

Figure 3.5 (a) PL spectrum of a neat film of F8BT on a compact silicon substrate, and (b and c) reflectance spectra for the PhCs before (blue) and after polymer infiltration (red). The infiltration leads to a red-shift of the photonic stop-band (and thus of the reflectance peak) of about 12±1 nm. Note that the vertical scales for (b) and (c) are different, i.e 40% and 100% reflectance, respectively. Inset: cartoon illustrating the inferred cross-section of the rugate filter (D is the inter-planar spacing determined by the period of the anodic etching current); the polymer layer is not filling the pores of the rugate filters, but there is just a layer on the walls of the cavities (see main text for discussion). The structure of the sample used to measure the F8BT PL is also shown.

Figure 3.5 shows the typical PL spectrum of an F8BT film (panel a) and the reflectance spectra for tuned (panel b) and detuned samples (panel c) before and after the infiltration of the F8BT, at normal incidence. I could not detect any PL from the bare porous silicon for both tuned and detuned samples.

Upon polymer infiltration the reflectance peaks red-shifted by ~ 12±1 nm in both samples due to the increased effective refractive index. In particular the reflectance peak for the tuned sample red-shifted from 515 nm to 526 nm after infiltration and for the detuned one it red-shifted from 771 nm to 784 nm. This is in qualitative agreement with the prediction of the Bragg-Snell law (Eq. 17), which can then be used to quantify the effective refractive index n_{eff} [133].

From Eq. 17, I determine $n_{eff} = 1.81$ and 1.72 for the as-fabricated rugate filters, for interplanar spacing D of 150 nm and 240 nm as obtained from TEM images for the rugate with stop-band peaks (before oxidation) at 551 nm and 827 nm, respectively.

As a further check, the total thickness (t) of the nanostructured samples can also be calculated by using the interference fringes in the reflectance spectra once the effective refractive index of the photonic crystal is known:

$$t = \frac{N_{fringes}}{2n_{eff}\Delta\nu} \tag{33}$$

where $N_{fringes}$ is the number of fringes within the spectral range $\Delta\nu$ (in cm^{-1}). By using the effective refractive indices obtained with the Bragg-Snell's law, and a spectral range of ~4800 cm^{-1} for the tuned sample and ~3000 cm^{-1} for the detuned one, I found $t = 7.6$ μm for the tuned filter (which is in excellent agreement with the SEM/TEM observations) and $t = 12$ μm for the detuned one.

Considering that the refractive indices of F8BT are 1.6 (extraordinary one) and 1.8 (ordinary one) [134] and the refractive index of air is 1, I would have expected a spectral shift of the reflectance peaks bigger than the observed one if the cavities had been completely filled by the polymer. In fact, in the case of a complete filling of the cavities with the F8BT (i.e. totally removing the contribution of the air to the effective refractive index and replacing that with the one of the polymer in the Bruggeman's model) the reflectance peaks of the two rugate filters would have moved from 515 nm to 634 nm (119 nm shift) and from 771 nm to 960 nm (189 nm shift) for the tuned and detuned filter, respectively.

Having established that infiltration leads to a "coating" of the pores walls, rather than to "solid filling" of the pores with the polymer, an interesting question arises as to whether such a "coating" is complete or partial in the vertical direction. In fact, partial "coating" of the pores is excluded by the SEM and (S)TEM micrographs (figure 3.1), that do not show any such evidence, and by the optical measurements providing evidence for just one un-broadened reflectance peak [135]. In fact, partial filling/coating along the pore's depth should have resulted in two reflectance peaks as in the presence of two PhCs stacked one over the other: the one made by Si and air and the one made by Si/polymer and air [136]. Since the shift of the reflectance peak upon infiltration is 12±1 nm, any such a peak should be clearly observable in the overall reflectance spectrum, unless the one associated to the "empty" fraction of the pores is particularly small compared to the other. In practice, given the intensity resolution with which I was able to measure the spectral features, I can estimate that the pores are coated to well over 99% of their depth.

To observe the modification of the PL spectra induced by the photonic crystal, I compared the PL of the F8BT infiltrated into the tuned and detuned (reference) filters, to avoid those small differences in the surface chemistry of the porous silicon samples affected the determination of the photonic effects. The PL spectra were then normalized with respect to the intensity at $\lambda = 550$ nm, i.e. several tens of nm away from the centre of the photonic stop-band [136].

In Figure 3.6(a) I report the PL spectra as a function of the angle of incidence of the exciting laser beam for both tuned and de-tuned infiltrated filters (only at normal incidence for the detuned sample, as there is no angular dependence). Clearly, F8BT's photoluminescence is strongly modified by the presence of both the stop-band and of the interference fringes, which contribute both to "structuring" the emission. Remarkably, the PBG suppresses (albeit partially) propagation at 528 nm (at 0◦ incidence) and increases the intensity at the high-energy edge (from 518 nm at 0° incidence to 503 nm at 30° incidence). This is in agreement with the expected suppression of the photonic density of states (DOS) in (the middle of) the stop-band, and with its increase at the stop-band high-energy edge [137] and it will be demonstrated below by mean of radiative lifetime measurements. Such enhancement and the suppression display strong dependence on the excitation angle, because of the dispersion of the stop-band.

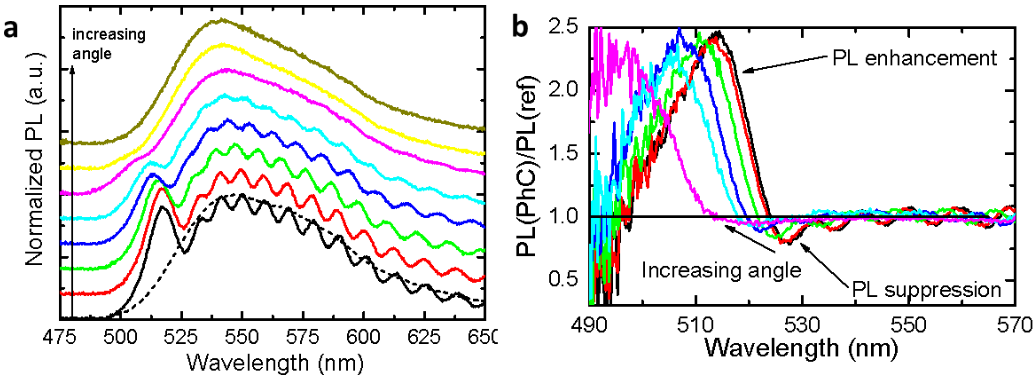

Figure 3.6 (a) PL spectra (solid lines) collected at different incidence angle (from 0° to25° with step of 5°) of the exciting beam for F8BT infiltrated into the tuned PhC and at 0° for the F8BT infiltrated into the detuned PhC (dashed line). I used a CW laser, emitting at 405 nm, as excitation source. I can observe the PL peak dispersion moving from 518 nm at 0° to 506 nm at 25°. (b) Ratio between the PL spectra from the tuned and detuned PhC at different angles, as in (a) above.

The enhancement/suppression above is appreciated clearly in Figure 3.6(b) in which I have plotted the ratio (R_n) between the PL spectra of infiltrated tuned filter and detuned filters. Thus figure 3.6(b) emphasises both enhancement ($R_n > 1$) in the region between 518 and 506 nm and a minor suppression ($R_n < 1$) at the stop-band (between 528 and 512 nm) for angle increasing from 0° (normal incidence) and 25°. The difference in the intensity of the suppression and enhancement could be explained as the difference in the experimental set-up for the two samples (film thickness, laser spot size) and to refractive-index effects [138].

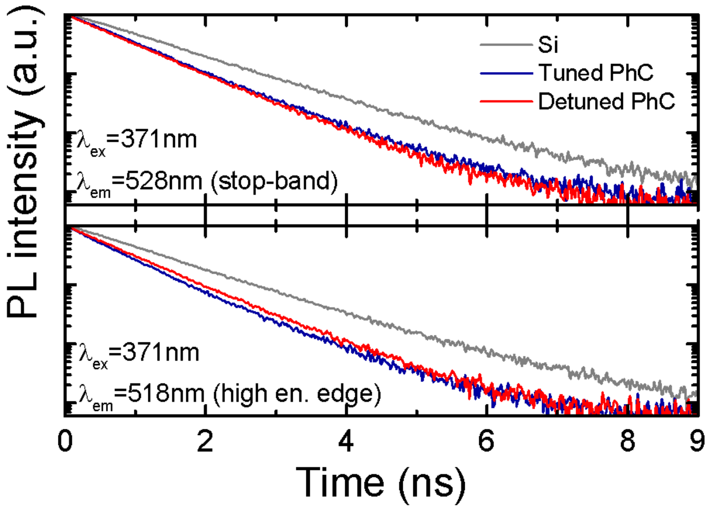

Figure 3.7 Radiative decay of the F8BT PL measured by time-correlated single-photon counting, TCSPC (371 nm excitation) and recorded either within the stop-band (528 nm, top panel) and at the high-energy edge (518 nm, bottom panel) for a neat F8BT film on Si, as well as for F8BT infiltrated into the tuned and detuned filters, as indicated in the plots legends.

Finally, to obtain conclusive evidence about the modification of the radiative rate of F8BT induced by the “photonic host” (i.e. the rugate filters) I measured the PL temporal decay (figure 3.7) both within the stop-band (528 nm) and at the high-energy edge of the latter (518 nm). I focused on these two spectral lines because at such wavelengths there is a clear modification of the DOS.

The results for a neat F8BT film (thickness ~ 800 nm) on Si deposited by dip-coating, are in good agreement with previous works [139-142] showing a mono-exponential PL decay for neat films of F8BT deposited by spin-coating, with lifetimes varying from 0.89 to 1.84 ns depending on wavelength, film thickness and substrate materials. In this case, I obtained decay times of ~ 1.15 ns at 518 nm and ~ 1.18 ns at 528 nm, table 3.1). However, when the polymer is infiltrated in the tuned and detuned PhCs, I find that accurate fits of the PL temporal decay can only be obtained with a “bi-exponential” equation [60], with characteristic lifetimes as reported in table 3.1 below.

The need for a bi-exponential fit for the infiltrated polymer is not surprising, given the large area/volume ratio of the regions in which the polymer is accommodated, and for which a relatively strong interaction with the SiO_2/porous silicon can be expected, both of a chemical and of a physical nature which are likely to lead to different strand packing patterns and likely formation of weakly-bound interchain states in addition to the monomolecular singlet excitons that characterise the emission of the neat thin films. In general, the photoluminescence of conjugated semiconductors is a sensitive probe of their chemico-physical environment, and of the geometry adopted by the polymeric strands. Similar effects have been noted both when adsorbing similar chromophores on nanospheres in three-dimensional self-assembled opals[110] or in the presence of strong interchain interactions for a variety of conjugated polymers, including F8BT [143, 144]. While such interactions might differ significantly for the infiltrated F8BT with respect to the one on neat Si, they should be very similar for the tuned and detuned filters, thereby enabling a meaningful comparison.

	τ_1 (ps)(I_1)	**τ_2 (ps) (I_2)**
High-energy edge		
Tuned PhC	690±34 (0.8)	1210±60 (0.2)
Detuned PhC	830±41 (0.95)	1590±79 (0.05)
Film on Si	1150±57	
Stop-band		
Tuned PhC	860±43 (0.94)	1680±84 (0.06)
Detuned PhC	830±41 (0.95)	1600±80 (0.05)
Film on Si	1180±59	

Table 3.1 Temporal decay constants ($\tau1$, $\tau2$) extracted from least square fits of the PL decay curves with their relative weight (I1, I2).

It is thus very interesting to observe a very clear reduction of both lifetimes (table 3.1) at the high-energy edge of the stop-band (518nm) for the tuned with respect to the (detuned) reference filter (~17% of τ_1 and ~24% τ_2 for the mean). As expected, I also find slightly longer time constants within the stop-band (528 nm) (by ~4% for τ_1 and ~5% for τ_2). Note also that the less significant variation within the stop-band (effectively comparable with the error) is fully consistent with a much less important suppression of the emission in this region, as compared to the enhancement at the band edge (as also evidenced by figure 3.6). Such apparently limited differences between the radiative decay rates of F8BT within tuned/detuned filters are entirely within expectations for one-dimensional (1D) photonic structures such as rugate filters, that only provide intrinsically limited “photonic confinement” (i.e. only along the z-direction) and that a narrow spectral width (516 – 533 nm) compared to the PL of the F8BT guest (490 – 700 nm) [145].

3.5 Conclusion

In conclusion I have investigated a hybrid silicon-organic photonic system. I achieved excellent infiltration of the green-emitting highly luminescent F8BT into rugate filter cavities whose detailed nano-/meso-structure I carefully analysed via (S)TEM and SEM. F8BT infiltration into the rugate filters leads to a red-shift of the stop-band and brings about a wavelength- and angle-dependent PL suppression-enhancement due to the presence of the photonic stop-band. A modification of the emission lifetime at the stop-band high-energy edge is clearly observed and assigned to the modulation of the photonic density of states imposed by the conjugated polymer.

Chapter 4

Spectroscopy of synthetic opals

In this chapter I present a spectroscopic investigation of a particular class of 3D photonic crystals, synthetic opals. In particular, I describe a simple bottom-up approach for preparing photonic crystals from a water suspension of polystyrene microspheres and how to introduce supramolecularly engineered luminescent polymers to observe suppression-enhancement in their photoluminescence spectrum. Secondly I present transmission experiment to explore the Bragg-Snell's law for the determination of the effective refractive index.

The following chapter is reproduced by permission of AIP Publishing LLC., Copyright 2016 (see ref. [110]) and of American Association of Physics Teachers (see ref. [146]).

4.1 Synthetic opals

Even though PhCs are mainly prepared by top–down methods, the bottom–up approach seems very promising in order to tailor the system for specific applications [147]. In this scenario, colloidal photonic crystals, e.g synthetic opals [148] (figure 4.1), are very interesting due to their low fabrication cost and ease of preparation.

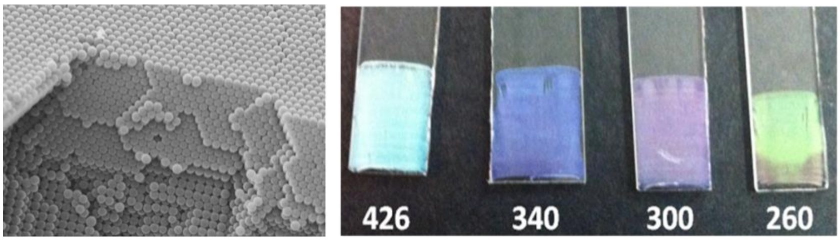

Figure 4.1 SEM image of the opal structure (left) and photo of opals made with different microspheres diameter (right), the diameter (in nm) is indicated below the opals. The reflected color changes as function of the dimension, according to Bragg-Snell's law.

Opals are in fact a versatile system that can enable the investigation of a variety of photonic effects and especially the fine-tuning of optical properties [149], including the modification of the emission spectra and radiative rates [110], optical switching [150], and hybrid photonic-plasmonic like resonances [113]. Different active materials such as metal nanoparticles [151], semiconductor nanocrystals [152] or conjugated molecules [153], can be effectively incorporated into the opals in by means of infiltration, co-growth or evaporation.

Opals are 3D photonic crystals assembled in a face-centred-cubic (FCC) structure of dielectric microspheres (figure 4.1). Such structures can be prepared by many bottom-up approaches, exploiting the spontaneous assembly of the micospheres into the crystalline structure. The dielectric contrast of the media composing the opals is given by the refractive index of air (n = 1) and of the material used for the microspheres.

To evaluate the effective refractive index of the opals, but more in general of a PhCs, I can use Lorentz-Lorenz equation [153]:

$$\frac{n_{eff}^2-1}{n_{eff}^2+2} = \sum f_1 \frac{n_1^2-1}{n_1^2+2} + f_2 \frac{n_2^2-1}{n_2^2+2} \quad (34)$$

Where n_{eff} is the effective refractive index, n_1 is the refractive index of vacuum (n_1=1), n_2 is the refractive index of the material used and $f_{1\&2}$ the volume fractions of the two media. In particular, f_2 = 0.74 for a face-centred-cubic structure.

As reported in figure 4.2, opals cannot have a complete photonic band-gap (i.e. a photonic gap for all the values of k) even with extremely high dielectric contrast, but only a stop-band along the crystallographic direction (111) (normal to the growth direction, fig. 3.2), which is also called pseudo-photonic band gap (p-PBG).

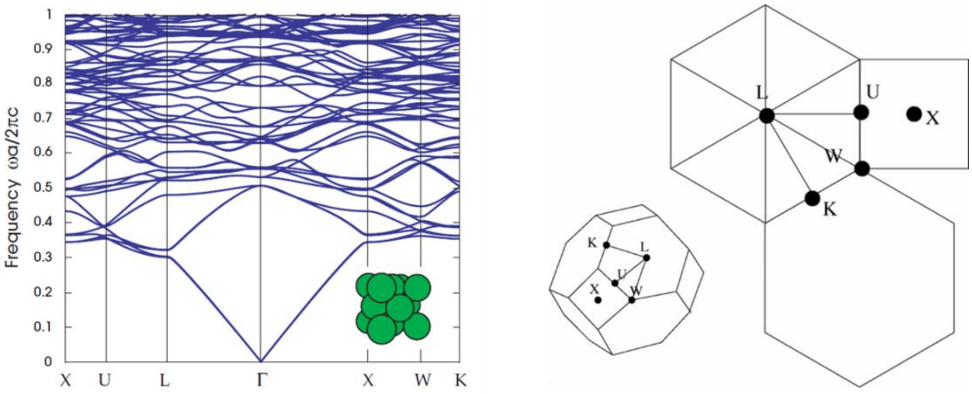

Figure 4.2 Right: photonic band structure of an opal made with dielectric spheres (ε=13). The stop-band is present along certain crystallographic directions (e.g. the Γ-L direction) but not for every direction, thus it is not a complete photonic band-gap. Inset: FCC lattice structure; taken from ref. [3].Left: symmetry point in the Brillouin zone for a FCC lattice; taken from ref. [137].

In addition to the p-PBG, synthetic opals present also other several modes at higher energies. In particular, the band structure of opals in the region of high frequencies is more complicated to describe than that in the spectral region in which there is the stop-band. To distinguish the different effects caused by the band structure you the Bragg-Snell law is not sufficient, and it has been resolved using analytical models starting from Maxwell’s equation. As an example I report the photonic band structure and the relative density of states (DOS).

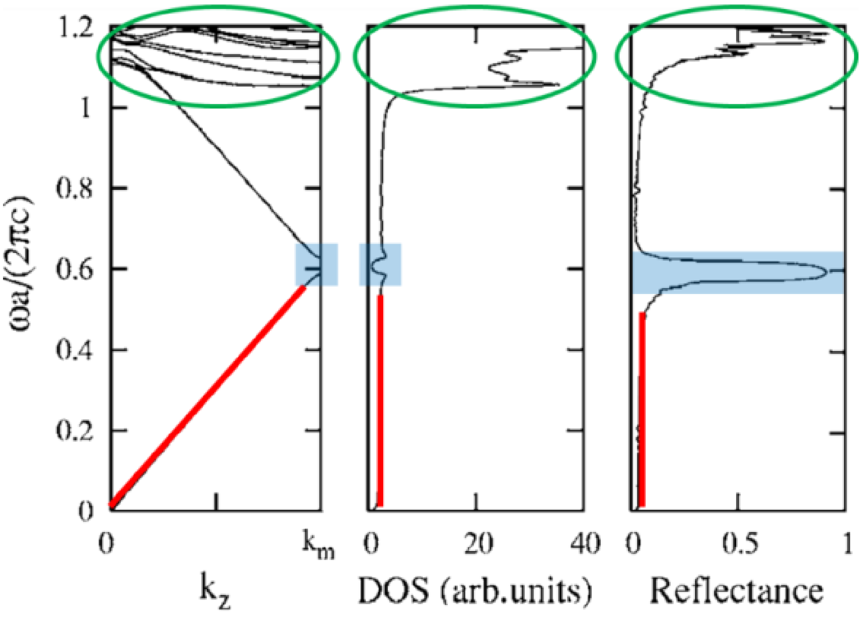

Figure 4.3 Photonic band structures and corresponding DOS and reflectance spectrum at normal incidence. Adapted from ref. [137].

In figure 4.3 three distinct photonic regions are shown: in red band structure exhibits a linear regime, corresponding to a constant DOS; the band gap is highlighted in blue and in correspondence the DOS is suppressed and, finally, the band structure, that is circled in green, has a non-linear dispersion and presents critical points, also known as van Hove singularities (in analogy to the critical points in the joint density of states commonly used for describing the optical properties of semiconductors [154]) and this correspond to a divergent DOS. The photonic band-gap and the singularities are caused by different physical phenomena. Respectively, the PBG is due to backward diffraction by the (111) planes, the van Hove singularity are caused by diffraction along directions different from the incident one, by families of planes other than the (111). This difference has a strong impact on the dispersion properties of the two structures as shown in figure 4.4.

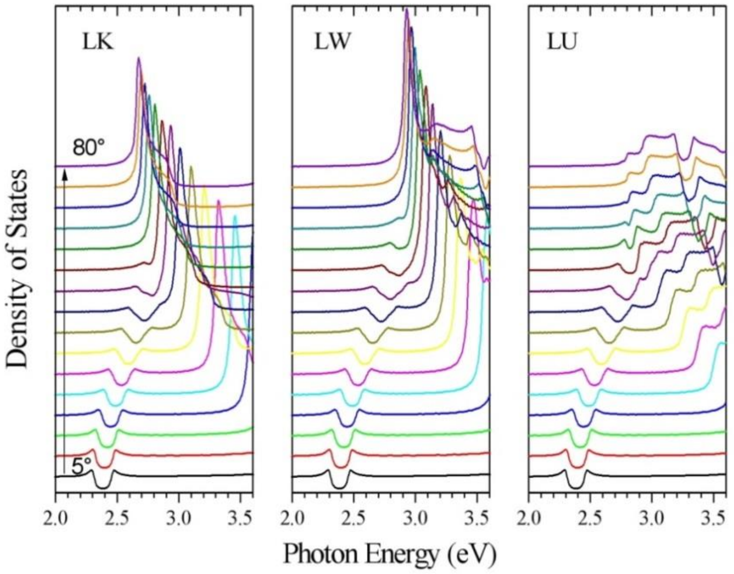

Figure 4. 4 Density of states at different angles and for different orientations. Taken from ref. [137].

In figure 4.4 it can also be observed observe that the stop-band and the van Hove singularities have opposite trends as function of the angle of incidence (θ). In fact, by increasing θ of the gap shifts to higher energies whereas the singularities move at lower energies. Furthermore, the dispersion of the van Hove singularities depends on the orientation of opal.

4.2 Polyrotaxanes

Conjugated polyrotaxanes [143, 155, 156] are a special class of conjugated polymeric semiconductors that are threaded through cyclodextrin macrocycles which act like rings around the conjugated backbone (figure 4.5) .These rings behave as “spacer” between the chains and thus provide control over the interchain interactions and enabling us to investigate the photophysics of conjugated semiconductors [157, 158].

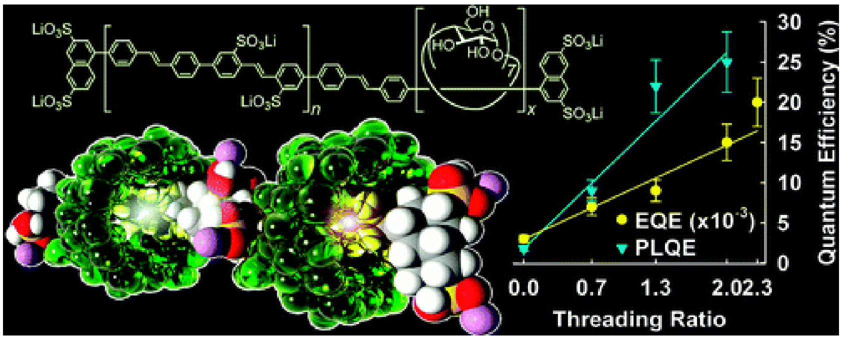

Figure 4.5 Chemical structures of the cyclodextrin-threaded conjugated polyrotaxanes with poly(4,4’-diphenylene-vinylene) (PDV.Li) core with naphthalene stoppers (average number of repeat units n = 10) and its optical properties (photoluminescence quantum efficiency, PLQE, and OLES external quantum efficiency, EQE) as function of the threading ratio. Reproduced from ref. [157].

In particular, cyclodextrin insulation suppresses intermolecular interactions, showing photoluminescence decay dynamics which is independent of concentration [156, 159].

Interestingly, although encapsulation preserves the intrinsic spectroscopic properties of the isolated chains, it does not suppress the charge transport in solid films, thus yielding enhanced and blue-shifted electroluminescence with respect to unthreaded conjugated polymers.

For all these reasons, during the last 15 years they have been successfully used in white-light-emitting diodes [6-8] and optically pumped laser [9, 10].

Another interesting property of polyrotaxanes is their water solubility. In fact, cyclodextrin threading is obtained via hydrophobic binding, which requires processability in polar solvents. For this reason, polyrotaxanes backbones are functionalized with of polar groups and are thus interesting for a variety of applications, spanning from biosensing to incorporation into plastic photonic structures without the need of covalently binding the polymers.

4.3 Experimental details

I prepared opals with polystyrene microspheres of different size. The preparation of the artificial opals consist in a self-assembly of commercial polystyrene microspheres (Duke Scientific, 10% in volume, diameters of 200, 220, 370 and 430 nm, standard deviation < 5%; refractive index, $n_{PS} = 1.59$), exploiting the vertical deposition method onto glass substrates.

The starting suspensions are further diluted to 0.2% v/v in diluted water in order to grow opals of the desired thickness. Typically, an opal thickness of 3-4 μm offers the best compromise between reflection and transmission. The opals have been prepared onto commercial soda lime slides previously cleaned with the RCA-1 procedure to obtain a more hydrophilic surface [160].

Once cleaned, the slides are immersed perpendicularly in the suspension of microspheres and lifted at a constant speed ($7\text{x}10^{-5}$ mm/s) at 28 °C. The process takes place inside an incubator placed onto an optical table to avoid any possible vibration that would cause defects and stacking faults inside the photonic structures. I used a home-built dip-coater with a motorized translation stage (Thorlabs). The opal film is created at the interface between the water meniscus and the glass substrate by the Van der Waals force during water evaporation (figure 4.6(a)). The polystyrene microspheres self-assemble into a face-centered cubic lattice with the crystallographic [111] direction oriented perpendicular to the substrate. Figure 4.6(b) shows the dip-coater inside the incubator with multiple slides securely attached to an extension that permits to simultaneously create opals of different sized microspheres.

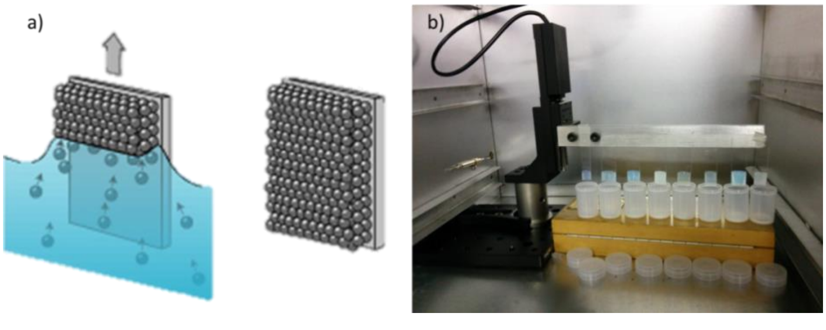

Figure 4.6 (a) Scheme of the vertical deposition technique used to prepare the opals and (b) the experimental set-up.

The active material I used was a semiconducting polymer, PDV.Li, a polyelectrolytic derivative of polypara-phenylene where sulfonated sidegroups are balanced by Li+ ions, threaded with β -cyclodextrin macrocycles (PDV.Li⊂ β –CD), known as polyrotaxanes (figure 4.5) [156]. I used of PDV.Li⊂β–CD with threading ratio 2 (i.e. number of cyclodextrins per monomeric repetition unit). The conjugated polymers were synthesised at the “Chemistry Research Laboratory, Department of Chemistry, University of Oxford” by Dr. Shane O. McDonnel and Prof. Harry L. Anderson.

I obtained effective incorporation of the polyrotaxane inside the opals via a co-growth method during the vertical deposition of the PhC. A PDV.Li⊂β–CD concentration of $8x10^{-3}$ mg/ml yielded homogeneously infiltrated opals without hindering the formation of the photonic crystals (which could affect the intrinsic PhC optical properties) while preserving strong PL properties of the system. Furthermore, partial infiltration of voids preserves a reasonable dielectric contrast within the structure, as inferred from lack of spectral shifts and narrowing (broadening) of the stop-band. Scanning electron microscope (SEM) micrographs of the co-grown PhCs reported in figure 4.7 show no presence of lattice distortion induced by the incorporation of polyrotaxanes, nor an excess polymer layer on the opal surface for co-grown PhCs with 8×10^{-3} mg/ml PDV.Li⊂β-CD solution and, more importantly, that the interstices between nanospheres are empty, thereby preserving a desirable higher dielectric contrast within the structure than otherwise possible in case of substantial filling of the interstices. The inset of figure 4.7(a) shows a photography of the opal with a laser diode (λ = 405 nm) incident on the crystal surface. I can observe the hexagonal diffraction pattern of the infiltrated opal, thus confirming the high internal order of the FCC crystal [161, 162].

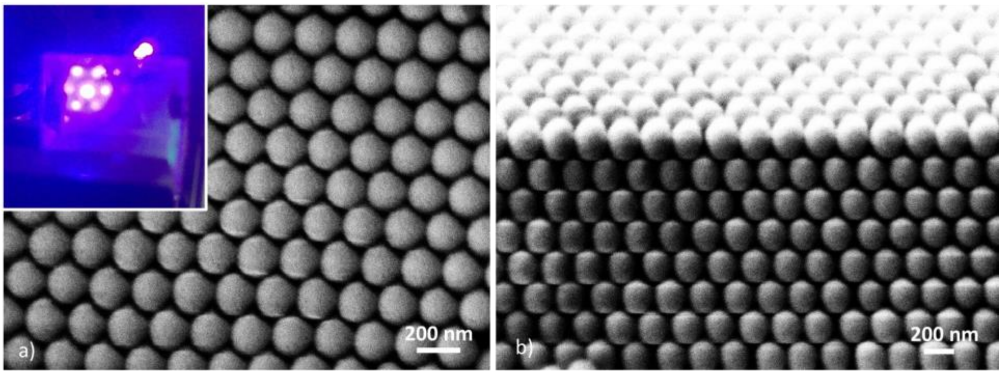

Figure 4.7 SEM micrographs of an opal film incorporating PDV.Li$\subset\beta$-CD: (a) cryo-cleaved wall surface showing the internal structure of the opal, (b) film cross-section. Strong contrast between the sphere and the interstices is observed, confirming that the latter are not filled up by the conjugated polyelectrolytes (the density of the conjugated moiety and of the spheres being comparable). Inset: Photography of the diffraction pattern from the opals. Images were collected using the SEM mode of a dual beam Carl Zeiss XB1540 “Cross-Beam” focussed-ion-beam microscope and the cross section was obtained via cryo-cleaving an opal film. Adapted from ref. [110].

Normal reflectance and angle resolved transmittance measurements have been carried out using an Ocean Optics S2000 spectrometer in combination with a fibre-coupled Ocean Optics HL-2000 tungsten halogen source. Steady-state PL spectra at different incidence angle of the exciting beam have been carried out using a pulsed laser diode (λ_{ex} = 371 nm, pulse width ~60 ps) and an Andor Shamrock 163i spectrometer coupled with an Andor Newton CCD camera cooled at -50 °C. Samples have been mounted on a rotating stage (M-060.DG, Physik Instrumente, resolution ~0.0001°).

4.4 Bare opals investigation

The obtained synthetic opals have an area of 2 cm^2 and to check the crystals homogeneity normal incidence reflectance spectra have been collected in different spots of the samples. Figure 4.8 shows the reflection spectra for the opals made with spheres having a diameter of 200 nm (a), 220 nm (b) 370 nm (c) and 430 (d).

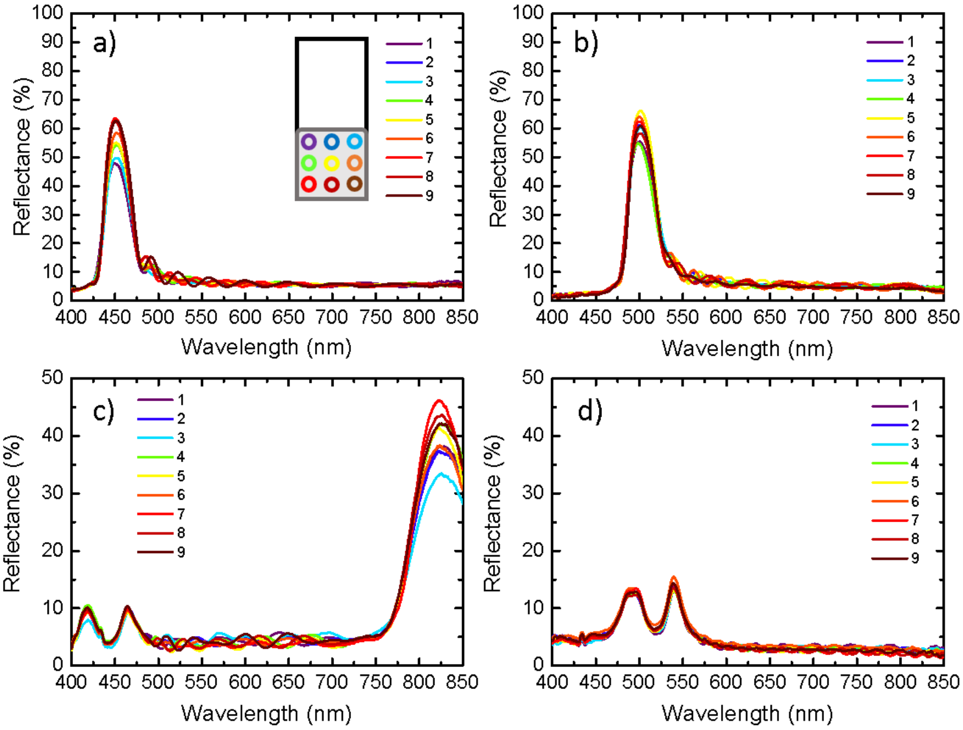

Figure 4.8 Reflectance spectra collected from opal made with microspheres with a diameter of (a) 200 nm, (b) 220 nm, (c) 370 nm and (d) 430 nm. Inset: scheme of the mapping.

In all spectra I observed the presence of three characteristic structures: the Bragg reflectance peak (except for the opal made with larger spheres, where this peak is in the “deep” NIR and thus not visible using the spectrometer available in our laboratory) at 450 nm, 500 nm and 825 nm for the sample made with spheres of 200 nm, 220 nm and 370 mn diameter, respectively; the interference fringes due to the Fabry-Perot effect from the front and back faces of the crystal and the van Hove-like modes 420 nm and 470 nm for the opal made with 370 nm spheres and 480 nm and 540 nm for the opal made with 430 nm sphere. The latter are situated at shorter wavelengths than the Bragg peak and are known to depend strongly on the internal FCC order [109, 137] and on the microsphere quality [109]. According to the Bragg-Snell’s law, the Bragg peak shifts to lower energies while increasing the diameter of the microspheres. Interestingly, the spectral position and the spectral shape of the Bragg peak and van Hove singularities are unchanged in each point of the samples, thus suggesting a good uniformity in the PhCs.

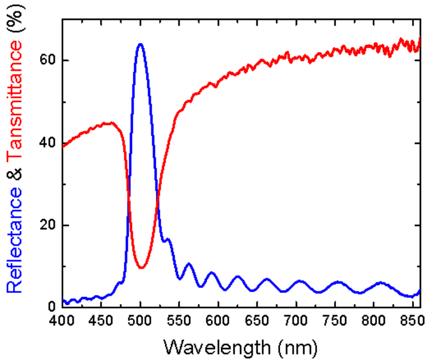

Figure 4.9 Reflectance (blue line) and transmittance (red line) spectra of an opal prepared with microspheres diameter = 220 nm.

Figure 4.9 shows the reflectance and transmittance spectra of the opal prepared with microsphere having a diameter of 220 nm. The photonic band-gap can correspond to a reflectance peak and a transmission dip. I calculated the total thickness of the opals using the interference fringes in the reflectance spectra using Eq. 18 and the n_{eff} obtained from Eq. 19. The values calculated from the opals shown in figure 4.8 are reported in table 4.1

Microspheres diameter (nm)	Thickness (µm)
200	2.9±0.2
220	3.1±0.1
370	2.6±0.1
430	4.2±0.2

Table 4.1 Thickness of the opals made with different micorspheres diameters.

As seen from table, it is possible to achieve a good control on the total thickness of the sample.

Angle resolved transmittance measurements permits to analyze the dispersion (i.e. the dependence of the photons on the wave-vector of the light) of the photonic gap and the high-energy modes. In fact, as observed in the band structure of opals (figure 4.4) there is a strong dependence on the wave vector k which is correlated to the angle of incidence of light θ. In particular, I can sample along the LU crystallographic direction.

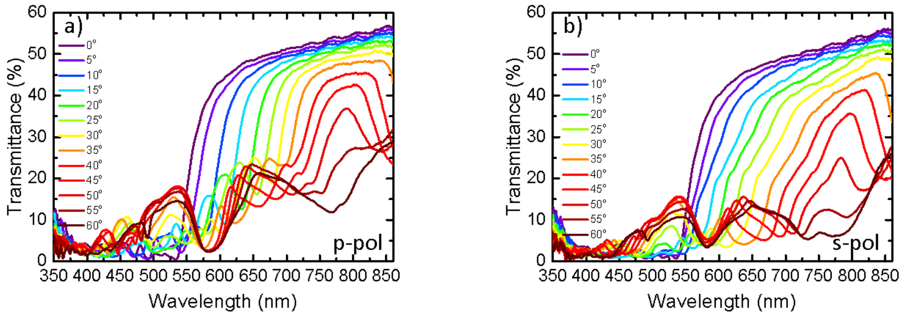

Figure 4.10 Angle-resolved transmittance spectra for the opal made with microspheres diameter 430 nm for (a) p- and (b) s-polarised light.

Figure 4.10 shows the transmission spectra collected with p- (a) and s- (b) polarised light of an opal made with spheres with a diameter of 430 nm.

As previously said, the Bragg peak cannot be resolved at normal incidence, similarly to the reflectance spectra shown before in figure 4.8(d). Interestingly, the stopband starts appearing at 40°, as predicted by the Bragg-Snell's law, the stopband blue-shifts at higher incidence angle. The minimum in the transmission spectrum increases for p-polarized light as the incident angle approaches Brewster's angle. In addition to the photonic stop-band I can observe the high-energy modes. Such structures have opposite dispersion compared to the photonic gap and therefore undergo to a red-shit while increasing the collection angle. To show better the dispersion of the photonic bands, the same data are reported on colored contour-plot in figure 4.11.

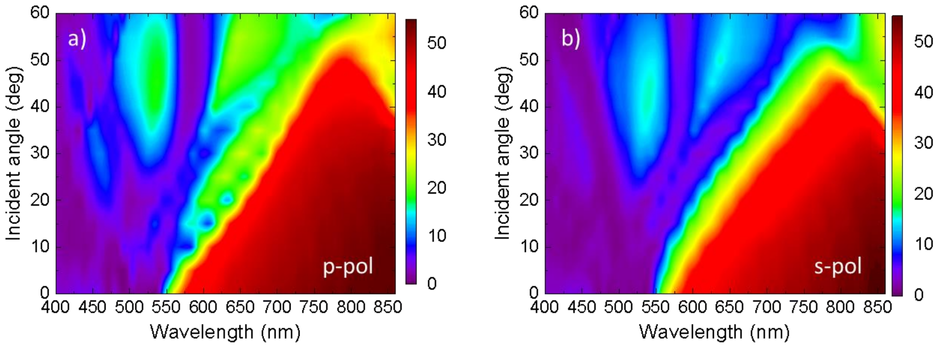

Figure 4.11 Colored contour-plot of the transmittance spectra for the opal made with microspheres diameter 430 nm for (a) p- and (b) s-polarised light. Transmittance percentage is shown in color scale.

Although limited to higher angle, I can observe that the dispersion of the photonic gap that is the same for both polarizations, whereas the width of the stopband is rather different, in particular for polarization p the peak narrows increasing the angle of incidence, while for the s polarization it increases at larger angles of incidence. Furthermore, I can clearly see all thehigh-energy modes. These structures have opposite dispersion to the Bragg peak and at angles above 45 ° these modes overlap the Bragg peak. Interestingly, they strongly depend on the polarization.

From these measurements it is possible to obtain the effective refractive index of the opals by fitting with the Bragg-Snell's law the spectral position of the stop-band as a function of θ, assuming that the lattice is the ideal FCC for which $D = \sqrt{2/3}\,a$, where D is the inerplanar distance and a the microspheres diameter. Figure 4.12 shows the unpolarised transmittance spectra for the opals: (a) 200 nm, (b) 220 nm, and (c) 370 nm.

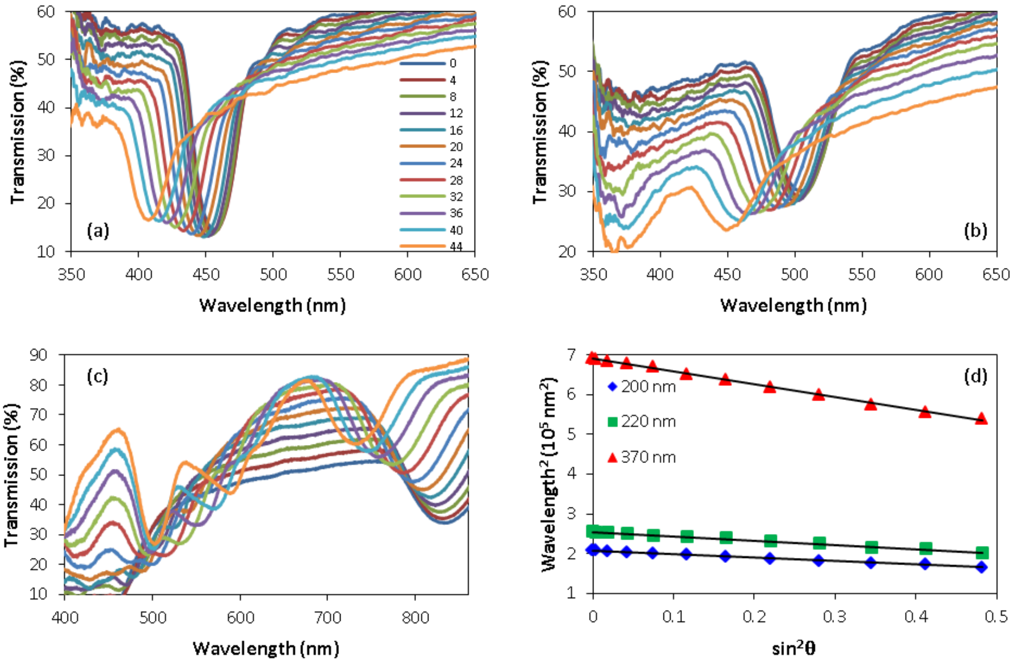

Figure 4.12 Transmittance spectra of the opals as a function of incidence angle for (a) 200 nm, (b) 220 nm and (c) 370 nm microspheres diameter. The Bragg-Snell law analysis of the spectra appears in (d) where the lines are linear regressions. Taken from ref. [146].

Fig. 4.12(d) shows a linearized form of Bragg-Snell's law fitting of the stop-band wavelength as function of the angle of incidence of light. By setting in the equation the nominal diameter of the microsphere provided by the manufacturer, I derive an effective refractive index of 1.40 for each opal in agreement with the Lorentz-Lorenz relation. This result confirms that the opal is well ordered in a face-centered cubic lattice without, or with very few, stacking faults inside.

4.5 Infiltrated opals investigation

Figure 4.13 shows reflectance spectra of a bare opal made with polystyrene microspheres with a diameter of 200 nm before and for the infiltrated opal. The presence the polymer inside the opal has no effects on the optical properties of the photonic crystal, in fact no significant changes in the spectral position and in the shape of the reflectance peak of the PhCs have been observed.

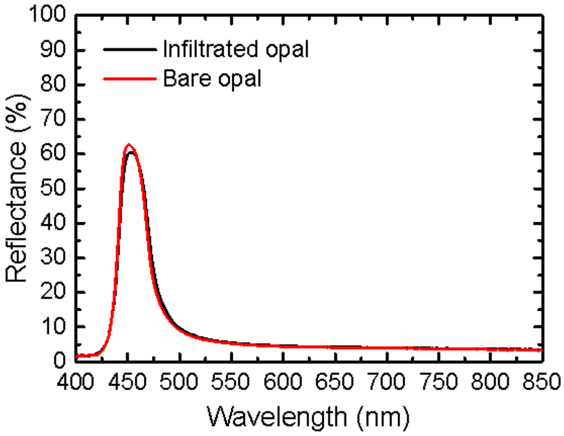

Figure 4.13 Reflectance spectra of the bare opal made with microsphere diameter 200 nm (red) and infiltrated (black) with the polyrotaxanes. There is no difference between the spectral positions of the reflectance peaks.

Figure 4.14 shows the reflectance peaks of the opals made with microspheres with different diameter and also the PL of a polyrotaxanes spin-coated thin film and the PL of the same polymer infiltrated into the opal annealed at 80 °C for 10 minutes in air. The thermal annealing was sufficient to destroy the internal order of the structure and, in turn any photonic effects, without harming the polymer due to the high thermal stability of this class of supramolecular systems.

I observe that there is about 50 nm blue-shift in the PL for polymer infiltrated into the melted opals compared to the spin-coated thin film. I attribute this effect to the electrostatic interactions of the Li^+ cations with the negatively charged surface of the polystyrene microspheres. This effect would lead to a modification the electronic properties of the semiconducting chains.

Furthermore, due to the preparation method, that induces strong capillary forces [163], and to the internal geometry of the crystal, the polymers undergo to structural constraints, leading to a modification of the PL dynamics of the polyrotaxane compared to that observed in a neat-polymer film or solution [157].

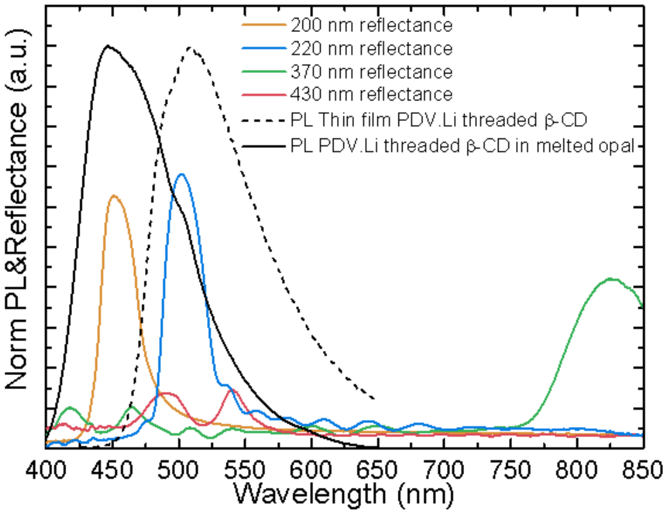

Figure 4.14 Normalized reflectance spectra (coloured lines) of the bare opals and normalized PL emission (black solid line) of polyrotaxanes inside a thermally annealed opal and of a spin-coated thin film (black dashed line). The annealing was necessary to keep the material chemical properties but avoiding the photonic contribution.

The main results discussed here concern spheres with a diameter *a* = 200 nm since these ensure an optimal spectral overlap of the polyrotaxane PL spectrum and of the opal stop-band.

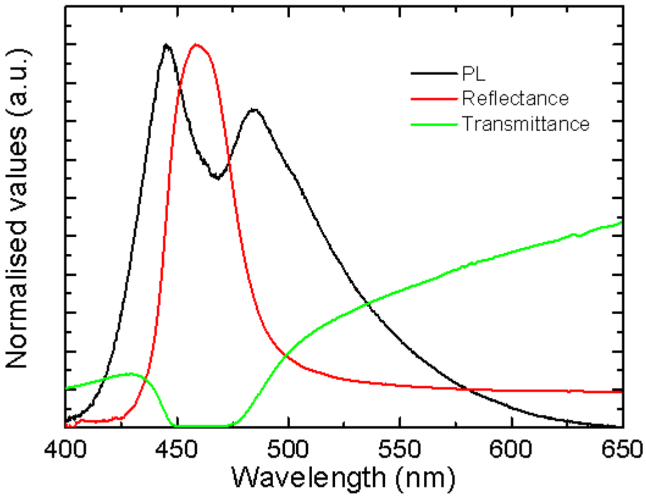

Figure 4.15 PL (black), reflectance (red) and transmittance (green) spectra col lected at normal incidence for spray-coated opals made with beads having diameter 200 nm (a) and 430 nm (b).

Figure 4.15 shows reflectance and transmittance spectra of the opal made with polystyrene microspheres with a diameter of 200 nm. As expected, the reflectance peak at ~450 nm corresponds to a minimum in the transmittance spectrum. Remarkably, the PL emission is strongly modified by the opals. Specifically, in correspondence of the photonic stop-band there is partial suppression of the PL, whereas there is an enhancement at the high-energy edge.

The angle-resolved PL spectra for infiltrated opal are reported in figure 4.16. In particular, the spectra as function of the illumination angle (a) and the PL ratio between the emission from the polyrotaxanes infiltrated into the as prepared opal and the melted one (b) are shown.

The PL of the polyrotaxanes is strongly modified by the photonic crystal: in particular, the emission is partially suppressed in correspondence of the stop-and. In addition, there is an enhancement of the PL intensity at the high-energy edge of the stop-band. Both enhancement and suppression have the same dispersion as the stop-band, thus suggesting that both effects are connected to a directional redistribution of the photonic density of states [7, 13].

The enhancement/suppression effects are better appreciated in the ratio between the two PL spectra (figure 4.16(b)). Note that within the PBG the ratio is lower than 1 (indicated in the figure by the black line), instead the ratio is above 1 for the short-wavelength edge of the PBG [7, 13, 15, 16].

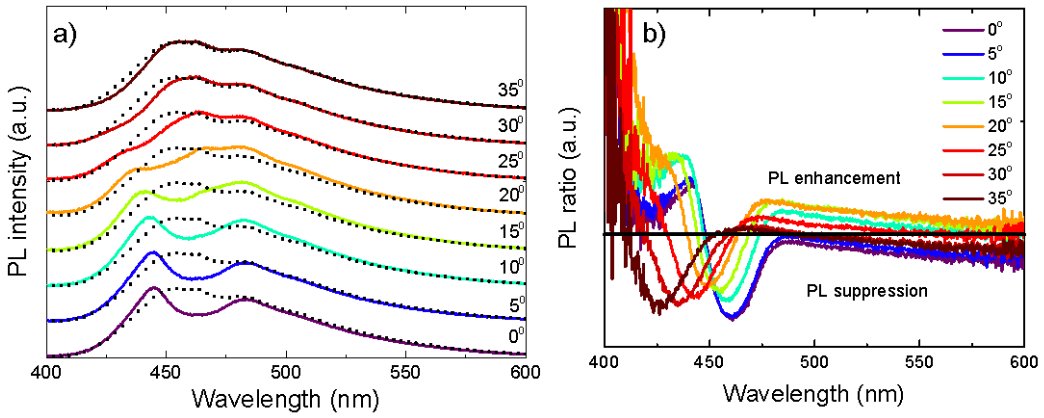

Figure 4.16 (a) Angle resolved PL emission for infiltrated opals made with microspheres diameter 200 nm (a). The enhancement and suppression effects depend on the incident angle. This effect can be better appreciated in (b) where I plot the PL ratio between the thin film and the photonic structure at various angles.

4.6 Conclusion

In conclusion, I have been able to observe different photonic effect in all-plastic water-solution processable photonic crystals functionalized with a supramolecular conjugated polymer. First I presented a simple bottom-up method tor the preparation of high quality synthetic opals. I examined the opal polarized reflection and transmission spectra. These measurements permit to evaluate the effective refractive index of crystals made with spheres with various diameters and I found good agreement between models and experimental findings.

Furthermore, I have been able to modulate the emission of the polyrotaxanes without changing its chemical structure. In particular, I observed a wavelength dependent enhancement/suppression of the emission spectra of β-CD-threaded $PDV_{10}Li$. These effects are related to the modification of the photonic density of states inside the photonic stop-band and at its high-energy edge.

Chapter 5

Nanostructured titania for efficient perovskite solar cells

In this chapter I exploit the polystyrene micrspheres used in the previous Chapter 4 for the preparation of novel titania scaffolds that will be implemented into perovskite photovoltaic devices. Specifically, the micropsheres have been used for the formation of a colloidal template for the subsequent growth of the ETL layer.

Titanium dioxide (titania, or TiO_2) is a semiconducting material that, thanks to its wide band-gap (3.7 eV) and relatively high oxidation potential of the holes generated upon UV-light irradiation, can be employed in photovoltaic devices [164], and photocatalysis [165], respectively. In particular, in recent years TiO_2 has been incorporated effectively as scaffold layer in organo-halide perovskite solar cells, in which its porosity and meso/nanostructural arrangement play an important role in the charge transport processes occurring in such promising class of photovoltaic devices. It is thus essential to investigate the experimental parameters controlling its structural and optical features.

In particular, here I describe the preparation and characterisation of such porous photonic titania scaffolds via a simple and scalable bottom-up approach. I also integrated such scaffolds in organo-lead-halide perovskite solar cells. The photovoltaic devices presented herein show higher efficiency compared to standard ones prepared onto mesoporous or compact titania layers thanks to significantly improved light trapping. In addition, the charge-transport performances are also improved according to an optimised perovskite film morphology. As a result, I obtained an average power conversion efficiency 50% higher than reference cells prepared onto mesoporous titania scaffold for the ones prepared with the optimised TiO_2 nanostructure, thus making such scaffold layers good candidates for efficient perovskite solar cells.

5.1 Nanostructures for optoelectronic

Ordered photonic nanostructured surfaces are gathering increasing interest since they can be used to investigate in innovative technological applications in optoelectronics and photonics. In particular, the incorporation of photonic nanostructures into optoelectronic devices has seen to beneficial for the operation of such systems, as they can boost and/or modify the interaction between light and active material. In this context, photonic structures can be used as optical feedback structures in lasers [166, 167], as diffraction grating to enhance the angular emission of OLEDs [168, 169] and light confinement in solar cells [170-173].

Among various materials that can be employed as active layers in these applications, organic–inorganic lead halide perovskite materials have attracted increasing attention thanks to their outstanding optoelectronic properties, in particular in photovoltaic devices [98, 99, 174]. Perovskite-based solar cells have been reported so far in two different configurations: planar heterojunction [175] and the mesoscopic structure based on oxide film [176].

The planar heterojunction configuration permits more versatility in terms of device architecture, as it can be used for both direct and inverted cells (see chapter 2 section 2.3.1), although the mesoscopic configuration derives from the dye-sensitised cells technology, and has benefitted from years of technological refinements and optimisations. In addition, mesoscopic scaffolds can be designed for maximizing optical absorption using nanostructured photonic materials.

Although various oxides have been investigated, TiO_2 remains the most extensively used scaffold material [177]. Standard mesoporous titania scaffolds consist of nanocrystalline films with a thickness of few hundreds of nanometres [174], usually obtained via sintering of TiO_2 nanocrystals paste (usually around 20 nm).

Among various techniques, colloidal monolayer lithography is an efficient and low-cost technique for the fabrication of large area, highly ordered, structured scaffolds. Monolayers of polymeric micro and nanospheres are prepared via self-assembly [178] e.g. drop-casting [179], spin-coating [173, 180], Langmuir-Blodgett technique [181] or air-water interface transfer of the monolayer onto a substrate [113].

Herein, I exploit an ordered, hexagonally packed, titania microspheres monolayer obtained via a replica of a polystyrene microspheres monolayer, obtained via a facile air-water interface method. I find that nanostructured perovskite solar cells prepared onto these photonic structures show higher efficiency, which I attribute to both improved perovskites crystallization and to an enhanced light-harvesting induced by the nanostructures.

5.2 Experimental details

Commercial polystyrene (PS) monodisperse microspheres (10% in volume, diameter a = 220, 370 and 430 nm; refractive index, $n_{PS} = 1.59$; standard deviation < 5%) water suspensions (Thermo Scientific) were used for the preparation of monolayers. These were prepared via the self-assembling method at air-water interface. Microspheres suspensions were properly diluted in ethanol with a 1:2 ratio and then dropped onto the water surface. The resulting self-assembled ordered two dimensional hexagonal-closed packed structures were transferred onto the FTO/c-TiO_2 substrates dipped into the reservoir. The good quality of the PS microspheres monolayers and the effectiveness of the transfer process are confirmed by the atomic force microscopy (AFM) characterisation (see figure 5.2(d)). To obtain the titania nanostructures, the microspheres monolayers were infiltrated with the titania precursor solution. This was prepared by mixing 100 mL of titanium(IV) isopropoxide (Sigma Aldrich, 97%) with 10.0 mL of ethanol and 2 mL HCl (2M). One droplet of the solution was carefully deposited onto the samples that were then let dried at room temperature for 12 h. Eventually, the monolayers were calcined via a multiple steps annealing in a furnace (fast heating from room temperature to 150 °C, approx. 30°C /min, then to 300°C with a rate of 5°C/min and left for 2 hours, finally increased with again a rate of 5°C/min to 500°C and left for 2 hours) to obtain the hexagonal-closed packed titania microspheres layer.

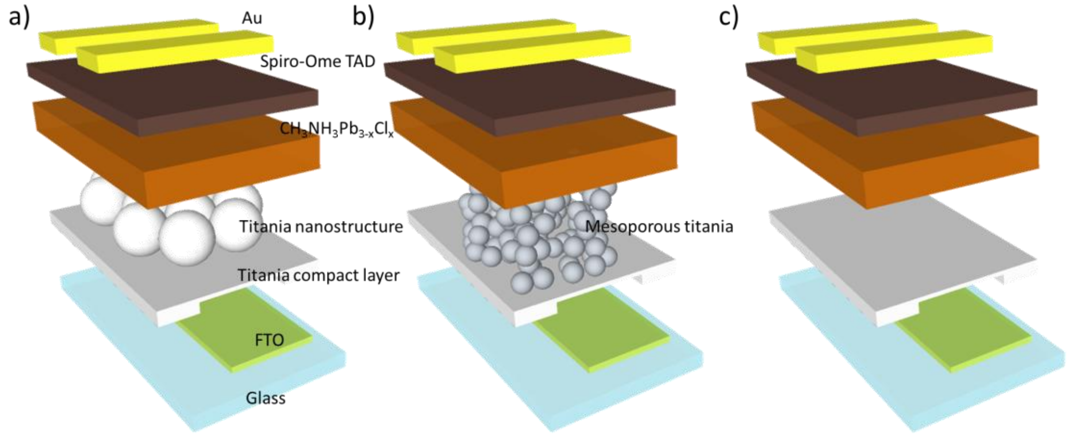

Figure 5.1 (a) Scheme of the device prepared with the ordered nanostructure, (b) with the "standard" titania mesoporous scaffold, and (c) with the perovskite coated on top of the compact titania layer.

Figure 5.1 shows the three device architectures for organo-halide perovskite solar cells tested in this work. To create the desired electrodes pattern, FTO/glass substrates (Sigma Aldrich, 13 Ω/□, 15 mm x 20 mm) were patterned with zinc powder and 2 M HCl diluted in deionized water. The obtained substrates were first cleaned with ultrasonic bath in acetone and isopropanol (12 min each step), then treated with an oxygen plasma for 10 min to remove any remaining organic residues. The compact TiO_2 film (c-TiO_2) was deposited by spin coating at 2000 rpm for 60 s and sintered on a hot plate at 500 °C for 30 min in ambient condition. For the reference devices, a TiO_2 paste (nanocrystals average size ~ 20 nm, Dyesol 18NR-T) was diluted to 1:5 with ethanol and spin coated on substrate at 1000 rpm for 60 s (thickness ~300 nm) and sintered at 500°C for 30 min to obtain the mesoporous scaffold layer.

After the deposition of the titania nanostructured or mesoporous films, the perovskite layer was obtained by spin coating the $CH_3NH_3PbI_{3-x}Cl_x$ solution (Ossila Ltd.) in nitrogen atmosphere at 2500rpm for 60 s and heating at 90 °C for 90 min. The hole-transporting material (HTM) was deposited by spin coating a solution of 2,10,7,70-tetrakis-(N,N-dip-methoxyphenylamine)9,92-spirobifluorene (Spiro-OmeTAD) at 2000 rpm for 60 s in nitrogen atmosphere and left 4 h in air in a closed dry box. The solution was prepared by adding 96.5 mg of Spiro-OmeTAD (Ossila Ltd.), 10 µL of 4-tertbutylpyridine (TBP, Aldrich) and 30 µL of a

170 mg/mL LiN(CF_3SO_2) 2M solution in 1-butanol to 1 mL of chlorobenzene. Finally, the samples were introduced into a high vacuum chamber to evaporate gold (Au) back contacts (thickness 100 nm). An evaporation mask defined devices area of both 0.15 cm^2 and 0.09 cm^2.

The thickness of the films was measured by a surface profilometer (Dektak^3). UV-Visible transmittance measurements were done with an Agilent 8453 spectrophotometer. Surface morphology has been investigated by using an atomic force microscopy (AFM, Dimension 3100). All AFM images were recorded using tapping mode in air. XPS spectra were recorded with a PHI 5000 VersaProbe II scanning XPS Microprobe (TM) using monochromatic Al-Kα radiation (hν = 1486.6 eV) from an X-ray source operating at 200 μm spot size, 50 W power and 15 kV acceleration voltage. A surface XPS survey was collected with the hemispherical analyser (128 channels) at the pass energy of 23.500 eV, energy step size of 0.200 eV; the photoelectron take off angle with respect to the surface was 45 °; for depth profiling timed sputtering was performed with an Ar+ ion gun, with a 3×3 mm raster spot, 3 kV, with 10 s time steps. XRD measurements were performed with a Rigaku SmartLab diffractometer (Rigaku, Tokyo, Japan) by using a Kα wavelength emitted by a Cu anode (0.154 nm) using grazing incidence configuration.

Device performance was evaluated under illumination by a Class A solar simulator (ABET Technologies) at AM1.5G and 100 mW/cm^2 connected with a source-meter (Keithley2420), calibrated with reference Silicon cell (RERASolutionsRR-1002).

5.3 Morphological and optical characterization

The fabrication method for patterning the oxide structures in showed in figure 5.2(a). I deposited the hexagonal closed-pack microspheres monolayers onto the FTO/compact TiO_2 (c-TiO_2) coated substrate via self-assembling method at air-water interface. In particular, I used PS microspheres with three different diameters, namely 220 nm, 370 nm and 430 nm, to fabricate structures with different sizes and thicknesses. (step 1) After the monolayers were dried, I then dropped the TiO_2 precursor solution (step 2). The resulting TiO_2/ PS composites were then calcined in air and the final structures consisted in a hexagonal-closed packed hollow titania microsphere monolayer (step 3).

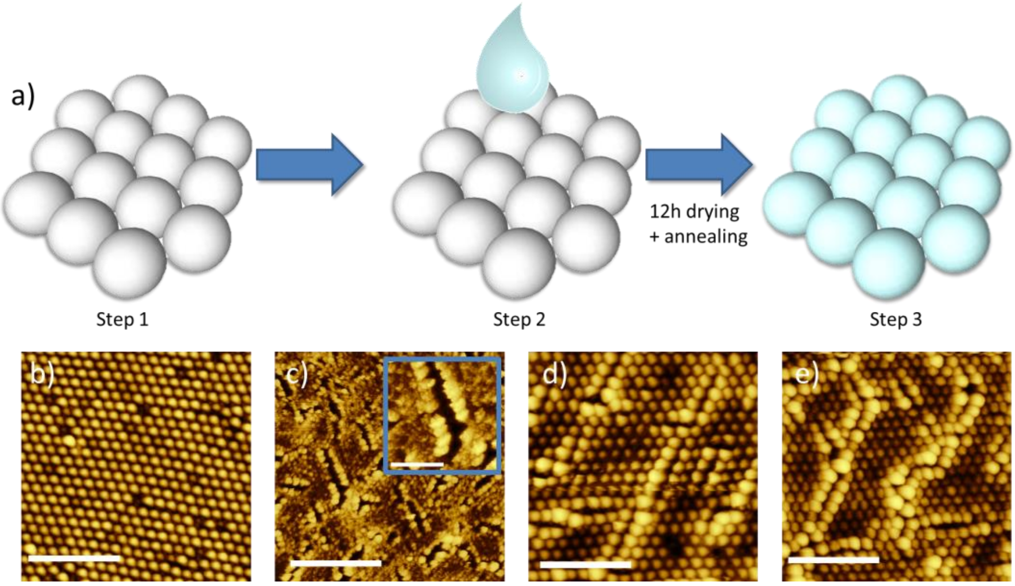

Figure 5.2 (a) Preparation steps for patterned titania photonic scaffolds: (1) PS microspheres monolayer is obtained via self-assembling and transferred onto the FTO/c-TiO_2, (2) drop-casting of the oxide precursor solution onto the PS microsferes template. Complete filling of the gaps of the monolayer is obtained leaving the samples drying overnight, (3) titania microspheres replica structure forms after a three-steps annealing described in the experimental section. AFM images (scalebars are 3 μm) show: (b) a typical highly-ordered monolayer of PS microspheres with a diameter of 370 nm, and the calcinated TiO_2 monolayers obtained from PS microspheres with various diameter, in particualr: (c) 220 nm (inse in blue box: a zoomed images on the layer, the scale bar is 1 μm), (d) 270 nm and (e) 430 nm.

Figure 5.2(b-e) shows the atomic force microscopy (AFM) images of the starting PS microspheres monolayer made with microspheres with diameter 370 nm (b), and of the titania samples (c – e). The titania microspheres hexagonal close-packed structure is well copied from the hexagonally packed colloidal PS templates in the titania samples, except for the sample made from the smallest spheres (220 nm), where the resulting structure is a random not-compact layer (inset in figure 5.2(c)). For the samples made from larger spheres, the obtained films are highly ordered, dense and continuous at large scale in spite of some cracks (figure 5.2(d) and (e)).

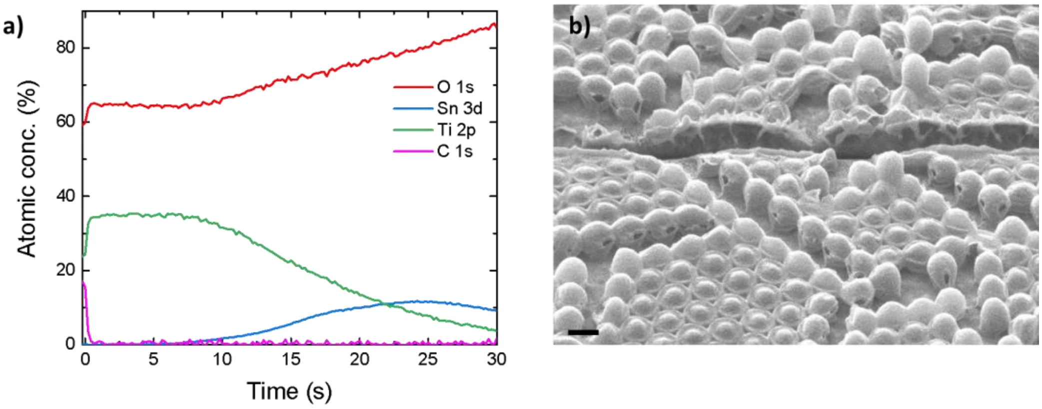

Figure 5.3 (a) Ar-milled XPS profile of the microspheres titania layer onto FTO/cTiO$_2$ substrates. Dr. Tiziana Fiore from University of Palermo for the measurement is thankfully acknowledged for these measurements. (b) FIB-milled SEM micrograph (scalebar is 400 nm) of the titania hollow spheres monolayer.

The X-ray photoelectron (XPS) depth profile (figure 5.3 (a)) confirmed the absence of residual polystyrene inside the titania nanostructures (within the ~1% limits of the techniques resolution). In fact, the carbon signal is attributed essentially to surface impurities, since the signal disappeared after 10 s sputtering. Furthermore, I observe a concomitant decrease of Ti concentration with an increase of the underlying Sn, which is present into the substrate. This confirms that the TiO$_2$ layer formation on the FTO substrate surface and that the annealing process removed the polystyrene leaving no more carbon inside the oxide microspheres. I carried out a focused ion beam (FIB) milling of the titania microspheres monolayer to check the internal structures of the spheres and the result is shown in figure 5.3(b). In the SEM images the beads appear a bit deflated due to the ion beam but, more interestingly, hollow inside.

As a control, I also prepared mesoporous titania scaffold onto the FTO/c-TiO$_2$ substrates ~400 nm thick. It is well-known that TiO$_2$ crystallizes into three main crystalline structures: anatase, rutile and brookite [182].

The X-ray diffraction (XRD) patterns of the TiO$_2$ nanostructures shows a pure anatase phase of both the titania oxide scaffold and compact layers (figure 5.4), with peak associated to the plane 101 at 25.37°, whereas the other peaks are related to the FTO. The XRD data were directly collected from the films on the FTO substrates.

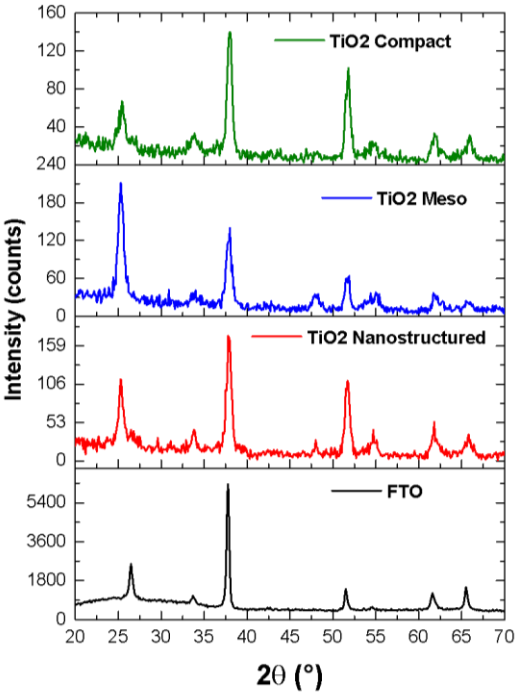

Figure 5.4 XRD spectra of the titania nanostructures and the titania mesoporous layer sintered onto FTO substrates and of the bare FTO. Anatase peaks of TiO_2: 2 theta 25.37°, fluorine-doped tin oxide (FTO) substrate peaks: 2 theta = 26.4°, 37.6°.These measurements were taken by G. M. Paterno' from our group.

In figure 5.5 I show a comparison of the transmission spectra of the control substrates (bare FTO, FTO/cTiO_2 and FTO/cTiO_2/mesoporous scaffold) and substrates with the nanopatterned TiO_2 structures made from the microsphere monolayers. I excluded from this and following characterization the titania scaffold obtained from the smallest microspheres (i.e. 220 nm) since form AFM images I did not observe any ordered structures. While the TiO_2 mesoporous scaffold film appears not to reduce the transmittance, compared to the bare compact layer sample, the nanopatterned structures show considerably different characteristic. In fact, I observe the presence of many dips at wavelength different to the one of the dip related to the cTIO_2 layer. The origin of this structure is related to the front light scattering induced by the monolayer [77].

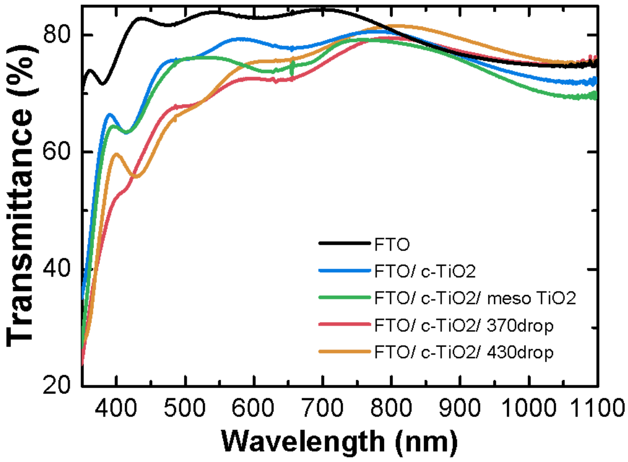

Figure 5.5 Transmittance spectra of the titania structure synthesized onto the FTO substrates.

Beyond the photonic ordered periodicity, these nanostructured monolayers are also highly porous structures. As a consequence of this, I expect a good filling behaviour within the pores, leading to a controllable perovskite crystals size, despite the tendency of the material to crystalize in large crystals [183].

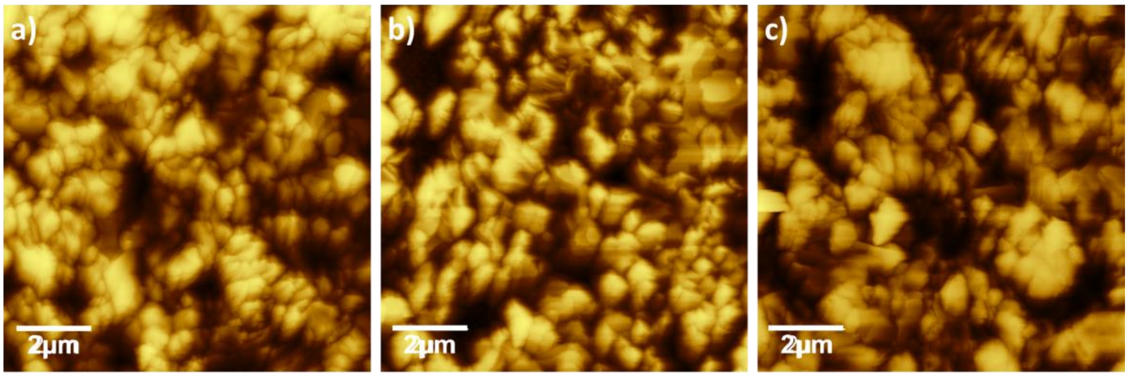

Figure 5.6 AFM (tapping mode) images of the perovskite layer synthesized onto the nanostructured titania starting from (a) spheres having a diameter of 370 nm, (b) the mesoporous titania layer and (c) on compact titania layer.

In figure 5.6 I show the morphology of the perovskite films grown on the titania microsphere monolayer and the flat titania film. While the perovskite film within titania nanostructures (figure 5.6(a)) appears to be more uniform and formed of small domains, the film on top of the compact TiO_2 (figure 5.6(c)) layer show larger and less compact perovskite crystalline domains. The crystallinity of the perovskite films prepared onto the different substrates is confirmed by the XRD spectra (figure 5.7). Although there are no changes on the peaks position, I note that the peaks are slightly broader for the perovskite grown on the microspheres, with a FWHM increasing from 0.227 for the film prepared onto flat titania layer to 0.339 for the film prepared onto the mesoporous scaffold, and 0.236 and 0.234 for the ones prepare onto the monolayer made with spheres with a diameter of 370 nm and 430 nm, respectively. This indicates that the crystal domain size is smaller, consistent with the AFM images and suggesting the confinement of the crystallization within the pores. Although the presence of smaller crystals has been demonstrated disadvantageous in terms of charge mobility, due to an increased number of grain boundaries [184], have uniform crystal domains with small grain sizes might improve the interfacial contact between the perovskite and the TiO_2

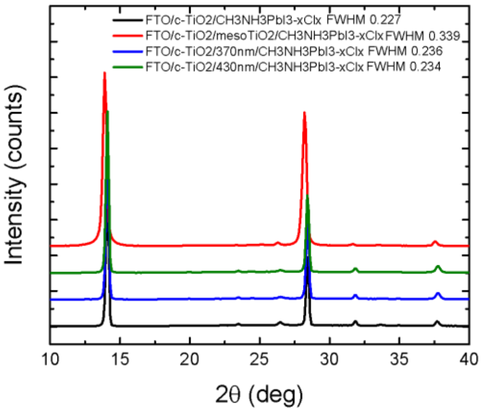

Figure 5.7 XRD spectra of the perovskite layer sintered onto FTO/cTiO2 (black line), FTO/cTiO2/mesoporous (red line), and FTO/cTiO2/nanostructure (blue line for the microspheres with 370 nm diameter, green line for the microspheres with 430 nm diameter) substrates. Broader peaks (full width half maximum, FWHM, inset) for the perovskite prepared onto the mesoporous and nanostructured films. These measurements were taken by G. M. Paterno' from our group.

The films prepared onto the mesoporous structure (figure 5.6(b)) appears to be formed by small crystals, similar to the films prepared onto the nanostructure, but the film looks less continuous and it appears to be not well infiltrated into the titania. In fact, in the AFM image I can see holes in the perovskite films and the titania underneath.

5.4 Photovoltaic devices

I fabricated solar cell devices by capping the microstructured perovskite layers with spiro-OmeTAD, an organic hole-conductor, and 100 nm of gold top electrode, as I show schematically in figure 1. I compared devices with and without the microstructured photonic titania scaffold at comparable perovskite concentrations and measured the device performance under simulated AM 1.5 100 mW cm^2 sunlight and in dark. The measurements have been carried out both in reverse (from open-circuit voltage, V_{oc}, to short circuit current density, J_{sc}) and direct (from J_{sc} to V_{oc}) bias conditions with a scan rate of 80 mV/s.

The J-V curves are shown in figure 5.8(a). I observe an increase in both open-circuit voltage (V_{oc}), that reaches a maximum value of 0.9 V for the device exploiting the scaffold prepared from the microspheres made with the spheres with diameter 370 nm, and short circuit current density (J_{sc}), with values exceeding 20mA/cm^2 for both devices employing the nanostructured TiO_2 as scaffold.

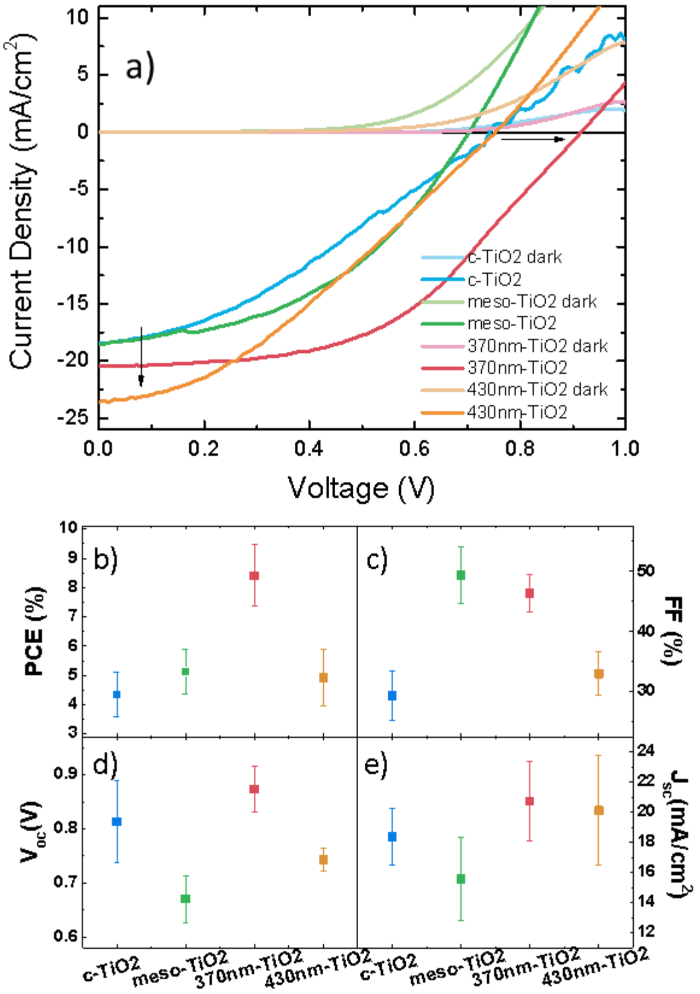

Figure 5.8 Electrical characterization and device performance analysis: (a) J−V curves of the devices both under illumination (darker curves) and in dark (lighter curves). The arrows highlight the enhanced Jsc and Voc obtained for the cells prepared with the nanostructured titania layer. (b-e) Box-plot of the devices performance: (b) power conversion efficiency (PCE), (c) Fill Factor (FF), (d) open circuit voltage (Voc), and (e) short-circuit current density (Jsc).

In figure 5.8 (b-e) I summarize all the solar cell performance parameters. Perovskite solar cells employing nanostructured TiO_2 microspheres monolayers exhibit power conversion efficiencies (PCEs), up to 9% for the 370nm diameter microspheres. This value doubles the efficiencies of the other devices analysed, although it is below state-of-the-art efficiencies [185] likely because the non-optimised perovskite growth process (moisture air level during the active layer casting, annealing temperature calibration and so on). The enhanced V_{oc} can be explained by the suppression of shunts between the hole-blocking layer (c-TiO_2) and the hole-transport layer (Spiro-OmeTAD) thanks to an improved isolation induced by the ordered microstructures which exhibit a controlled and optimized thickness. In particular, such an enhancement was observed only for the scaffold prepared from the smaller microspheres (i.e. 370 nm), whereas the larger microspheres did not show a remarkable improvement of the solar cells devices. I attribute this to a too thick oxide layer for the scaffold prepared with the larger spheres (i.e. 430 nm).

Interestingly, I note that the average short-circuit current densities (J_{SC}) are also higher than the devices prepared on both the just compact titania layer and also on the “standard” device prepared onto the nanostructured titania. I attribute this to two facts: first, as confirmed by the XRD pattern and the AFM, the perovskite domains might be smaller than the one obtained onto the compact titania and for this reason they are in full contact with the electron-transporting layer; second, the ordered layer is a better scattering medium compared to the other two, and this improve the light harvesting in the active layer.

Shunt resistance (R_{SH}) and series resistance (R_S) for devices have been obtained by fitting the J–V curves with a one-diode model (figure 5.9(a-d)) [186] and the mean values are reported in figure 5(e-f).

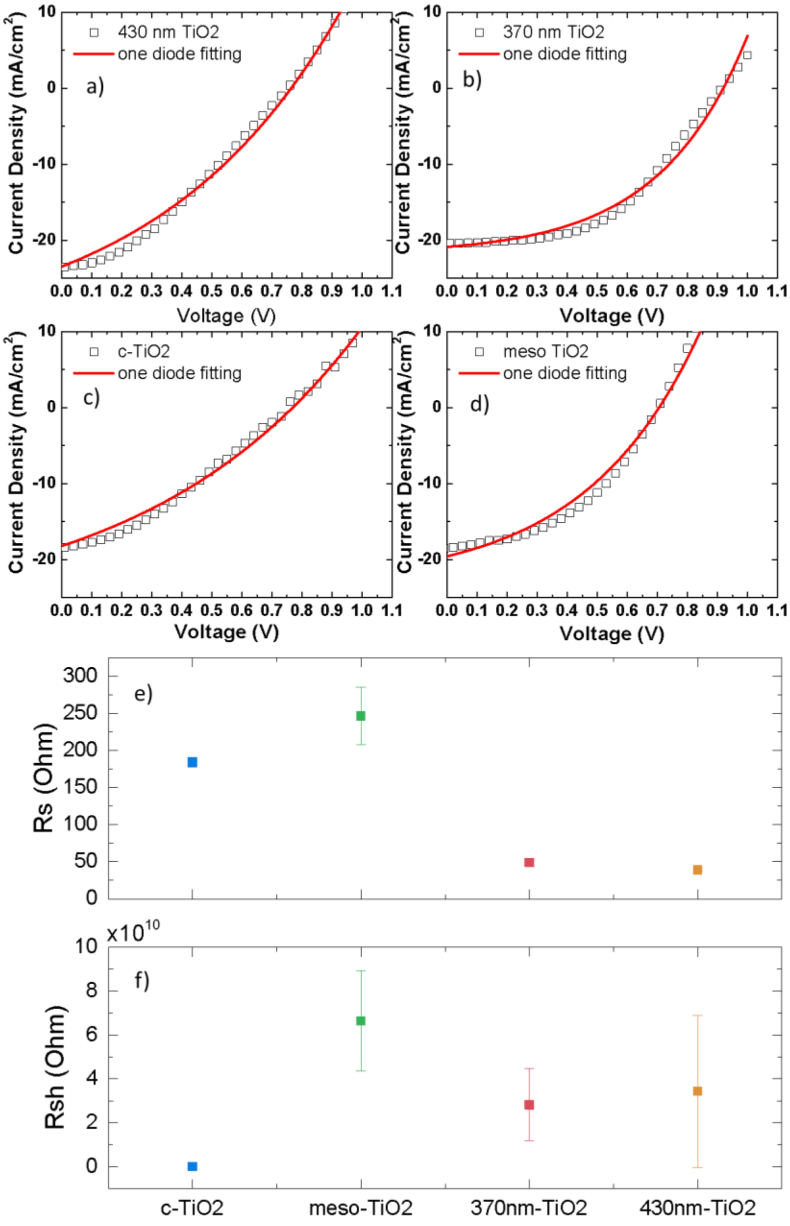

Figure 5.9 (a-d) One-diode model fitting (R^2>0.97) for each titania scaffolds. (e) Series resistance (f) and shunt resistance for devices obtained from the fitting of the current density – voltage curve.

The higher shunt resistances have been found for both the nanostructured and mesoporous titania confirming that the recombination paths are significantly blocked in the microstructured titania devices, thanks to the better isolating lateral layer, compared to the just compact titania layer. Furthermore, the lower series resistances found in the nanostructured titania confirm that there is an improved movement of current through the device, in good agreement with a better crystallization of perovskite material.

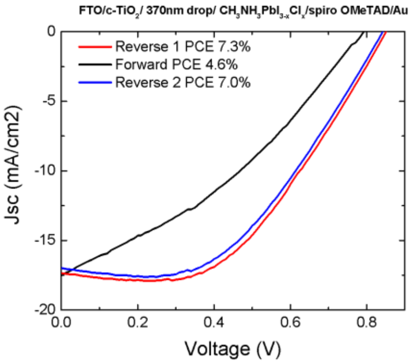

Figure 5.10 Hysteresis measurement of FTO/c-TiO2/370nm drop/Perovskite/Spiro-OmeTAD/Au.

The current voltage curves presented here are scanned from forward bias to short-circuit, i.e. in reverse condition. I observed hysteresis in the J–V curves when measuring in forward condition, with PCE lower than that determined from the current voltage curves measured in reverse condition [187, 188]. For instance in figure 5.10 I show the forward current voltage scans for a device prepared onto the nanostructured titania, which exhibited a J–V derived PCE of 7.3% in reverse bias with a PCE of just over 4.6% in forward. Remarkably, a further measurement from forward bias to short-circuit showed the same behaviour (and PCE) of the first measurement.

5.5 Conclusion

In conclusion, I have presented a low-cost, scalable technique for fabricating highly ordered patterned titanium oxide photonic scaffold. Perovskite solar cells prepared onto these scaffold exhibit efficiencies of about 9%, higher that the standard ones prepared both with mesoporous and compact titania layers.

I attribute this enhancement to an increased light-trapping inside the perovskite active layer induced by the feedback structure and an improved perovskite film formation. Furthermore, thanks to the controlled and uniform thickness of the titania scaffold that can be obtained with these layers, the shunting path are suppressed, resulting in increasing devices efficiency. This work showed the importance of designing novel nanostructured photonic scaffold for photonic and optoelectronic perovskite-based devices.

Chapter 6

Transparent electrodes: preparation, characterization and work-function engineering

In this chapter I report on the morphological, electrical and optical characteristics of single-wall carbon nanotube (SWCNTs) and silver nanowires (AgNWs) films on different transparent substrates, obtained using spray deposition. In particular, I studied the variation of resistance as function of the temperature in networks having different nanotubes density. The obtained results suggest that the change in the temperature behaviour is due to the desorption of oxygen molecules at relatively high temperature and this effect is found to be function of the network density. The computational simulation has been carried out by Dr. Simone Colasanti and Prof. Paolo Lugli (Technical University of Munich, TUM). In conclusion, I have investigated the modification of the work function of the spray-coated thin films induced by the physisorption of PEI (polyethylenimine) as a surface modifier. I find that the work function of the bare thin films is lowered after the deposition of PEI by approximately 0.5 to 1 eV with respect to the pristine films, thereby yielding electrodes with minimum work functions of ~ 3.75 eV. This value makes the films suitable as cathodes in light-emitting diodes (OLEDs) or electron-collecting electrodes in organic photovoltaic diodes (OPVDs). More generally, such results are of relevance to the implementation of flexible and stretchable electronics, as work function tunability is crucial for electrodes engineering, and both AgNWs and SWCNTs are among the best candidates for flexible electrodes in printable electronics. The following chapter is reproduced with permission of IEEE © 2011 IEEE (see ref. [189] and [32]).

6.1 Transparent conductive electrodes

Transparent electrodes are essential components in organic optoelectronic devices including organic light-emitting diodes (OLEDs), displays, and solar cells. In addition to transparency, relevant applications require high conductivity and a work function (WF) that minimizes the barrier for electron injection (in OLEDs) or collection (in organic photovoltaic diodes (OPVDs)) of the organic or hybrid semiconductors used as active layers. In addition to processability at low-cost over large areas, mechanical flexibility is increasingly required, e.g. for applications in which the active device has to conform to non-flat surfaces, or even be stretchable [190]. Whereas ITO has offered over the last decades the best compromise in terms of transparency, conductivity, ease of processing and, to some extent, work function, both scarcity of indium on a global scale and mechanical brittleness [22] limit its application to flexible devices. Transparent CNTs and AgNWs [35] films have been demonstrated to be good candidates to replace ITO thanks to their flexibility, resistance to flexural fatigue, and ease of manufacturing. Random CNTs networks have raised increasing interest due to their applicability in a wide range of different applications in science and engineering [191-193]. Among those applications are transparent electrodes [194-199], transistors and circuits [200, 201], as well as mechanical and chemical sensors [202, 203]. Devices based on CNT films promise high mechanical flexibility and low-weight, therefore being particularly attractive for large-area printed electronics. However, prior to employing these networks in any specific application, it is necessary to evaluate the electro-optical properties of such films and their dependence on different process parameters. For example, in the case of CNTs, the transport mechanisms are still not completely clear, especially at the junction between two tubes. The fact that these networks are comprised of a mixture of nanotubes with different electrical and mechanical properties makes the study of these films a non-trivial task. Furthermore, since the nanotubes are randomly arranged over the substrate, the material is intrinsically irregular. Eventually, the ability to control the work function of these electrodes is of paramount importance to obtain high efficiency devices. Many routes have been carried out to engineer the

WF of electrodes: oxygen plasma [204, 205] has been shown an effective WF modifiers for ITO films, PEDOT:PSS has also widely used to match the WF of ITO and the active layers in optoelectronic devices [206], self-assembled monolayers (SAMs) [207-209], can be used for both tuning the work function and to improve surface wettability and also physisorption of polymers [210] and small molecules [211] is also an effective candidate in the tuning of the WF. Among those, PEI has shown to be a good candidate for lowering the WF of various materials [210, 212, 213].

6.2 Experimental details

SWCNTs and AgNWs thin films have been spray-deposited using an air-atomizing nozzle. The system shown in figure 6.1(a) consists of an automated spray air atomizing spray valve (Nordson EFD, USA) in combination with an overhead motion platform (Precision Valve & Automation, USA). Figure 6.1(b) illustrates a scheme of the various components of the instrumental set-up. Deposition parameters, such as material flow rate, atomizing gas (N_2) pressure, nozzle-to-sample distance, substrate temperature, and motion speed can be adjusted to obtain the desired network. In particular, the final densities of nanotubes used in this work have been adjusted and controlled by varying the number spray cycles, keeping fixed all then parameters listed previously.

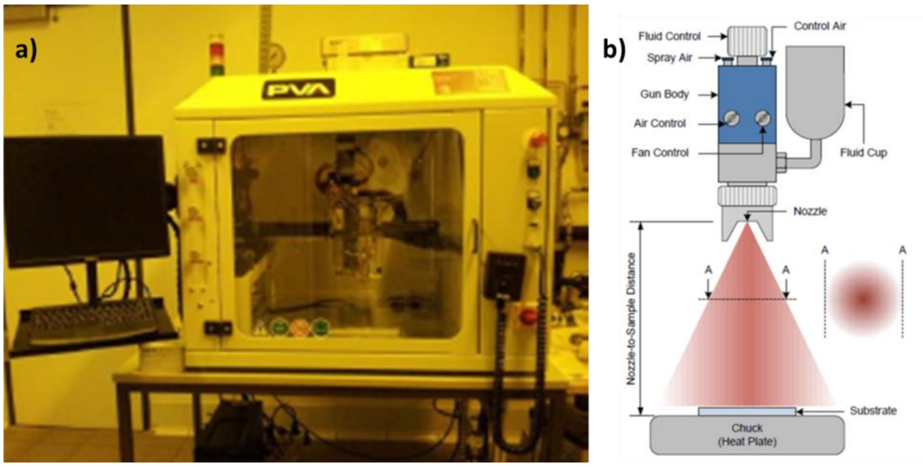

Figure 6.1 (a) Spray-coating set-up and (b) schematic illustration of the components.

The spray-deposition was carried out within the wet spraying regime while heating up the substrate in order to speed up the drying of wet droplets arriving at the substrate [214]. This allowed the optimal merging of the droplets that arrived at the samples and to minimize the coffee stains formation (e.g. when the drying of the droplets is too fast that all the material contained inside flow and accumulate at the edge of the droplet, leaving an unfilled ring of material) [189, 214, 215]. With this approach, I obtained the deposition of a dry layer with a controlled and reproducible thickness. I used aqueous solution of unsorted single-wall CNT (33% metallic, 67% semiconducting, Carbon Solutions, Inc (CSI) or ASP-100F, Hanwha Chemical). In order to prevent aggregation between the nanotubes, I used sodium carboxymethyl cellulose (CMC). I used this surfactant since it has been already reported by Takahashi et al. as optimal for the dispersion of SWCNTs in aqueous solutions [216]. The final dispersion of CNT is obtained starting by preparing the CMC solution in Millipore deionized (DI) water with a concentration of 0.5 wt%. This solution is then stirred overnight at room temperature to completely dissolve the surfactant in water. Then, the desired amount of CNTs have been added to the previously prepared aqueous CMC solution. In this work, I used a concentration of 0.05 wt%. The final dispersion of the carbon nanotubes is achieved by sonication of the as prepared solution for 90 min in a horn sonicator (Branson Sonifier S-450D). Eventually, the solution is centrifuged at 15000 rpm for 90 min and the ready-to-spray solution is obtained by decanting the top 80% of the supernatant. Post deposition treatment is necessary to remove the excess of the CMC that is embedded into CNTs after the spraying procedure and that affect the electrical behavior of the film. For this reason, samples are left immersed overnight in HNO3 (diluted 1:4 with DI water) to remove the surfactant, then in DI water for 15 min to remove remaining acid molecules and finally dried. AgNWs solution (0.5 wt% in DI water, Sigma-Aldrich), was used as received. The mixed AgNWs-SWCNTs thin films were sprayed from a 1:1 solution with different number of spraying cycles, namely 5 and 7. PEI (branched, Sigma Aldrich) was used as received, without further purification. PEI solution 5 wt% in methanol was prepared at room temperature and stirred overnight. For the morphological, electrical and optical characterization plain glass and PET (polyethylene tereftalate) substrates were used. For the temperature behavior I used an inter-digitated electrode structure (IDES) with 200 nm thermally grown SiO_2, 200 μm spacing between the fingers, consisting of a 5 nm thick Cr layer underneath 40 nm of gold as substrate. Prior to spray deposition, I performed an oxygen plasma treatment to all the substrates to increase the wettability. UV-vis characterisation has been carried out with an Agilent 8453 spectrophotometer. Resistance measurements have been performed using a Keithley 2400 source-meter connected to a home-built probe station (XYZ 500 Right and Left Micropositioners from Quater Research). Temperature was varied via hotplate and controlled using a type K thermocouple. Measurements in nitrogen have been performed inside an MBraun glovebox (O2<0.1 ppm, H2O<0.1 ppm). Surface morphology has been investigated by using an atomic force microscopy (Dimension 3100, Brucker). For the work function characterization, I have used a macroscopic Kelvin probe (KP) in air (at room temperature, RT) calibrated against a freshly-cleaved highly-oriented pyrolytic graphite, HOPG, surface. I estimate the uncertainty on these measurements to be ±0.05 eV.

6.3 Electrical and Optical characterization

In figure 6.2(a) I reported the transmittance spectra collected for the neat films onto glass substrates. The highest transmittance has been achieved for the bare AgNWs, 81% at 550 nm for the film and glass. The AgNWs electrodes is only slightly less transparent (~7%) compared to an ITO electrode. Interestingly, this spectrum shows two dip at 353 and 377 nm due to the localized surface plasmon resonance of these anisotropic metallic nanostructures [113]. Such optical feature might be exploited in photovoltaic devices, as they can enhance the light harvesting [217]. As expected, the AgNW-CNTs films transmittance decreases by increasing the dose (67% for the 5 deposition and 59% for the 7 deposition, both values are for the films and glass together). SWCNTs neat film has a comparable transmittance as the 7x and it does not show any plasmonic resonance. The sheet resistance measurements (figure. 6.2(b)) show that the AgNWs-based thin films I achieved the lower values of approximatively between 15 and 22 Ω/□. These values are promising for using these films as electrodes, since they match the sheet-resistance of the most widely used ITO and FTO[218], In particular, the best trade-off between transmittance and sheet resistance is obtained for the neat AgNWs neat films. On the other hand, SWCNTs neat films show a high sheet-resistance, making them less suitable for optoelectronic devices.

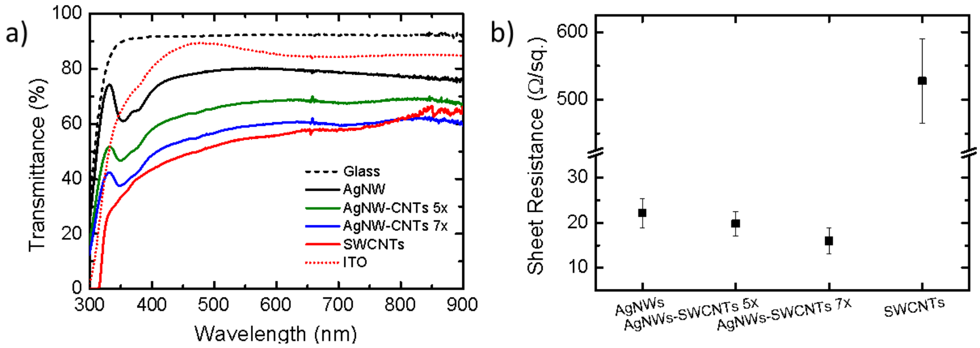

Figure 6.2 (a) Transmittance spectra (solid lines) for the various films deposited onto soda lime glass slides compared to the transmittance of the bare glass slide (black dashed line) and ITO onto glass (red dotted line). (b) Sheet resistance measured using a four points probe for the various thin films.

Atomic Force Microscopy (AFM) images have been carried out to estimate the morphology of the films (figure 6.3 (a-d)).

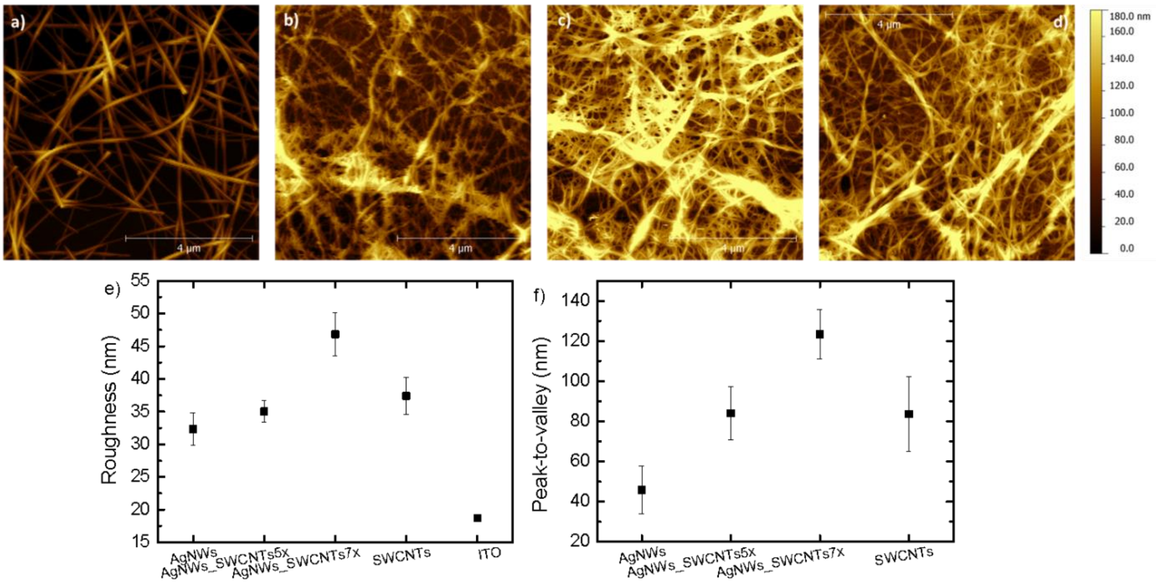

Figure 6.3 (a-d) Atomic force microscopy topographies (tapping mode) of (a) AgNWs, (b) 5x AgNWs-SWCNTs, (c) 7x AgNWs-SWCNTs, (d) SWCNTs thin films. Height scale has been kept equal for each sample. (e) Roughness of the films (included for an ITO film), that represents the standard deviation of surface heights calculated from AFM data and (f) Peak-to-valley distances for the thin films.

Interestingly, both films roughness and peak-to-valley distances follow the same trend for all the samples. The best morphological features, in terms of lower roughness and peak-to-valley, have been observed for the AgNWs neat films and the thinner film of the mixture AgNWs-SWCNTs. For those samples I observed a roughness of about 32 nm and 35 nm respectively and a peak-to-valley of about 45 nm and 84 nm respectively (figure 6.3(e-f)).

Although these values are higher than the one of ITO [219, 220], they are low enough to enable these films to be used as transparent electrodes, since both values are lower than the thickness of a typical semiconducting film used as active layer (about 90 nm).

I then focused on the SWCNTs networks (for which the deposition method was better optimized at the time the measurements were carried out) to check the possibility to prepare thin film onto flexible substrates. In this case I sprayed two different doses of SWCNTs solution on PET foils and glass substrates as reference.

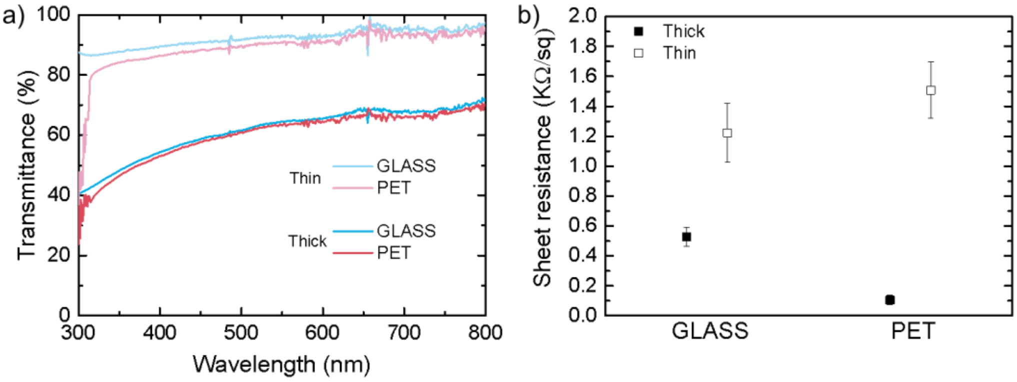

Figure 6.4 (a) Transmittance spectra for the films deposited onto soda lime glass slides (blue and light blue lines) and PET foils (red and light red lines) for the two thickness tested. (b) Sheet resistance measured using a four points probe for films prepared onto soda lime glass slide and PET foil. The value obtained for the film onto glass slide (for the thick sample) is comparable to previous results, thus suggesting an optimal reproducibility of the preparation method. Adapted from ref. [189].

The transmittance spectra are reported in figure 6.4(a). To avoid any effect induced by the substrates, and so to isolate the deposited films, I used as blank reference the bare glass and PET foil. For the lower dose the mean transmittance is similar for both film and is 92% at 550 nm. For the thicker one, the transmittance is 64%, similar to the one reported in the before. For both doses I found that the transmittance was not influenced by the substrates, thus suggesting a comparable wettability between them. This is further confirmed by the sheet resistance measurements. In fact, the obtained values (reported in figure 6.4(b)) are similar for bot samples and for the higher dose (i.e. thick layers) those are comparable with the one reported before.

6.4 Temperature behaviour

Another crucial parameter I focused on was the resistance variation with respect to the temperature for SWCNT networks. Prior to measure and calculate the electrical properties, it is necessary to evaluate the network morphology. From AFM images it is possible to infer the SWCNTs densities of the film. The samples I measured have shown a very low density of SWCNTs/µm^2, as it is presented in figure 6.5.

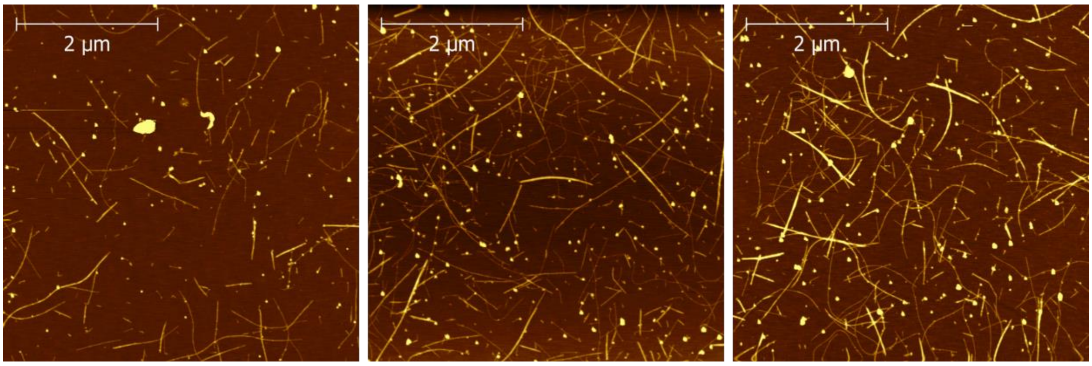

Figure 6.5 AFM images of the CNTs networks with increasing densities, namely 12 CNT/µm^2, 18 CNT/µm^2 and 24 CNT/µm^2. Adapted from ref. [32]

The experimental and simulated curves of the resistance-temperature behavior for networks with low, medium and high densities, namely 12 CNT/µm^2, 18 CNT/µm^2 and 24 CNT/µm^2 are shown in figure 6.6. These measurements have been recorded in ambient condition on two different wafers with 9 devices each.

For the nanotubes, the expression of the resistance follows equation (35):

$$R(V) = R_o(V)(1 + {}^{L}/_{\lambda_{eff}}) \tag{35}$$

where R_0 represents the so-called quantum resistance, L is the length of the tube segment and λ_{eff} is the effective mean free path, which contains the effects due to phonon scattering events [221, 222]. The quantum resistance is calculated as the ratio between the applied voltage and the current that flows through the nanotube[223]. The resistances of the nanotubes junctions do not follow equation (35), but are values taken from the literature. I referred in particular to the work by Fuhrer et al. [33] where the resistance of different junctions has been experimentally measured. In the simulations these resistances are set variable to take into account the disorder) with a narrow uniform distribution around the mean values of 250 kΩ for metallic-metallic junctions and 500 kΩ for semiconducting-semiconducting junctions. For metallic/semiconducting CNT junctions the physics of the conduction is more complex, as Fuhrer et. al. pointed out. The behaviour resembles the one of a Schottky barrier, as it is explained and theoretically predicted in [224]. For these type of junctions, the following expression is valid:

$$R_{(M-S)} = R_{(M-S)o}(^{T_0}/_{T})^{3/2} \qquad (36)$$

where $R_{(M\text{-}S)0}$ is the resistance at 50 K, calculated as the slope of the experimental I-V curve for the Schottky diode from [33], and T_0 the corresponding reference temperature, which is equal to 50 K. Values are typically around 1 MΩ at room temperature.

I observed that for all the samples the resistance decreases as function of the temperature, but the decay is strongly affected by the densities of the films. In particular, for the higher density networks the resistance decrease almost linearly with the temperature and until 90°C I did not observe any minimum.

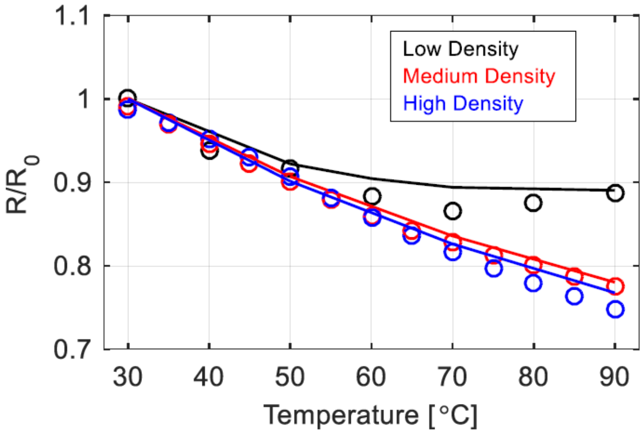

Figure 6.6 Measured (circles) and calculated (solid lines) relative resistance (defined as the ratio between the initial resistance and the measured one at different temperature) of three CNTs networks with different densities. The resistance decreases by increasing the temperature for the denser networks. Instead, for the network with 12 CNTs/µm2 I observe the presence of a minimum in the resistance. I thank Simone Colasanti for the simulation. Taken from ref. [32].

On the other hand, for the lower density networks, namely 9 CNT/µm^2, the resistance reaches a minimum at relatively low temperature (70 °C) before increasing again. Interestingly, this U-shape in the resistance has not been observed for the networks with higher densities and it became particularly severe by lowering the numbers on CNTs.

This increase in the resistance could be attributed both to a thermally activated oxygen desorption or to a more pronounced metallic behaviour in low-density networks. The role of oxygen and other molecules has already been extensively studied on single CNT, both experimentally [19] and theoretically [20]. Charge transfer from the molecules alters dramatically the electronic properties of the nanotubes and it has been shown that the oxygen has a p-doping effect on the nanotubes, making them more conductive. Desorption of oxygen, instead, results in an increase of the resistance because the CNTs tend to become less doped, thus less conductive. In the simulations this phenomenon is introduced by a certain temperature-dependent rate for desorption of the oxygen. This rate will change the position in energy of the Fermi level and it will affect the electronic transport through the nanotubes[223, 225]. The observed U-shape seems to be more related to the oxygen effect rather than a change from a semiconducting to metallic behaviour of the network. First evidence supporting this assumption is that the metallic/semiconducting ratio does not change with respect of the density of the film. On the other hand, by lowering the density, the active surface of the nanotubes exposed to air increases and, in turns, the reaction sites for the oxygen to be adsorbed/desorbed increase as well.

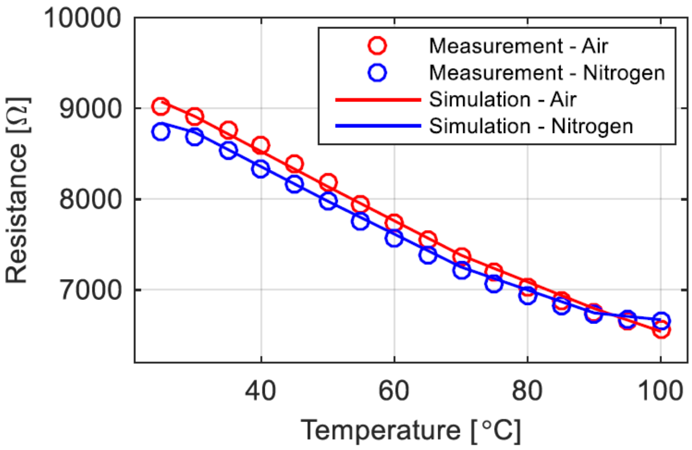

Figure 6.7 Temperature dependency of the resistance for a network with 16 CNTs/μm2 measured and simulated in air (red) and under nitrogen (blue). The different behavior of the network could be attributed to a different oxygen desorption from the CNTs in the two environments. I thank Simone Colasanti for the simulation. Taken from ref. [32].

To have a better insight on the conduction properties of the CNTs networks, and to further attribute the role of the oxygen, I carried out resistance versus temperature measurements both in ambient condition and under a nitrogen atmosphere. The experimental results for networks with densities around 16 CNT/μm^2 are shown in figure 6.7. Here, I observed that the same network behaves differently in ambient condition and in nitrogen environment. In particular, in nitrogen the resistance of the network shows a plateau at around 90 °C, whereas in ambient condition the resistance has a monotonic decreasing behavior. This effect could be induced by a more pronounced oxygen desorption when the sample is measured in nitrogen. In fact, in this condition, the oxygen that is released by the CNT could not be replaced after increasing the temperature. The behavior of the network respect to the temperature can be reduced to two concurrent phenomena: an increase of the temperature facilitates the carriers to cross the barriers at the junctions and, at the same time, reduces the amount of dopants, thus the intrinsic conductivity of the nanotubes. Depending on the initial content of oxygen, one of the two phenomena is predominant respect to the other. These results are consistent with other groups findings. In particular, Barnes et al. [226] investigated the effects of doping and temperature on the conductivity of CNTs networks, declaring the dopant desorption to be the main cause of the observed hysteresis in the measurements.

6.5 Work function engineering

The measurement of the work function has been done on the pristine sample and after each deposition of the PEI solution and annealing treatment. More precisely, the sequence of the applied treatments is the following: after a first work function measurement on the as-prepared samples, I spin-coated the PEI solution onto the film (40 µl, 4000 rpm) and I measured the work function. I then left the films overnight in air at RT before annealing them (Annealing I: 50 °C for 30 minutes in air) to completely remove the residual solvent. After measuring the work function, I deposited 40 µl of the same solution by drop casting before a further work function measurement. After 5 hours I carried out a further annealing (Annealing II: 50 °C for 30 minutes in air) because the solvent had not yet fully evaporated. I then measured the work function again, although the films did not appear to be completely dry, after which I left them overnight in air at RT. After a further annealing (Annealing III: 50 °C for 30 minutes in air) I carried out a final work function measurement on the films that at this time appeared to be essentially dry.

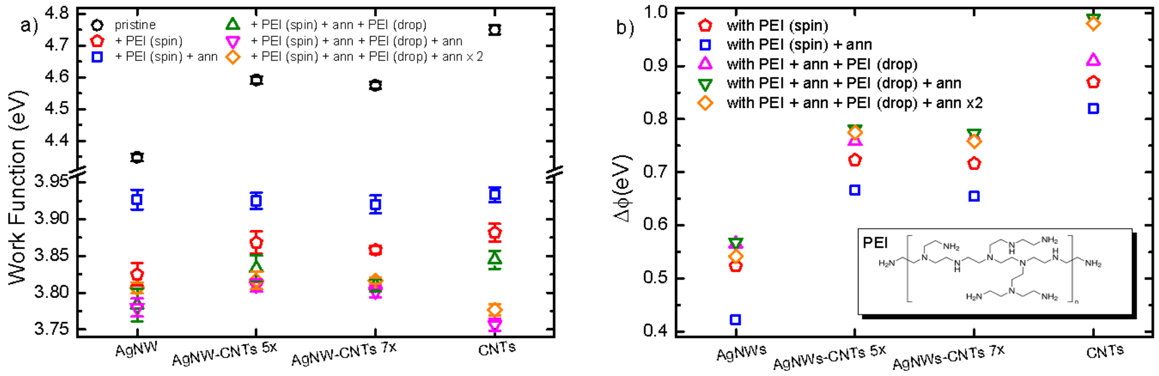

Figure 6.8 WF measured (a) on the thin films before (black circle) and after different PEI deposition and/or thermal treatments. (b) Difference between the WF after each treatment and the pristine values. Inset: PEI chemical structure.

I report the results in figure 6.8. First, I note that the pristine samples show the highest work function (4.34 eV for AgNWs, 4.57-4.59 eV for the mixed samples, and 4.75 eV for the SWCNTs). In addition, the film thickness does not influence significantly the work function of the mixed films. The work function of the mixed AgNWs-SWCNTs is, as expected, found to lie in between that of the constituting elements, i.e. AgNWs (4.34 eV) and SWCNTs (4.75eV). The work function of the AgNWs is in very good agreement with that reported previously for films of aggregates of Ag nanoparticles with dimensions of ~ 30 nm (between 4.32 eV and 4.34 eV) [227] but slightly lower than reported for continuous Ag films (4.6 eV) by the Georgiatech group, that introduced the use of PEI [210]. Interestingly, after spin-coating the PEI I observe a decrease in the work function for all the samples, namely from 4.34 eV to 3.82 eV for the AgNWs, from ~ 4.59 eV to a minimum of 3.85 eV (virtually identical to that of the AgNWs, considering the standard uncertainty of the measurement) for the thickest mixed film and from 475eV to 3.88eV for the SWCNTSs (red pentagons in Fig. 6.8(a)). This decrease is essentially in line with previous work [210] reporting lowering of the work function of continuous Ag thin films by 1 eV (from 4.6 eV to 3.6 eV) after spin-coating an ultrathin film (1-10 nm) of PEI. In this case I measure a difference of ~0.6 eV for the pure AgNWs, which is slightly lower than for the continuous films. I estimate that this could be due to a difference in the density and orientation of the dipolar groups introduced by the PEI as a consequence of differences in the surface morphologies and/or of the PEI thickness.

Upon first annealing, I also observe an unexpected but minor increase of the work function for all the samples (blue square in figure 6.8(a)). This slight increase might be related to evaporation of the polar solvent (methanol) or to a surface oxidation (the annealing has been carried out in air). Further deposition of PEI by drop-casting induced again a decrease of the WF for all the samples, in particular, I measured a work function of 3.78 eV for AgNWs, 3.81-3.83 eV for AgNWs-SWCNTs and 3.76 eV for SWCNTs (green triangle in figure 6.8(a)). This observation would be consistent with a more substantial filling of the voids in the films. Surprisingly, the final WF measured for the SWCNTs is identical to the one of the AgNWs, since the $\Delta\phi$ induced by the PEI onto those films is 1 eV and 0.6 eV respectively.

Further two annealing (pink triangle and orange diamond in figure 6.8(a)) have not essentially changed the WF values for all the samples, maybe due to a complete pore filling after the first drop-casting of methanolic solution. It is surprising, however, that the final work function is similar for both SWCNTs, AgNWs and mixed films, thus implying a difference in the $\Delta\phi$ induced by the PEI deposition (figure 6.8(b)). This could be due to a different physisorption on the different materials (e.g., again, in the density of PEI molecules that are effectively physisorbed or in the dipoles orientation). However, I also consider it possible that the effectiveness of the PEI is higher for the SWCNTs instead for the AgNWs. In fact, the lowering of the WF has been attributed to both the presence of the internal dipole inside the PEI, orientated perpendicularly to the thin film surface, and the surface dipole at the interface between the PEI and the electrode surface, again along the direction perpendicular to the films surface [228]. Since the latter dipole has been attributed to an electron transfer from the amine group of the PEI to the electrodes [210], the difference in $\Delta\phi$ could be assigned to the different electron affinity of the silver and the SWCNTs, namely 1.3 eV [229] and ~3 eV [230].

6.6 Conclusion

In conclusion, I compared the morphological, electrical and optical characteristics of SWCNTs and AgNWs thin films on different substrates, obtained using spray deposition. These films show comparable morphological characteristic sheet resistance and transmittance to standard transparent electrodes, making them suitable for application in flexible optoelectronic devices. Then I measured and modelled the temperature behaviour for SWCNTs networks with various densities and under different environmental condition. The good agreement between experimental and computational results allowed me to validate the model. I observed that the temperature behaviour is strongly affected by the networks densities. To further investigate the physical phenomena that cause such differences, I carried out the analysis also in nitrogen atmosphere. This allowed me to estimate the effect of the temperature and the oxygen on the film resistance. Finally, I have obtained a modification of the work function of AgNWs, SWCNTs and mixed AgNWs-SWCNTs thin films following spin-coating or drop-casting of PEI. The work function of the AgNWs films is reduced from 4.34 eV to 3.78 eV; the work functions of the mixed films are reduced from 4.57-4.59 eV to 3.78-3.81 eV; and the SWCNTs from 4.75 eV to 3.75 eV. All these results confirm that these films should be suitable as flexible cathodes/electron collecting electrodes for flexible OLEDs/OPVDs.

Conclusions and outlook

Micro- and nano-structures represent a powerful tool to investigate fundamental properties of light-matter interactions and for optoelectronic applications.

In particular, in this thesis I have shown how these architectures have a potential for applications in three different fields: light emission modification, light harvesting and transparent conductive electrodes.

In the first part, the use of photonic nanostructures opened the possibility to control the spontaneous emission of an embedded light-emitting material. In fact, the photonic band gap of a photonic crystal can either inhibit or enhance spontaneous emission by modifying its radiative rate. In addition, the cross section of stimulated emission directly depends upon the radiative rate of the material. Therefore, increasing the radiative rate directly decreases the stimulated emission threshold.

In Chapter 3, I have fabricated and fully characterised hybrid carbon-silicon luminescent photonic structures by electrochemical etching of silicon followed by effective infiltration of a high-efficiency green emitting conjugated polymer. Remarkably, a modification of the emission lifetime of the luminescent polymer due to the modulation of the photonic density of states inside the photonic structure is observed. These polymer-infiltrated Si-based crystals powerfully exemplify an element of a potential tool library of a “C-Si hybrid photonic platform”.

In Chapter 4, an all-plastic photonic crystal functionalized with conjugated polyrotaxanes shows a wavelength dependent enhancement/suppression of the photoluminescence intensity. The emission modification is induced by the photonic crystal, which modulates the photonic density of states.

The photonic crystals presented in this work represent an interesting and cheap way to modify the emission properties of the infiltrated material and can potentially lead to lasing emission. In particular, both novel photonic structures and conjugated polymers need to be developed and investigated to achieve both optically or, even more interesting, electrically pumped lasing. An obvious area of research is the preparation and characterization of inverse opal structures, starting from the “direct” ones presented in this work. This structures have a complete photonic-band gaps (in all three dimensions), therefore opening up the possibility to a stronger modification of the emission of dyes here observed. Furthermore, those could be prepared in a variety of material, such as titania, silica, ZnO and so forth. Another area of future work should involve the production and characterisation of optical microcavities, i.e. structures formed by photonic crystals-based reflecting layers on the two sides of an optical spacers (defined as defect). This structures could be used to obtain lasing emission from a dye infiltrated/coated in the optical spacers thanks to the strong modification of the photonic density of states induced by the structure.

In the second part of this thesis I have shown how it is possible to implement nanostructures into photovoltaic devices.

In Chapter 5, by photonically patterning with a simple bottom-up technique the electron transport layer, the external quantum efficiency of an organo-halide perovskite solar cell increases of about 100%. The increase in external quantum efficiency is attributed to two concomitant effects: an enhanced light-trapping induced by the scattering layer and an improved perovskite crystallization onto this highly porous structures. Furthermore, the possibility to perfectly control the layer formation, allowed me to find the optimal thickness.

The results presented here demonstrate that photonic nanostructures implemented in perovskite-based solar cell enhance its power-conversion efficiency. Light absorption is amplified as a result of the light scattering. These results demonstrate that the colloidal lithography is suitable for being implemented in quality in photovoltaic devices in order to boost their performance. This opens the door for the conscious optimization of the photonic structures, tailoring their optical properties in order to better cover the solar spectrum. The presented technique for the fabrication of nano- patterned solar cells should be improved as future to further increase the efficiency of the devices, to reach values comparable to the state-of -art. In particular, the preparation of the organo-halide perovskite layer and its deposition onto the ETL have to be improved.

Finally, in the third part of this thesis I have shown a scalable method to prepare nanostructured conductive thin films.

In Chapter 6, I presented a reliable and reproducible spray deposition process for the fabrication of highly uniform CNTs and AgNWs films onto rigid and flexible substrates, achieving a good trade-off between sheet resistance and transmittance. I carried out the deposition of Polyethylenimine onto these thin films, obtaining a reduction on the work function up to 1eV. In addition, I studied the temperature behaviour of CNTs network, pointing out the role of oxygen desorption.

The results presented have high potential for the fabrication of CNTs and AgNWs thin films with state-of-art performance on various transparent substrate materials. Future work in this area will be related to the implementation of this electrodes into light-emitting diodes and photovoltaic devices. Furthermore, the use of PEI for the fine tuning of the work function of the electrodes can be further developed in two ways. An optimisation of the film deposition, especially in terms of thickness (for example using a self-assembled monolayer with all the dipoles oriented in the same direction) is expected to lead to a further improvement of the tuning. Then, these functionalised electrodes could be implemented in optoelectronic devices.

References

[1] E. Yablonovitch, Phys. Rev. Lett., 58 (1987) 2059.

[2] S. John, Phys. Rev. Lett., 58 (1987) 2486.

[3] J.D. Joannopulos, R.D. Meade, J.N. Win, Photonic Crystals: Molding the Flow of the Light, Princeton University Press, Princeton, 1995.

[4] R.F. Cregan, B.J. Mangan, J.C. Knight, T.A. Birks, P.S.J. Russell, P.J. Roberts, D.C. Allan, Science, 285 (1999) 1537-1539.

[5] Y. Liu, H.W.M. Salemink, Opt. Express, 20 (2012) 19912-19920.

[6] S. Guldin, S. Hüttner, M. Kolle, M.E. Welland, P. Müller-Buschbaum, R.H. Friend, U. Steiner, N. Tétreault, Nano Lett., 10 (2010) 2303-2309.

[7] C. Wiesmann, K. Bergenek, N. Linder, U.T. Schwarz, Laser & Photonics Reviews, 3 (2009) 262-286.

[8] N. Tessler, G.J. Denton, R.H. Friend, Nature, 382 (1996) 695-697.

[9] I.D.W. Samuel, G.A. Turnbull, Materials Today, 28 (2004) 28.

[10] I.D.W. Samuel, G.A. Turnbull, Chemical Reviews, 107 (2007) 1272-1295.

[11] C.K. Chiang, C.R. Fincher, Y.W. Park, A.J. Heeger, H. Shirakawa, E.J. Louis, S.C. Gau, A.G. MacDiarmid, Phys. Rev. Lett., 39 (1977) 1098-1101.

[12] J.H. Burroughes, D.D.C. Bradley, A.R. Brown, R.N. Marks, K. Mackay, R.H. Friend, P.L. Burns, A.B. Holmes, Nature, 347 (1990) 539-541.

[13] C.W. Tang, Appl. Phys. Lett., 48 (1986) 183-185.

[14] NREL.

[15] H.J. Snaith, The Journal of Physical Chemistry Letters, 4 (2013) 3623-3630.

[16] M. Pisco, A. Cusano, A. Cutolo, Photonic Bandgap Structures Novel Technological Platforms for Physical, Chemical and Biological Sensing, Bentham Books2012.

[17] E. Hecht, Optics, (1990.

[18] K. Sakoda, Optical properties of photonic crystals, Springer2005.

[19] E. Pavarini, L.C. Andreani, C. Soci, M. Galli, F. Marabelli, D. Comoretto, Phys. Rev. B, 72 (2005) 045102.

[20] M. Barth, A. Gruber, F. Cichos, Phys. Rev. B, 72 (2005) 085129.

[21] E. Merzbacher, Quantum Mechanics, 3rd ed.1998.

[22] V. Zardetto, T.M. Brown, A. Reale, A. Di Carlo, J. Polym. Sci. B: Polym. Phys., 49 (2011) 638-648.

[23] R.G. Gordon, MRS Bulletin, 25 (2000) 52-57.

[24] D. Alemu, H.-Y. Wei, K.-C. Ho, C.-W. Chu, Energy & Environmental Science, 5 (2012) 9662-9671.

[25] S. Iijima, Nature, 354 (1991) 56-58.

[26] S. Iijima, T. Ichihashi, Nature, 363 (1993) 603-605.

[27] P.J.F. Harris, Carbon Nanotubes and Related Structures, Cambridge University Press1999.

[28] M.S. Dresselhaus, G. Dresselhaus, P. Avouris, S-Verlag Berlin, Heidelberg and New York, (2001) 12-25.

[29] S. Xie, W. Li, Z. Pan, B. Chang, L. Sun, Journal of Physics and Chemistry of Solids, 61 (2000) 1153-1158.

[30] X. Wan, J. Dong, D.Y. Xing, Phys. Rev. B, 58 (1998) 6756-6759.

[31] X. Lu, Z. Chen, Chemical Reviews, 105 (2005) 3643-3696.

[32] S. Colasanti, V. Robbiano, F.C. Loghin, A. Abdelhalim, V.D. Bhatt, A. Abdellah, F. Cacialli, P. Lugli, IEEE Transactions on Nanotechnology, 15 (2016) 171-178.

[33] M.S. Fuhrer, J. Nygård, L. Shih, M. Forero, Y.-G. Yoon, M.S.C. Mazzoni, H.J. Choi, J. Ihm, S.G. Louie, A. Zettl, P.L. McEuen, Science, 288 (2000) 494-497.

[34] S. Hong, S. Myung, Nat Nano, 2 (2007) 207-208.

[35] D.S. Hecht, L. Hu, G. Irvin, Advanced Materials, 23 (2011) 1482-1513.

[36] R.B. Weisman, Nat Mater, 2 (2003) 569-570.

[37] K. Ihara, H. Endoh, T. Saito, F. Nihey, J. Phys. Chem. C, 115 (2011) 22827-22832.

[38] A.A. Green, M.C. Hersam, Adv. Mater., 23 (2011) 2185-2190.

[39] R. Krupke, F. Hennrich, H.v. Löhneysen, M.M. Kappes, Science, 301 (2003) 344-347.

[40] M.S. Arnold, A.A. Green, J.F. Hulvat, S.I. Stupp, M.C. Hersam, Nat Nano, 1 (2006) 60-65.

[41] S. Mesgari, Y.F. Poon, L.Y. Yan, Y. Chen, L.S. Loo, Y.X. Thong, M.B. Chan-Park, J. Phys. Chem. C, 116 (2012) 10266-10273.

[42] M.J. O'Connell, S.M. Bachilo, C.B. Huffman, V.C. Moore, M.S. Strano, E.H. Haroz, K.L. Rialon, P.J. Boul, W.H. Noon, C. Kittrell, J. Ma, R.H. Hauge, R.B. Weisman, R.E. Smalley, Science, 297 (2002) 593-596.

[43] B. O'Connor, C. Haughn, K.-H. An, K.P. Pipe, M. Shtein, Appl. Phys. Lett., 93 (2008) 223304.

[44] R.B. Pode, C.J. Lee, D.G. Moon, J.I. Han, Appl. Phys. Lett., 84 (2004) 4614-4616.

[45] D.S. Ghosh, L. Martinez, S. Giurgola, P. Vergani, V. Pruneri, Opt. Lett., 34 (2009) 325-327.

[46] M.-G. Kang, M.-S. Kim, J. Kim, L.J. Guo, Adv. Mater., 20 (2008) 4408-4413.

[47] J. van de Groep, P. Spinelli, A. Polman, Nano Letters, 12 (2012) 3138-3144.

[48] S. De, T.M. Higgins, P.E. Lyons, E.M. Doherty, P.N. Nirmalraj, W.J. Blau, J.J. Boland, J.N. Coleman, ACS Nano, 3 (2009) 1767-1774.

[49] D. Azulai, T. Belenkova, H. Gilon, Z. Barkay, G. Markovich, Nano Lett., 9 (2009) 4246-4249.

[50] J.-Y. Lee, S.T. Connor, Y. Cui, P. Peumans, Nano Lett., 8 (2008) 689-692.

[51] S. Ye, A.R. Rathmell, Z. Chen, I.E. Stewart, B.J. Wiley, Adv. Mater., 26 (2014) 6670-6687.

[52] J. Lee, P. Lee, H. Lee, D. Lee, S.S. Lee, S.H. Ko, Nanoscale, 4 (2012) 6408-6414.

[53] D.-S. Leem, A. Edwards, M. Faist, J. Nelson, D.D.C. Bradley, J.C. de Mello, Adv. Mater., 23 (2011) 4371-4375.

[54] F. Selzer, Wei, D. Kneppe, L. Bormann, C. Sachse, N. Gaponik, A. Eychmuller, K. Leo, L. Muller-Meskamp, Nanoscale, 7 (2015) 2777-2783.

[55] D. Angmo, T.R. Andersen, J.J. Bentzen, M. Helgesen, R.R. Søndergaard, M. Jørgensen, J.E. Carlé, E. Bundgaard, F.C. Krebs, Adv. Funct. Mater., 25 (2015) 4539-4547.

[56] C. Hwang, J. An, B.D. Choi, K. Kim, S.-W. Jung, K.-J. Baeg, M.-G. Kim, K.M. Ok, J. Hong, Journal of Materials Chemistry C, 4 (2016) 1441-1447.

[57] A.R. Rathmell, S.M. Bergin, Y.-L. Hua, Z.-Y. Li, B.J. Wiley, Adv. Mater., 22 (2010) 3558-3563.

[58] V. Robbiano, F. Di Stasio, S. Surdo, S. Mian, G. Barillaro, F. Cacialli, Hybrid-Organic Photonic Structures for Light Emission Modification, in: D. Comoretto (Ed.) Organic and Hybrid Photonic Crystals, Springer International Publishing, Cham, 2015, pp. 339-358.

[59] S. Noda, A. Chutian, M. Imada, Nature, 407 (2000) 608.

[60] S.Y. Lin, J.G. Fleming, D.L. Hetherington, B.K. Smith, R. Biswas, K.M. Ho, M.M. Sigalas, W. Zubrzycki, S.R. Kurtz, J. Bur, Nature, 394 (1998) 251-253.

[61] L. Mai, F. Ding, T. Stöferle, A. Knoll, B. Jan Offrein, R.F. Mahrt, Applied Physics Letters, 103 (2013) -.

[62] A. Jebali, R.F. Mahrt, N. Moll, D. Erni, C. Bauer, G.-L. Bona, W. Bächtold, J. Appl. Phys., 96 (2004) 3043-3049.

[63] N. Moll, T. Stöferle, S. Schönenberger, R.F. Mahrt, Opt. Express, 17 (2009) 20998-21006.

[64] S. Kawata, H. Sun, T. Tanaka, K. Takada, Nature, 412 (2001) 697.

[65] S. Maruo, O. Nakamura, S. Kawata, Opt. Lett., 22 (1997) 132-134.

[66] L. Frezza, M. Patrini, M. Liscidini, D. Comoretto, J. Phys. Chem. C, 115 (2011) 19939-19946.

[67] G. Canazza, F. Scotognella, G. Lanzani, S.D. Silvestri, M. Zavelani-Rossi, D. Comoretto, Laser Physics Letters, 11 (2014) 035804.

[68] V. Lehmann, H. Föll, Journal of The Electrochemical Society, 137 (1990) 653-659.

[69] G. Barillaro, A. Nannini, M. Piotto, Sensors and Actuators A: Physical, 102 (2002) 195-201.

[70] M. Bassu, S. Surdo, L.M. Strambini, G. Barillaro, Advanced Functional Materials, 22 (2012) 1222-1228.

[71] H. Ning, N.A. Krueger, X. Sheng, H. Keum, C. Zhang, K.D. Choquette, X. Li, S. Kim, J.A. Rogers, P.V. Braun, ACS Photonics, 1 (2014) 1144-1150.

[72] G. Barillaro, L.M. Strambini, V. Annovazzi-Lodi, S. Merlo, Selected Topics in Quantum Electronics, IEEE Journal of, 15 (2009) 1359-1367.

[73] C. Pacholski, Sensors, 13 (2013) 4694-4713.

[74] L. Dähne, S. Leporatti, E. Donath, H. Möhwald, J. Am. Chem. Soc., 123 (2001) 5431-5436.

[75] K.C. Krogman, R.E. Cohen, P.T. Hammond, M.F. Rubner, B.N. Wang, Bioinspiration & Biomimetics, 8 (2013) 045005.

[76] G.D. Moon, T.I. Lee, B. Kim, G. Chae, J. Kim, S. Kim, J.-M. Myoung, U. Jeong, ACS Nano, 5 (2011) 8600-8612.

[77] A. Belardini, A. Benedetti, M. Centini, G. Leahu, F. Mura, S. Sennato, C. Sibilia, V. Robbiano, M.C. Giordano, C. Martella, D. Comoretto, F.B. de Mongeot, Advanced Optical Materials, 2 (2014) 208-213.

[78] A.F. Koenderink, P.M. Johnson, J.F.G. Lopez, W.L. Vos, C.R. Physique, 3 (2002) 67.

[79] A. Hartsuiker, W.L. Vos, Langmuir, 24 (2008) 4670-4675.

[80] D. Comoretto, R. Grassi, F. Marabelli, L.C. Andreani, Mat. Sci. Eng. C, 23 (2003) 61.

[81] A. Bolognesi, C. Mercogliano, S. Yunus, M. Civardi, D. Comoretto, A. Turturro, Langmuir, 21 (2005) 3480.

[82] N.P. Johnson, D.W. McComb, A. Richel, B.M. Treble, R.M.D.L. Rue, Synth. Met., 116 (2001) 469.

[83] H. Míguez, F. Meseguer, C. Lopez, F. López-Tejeira, J. Sunchez-Dehesa, Adv. Mater., 13 (2001) 393.

[84] J.F. Galisteo-Lopez, W.L. Vos, Phys. Rev. E, 66 (2002) 036616.

[85] G. Horowitz, Adv. Mater., 10 (1998) 365.

[86] V. Coropceanu, J. Cornil, D.A. da Silva Filho, Y. Olivier, R. Silbey, J.-L. Brédas, Chemical Reviews, 107 (2007) 926-952.

[87] A.J. Heeger, S. Kivelson, J.R. Schrieffer, W.P. Su, Reviews of Modern Physics, 60 (1988) 781-850.

[88] F. Dubin, R. Melet, T. Barisien, R. Grousson, L. Legrand, M. Schott, V. Voliotis, Nat Phys, 2 (2006) 32-35.

[89] J. Bardeen, Physical Review, 49 (1936) 653-663.

[90] C.J. Knill, J.F. Kennedy, Surfaces, Oxford University Press, Oxford, 1999.

[91] L. Kelvin, The London, Edinburgh, and Dublin Philosophical Magazine and Journal of Science, 46 (1898) 82-120.

[92] W.A. Zisman, Review of Scientific Instruments, 3 (1932) 367-370.

[93] J.R. Lakowicz, Principles of Fluorescence Spectroscopy, Kluwer Academic / Plenum Publishers, New York, 1999.

[94] J.R. Lakowicz, G. Weber, Biochemistry, 12 (1973) 4161-4170.

[95] F.C. Spano, C. Silva, Annual Review of Physical Chemistry, 65 (2014) 477-500.

[96] S. Siddiqui, F.C. Spano, Chem. Phys. Lett., 308 (1999) 99-105.

[97] T.-B. Song, Q. Chen, H. Zhou, C. Jiang, H.-H. Wang, Y. Yang, Y. Liu, J. You, Y. Yang, Journal of Materials Chemistry A, 3 (2015) 9032-9050.

[98] M.M. Lee, J. Teuscher, T. Miyasaka, T.N. Murakami, H.J. Snaith, Science, 338 (2012) 643-647.

[99] M.A. Green, A. Ho-Baillie, H.J. Snaith, Nat Photon, 8 (2014) 506-514.

[100] C. Li, X. Lu, W. Ding, L. Feng, Y. Gao, Z. Guo, Acta Crystallographica Section B, 64 (2008) 702-707.

[101] J.-H. Im, I.-H. Jang, N. Pellet, M. Grätzel, N.-G. Park, Nat Nano, 9 (2014) 927-932.

[102] G.E. Eperon, V.M. Burlakov, P. Docampo, A. Goriely, H.J. Snaith, Adv. Funct. Mater., 24 (2014) 151-157.

[103] G. Giorgi, K. Yamashita, Journal of Materials Chemistry A, 3 (2015) 8981-8991.

[104] Q. Xue, Z. Hu, J. Liu, J. Lin, C. Sun, Z. Chen, C. Duan, J. Wang, C. Liao, W.M. Lau, F. Huang, H.-L. Yip, Y. Cao, Journal of Materials Chemistry A, 2 (2014) 19598-19603.

[105] P.V. Braun, S.A. Rinne, F. Garcia-Santamaria, Adv. Mater., 18 (2006) 2665.

[106] L. Bechger, P. Lodahl, W.L. Vos, J. Phys. Chem. B, 109 (2005) 9980-9988.

[107] L. Berti, M. Cucini, F. Di Stasio, D. Comoretto, M. Galli, F. Marabelli, N. Manfredi, C. Marinzi, A. Abbotto, J. Phys. Chem. C, 114 (2010) 2403-2413.

[108] F. Di Stasio, L. Berti, M. Burger, F. Marabelli, S. Gardin, T. Dainese, R. Signorini, R. Bozio, D. Comoretto, Phys. Chem. Chem. Phys., 11 (2009) 11515-11519.

[109] D. Comoretto, V. Robbiano, G. Canazza, L. Boarino, G. Panzarasa, M. Laus, K. Sparnacci, Polymer Composites, 34 (2013) 1443-1450.

[110] F. Di Stasio, L. Berti, S.O. McDonnell, V. Robbiano, H.L. Anderson, D. Comoretto, F. Cacialli, APL Materials, 1 (2013) 042116.

[111] F. Jin, C. Li, X. Dong, W. Chen, X. Duan, Appl. Phys. Lett., (2006) 241101.

[112] V. Morandi, F. Marabelli, V. Amendola, M. Meneghetti, D. Comoretto, Adv. Func. Mater., 17 (2007) 2770-2786.

[113] V. Robbiano, M. Giordano, C. Martella, F. Di Stasio, D. Chiappe, F.B. de Mongeot, D. Comoretto, Advanced Optical Materials, 1 (2013) 389-396.

[114] J. Grüner, F. Cacialli, R.H. Friend, Journal of Applied Physics, 80 (1996) 207-215.

[115] G.R. Hayes, F. Cacialli, R.T. Phillips, Physical Review B, 56 (1997) 4798-4801.

[116] F. Cacialli, G.R. Hayes, J. Grüner, R.T. Phillips, R.H. Friend, Synthetic Metals, 84 (1997) 533-534.

[117] A.M. Ruminski, G. Barillaro, E. Secret, W.D. Huang, A. Potocny, U. Carion, C. Wertans, M.J. Sailor, Advanced Optical Materials, 1 (2013) 510-516.

[118] C.D. Presti, A. Irrera, G. Franzò, I. Crupi, F. Priolo, F. Iacona, G. Di Stefano, A. Piana, D. Sanfilippo, P.G. Fallica, Applied Physics Letters, 88 (2006) -.

[119] M. Galli, A. Politi, M. Belotti, D. Gerace, M. Liscidini, M. Patrini, L.C. Andreani, M. Miritello, A. Irrera, F. Priolo, Y. Chen, Applied Physics Letters, 88 (2006) -.

[120] N.A. Tokranova, S.W. Novak, J. Castracane, I.A. Levitsky, The Journal of Physical Chemistry C, 117 (2013) 22667-22676.

[121] V.S.-Y. Lin, K. Motesharei, K.-P.S. Dancil, M.J. Sailor, M.R. Ghadiri, Science, 278 (1997) 840-843.

[122] A.M. Ruminski, M.M. Moore, M.J. Sailor, Advanced Functional Materials, 18 (2008) 3418-3426.

[123] A.M. Ruminski, G. Barillaro, C. Chaffin, M.J. Sailor, Advanced Functional Materials, 21 (2011) 1511-1525.

[124] S. Surdo, S. Merlo, F. Carpignano, L.M. Strambini, C. Trono, A. Giannetti, F. Baldini, G. Barillaro, Lab on a Chip, 12 (2012) 4403-4415.

[125] K.A. Kilian, T. Böcking, K. Gaus, M. Gal, J.J. Gooding, ACS Nano, 1 (2007) 355-361.

[126] K.A. Kilian, L.M.H. Lai, A. Magenau, S. Cartland, T. Böcking, N. Di Girolamo, M. Gal, K. Gaus, J.J. Gooding, Nano Letters, 9 (2009) 2021-2025.

[127] S. Ciampi, T. Böcking, K.A. Kilian, J.B. Harper, J.J. Gooding, Langmuir, 24 (2008) 5888-5892.

[128] R. Hérino, Materials Science and Engineering: B, 69–70 (2000) 70-76.

[129] F.A. Harraz, M.S. Salem, T. Sakka, Y.H. Ogata, Electrochimica Acta, 53 (2008) 3734-3740.

[130] E. Segal, L.A. Perelman, F. Cunin, F. Di Renzo, J.M. Devoisselle, Y.Y. Li, M.J. Sailor, Advanced Functional Materials, 17 (2007) 1153-1162.

[131] G. Polito, S. Surdo, V. Robbiano, G. Tregnago, F. Cacialli, G. Barillaro, Advanced Optical Materials, 1 (2013) 894-898.

[132] M.S. Salem, M.J. Sailor, T. Sakka, Y.H. Ogata, Journal of Applied Physics, 101 (2007) 063503.

[133] W.L. Vos, R. Sprik, A.v. Blaaderen, A. Imhof, A. Lagendijk, G.H. Wegdam, Phys. Rev. B, 53 (1996) 16231.

[134] C.M. Ramsdale, N.C. Greenham, Journal of Physics D: Applied Physics, 36 (2003) L29.

[135] T. Jalkanen, V. Torres-Costa, E. Mäkilä, M. Kaasalainen, R. Koda, T. Sakka, Y.H. Ogata, J. Salonen, ACS Applied Materials & Interfaces, 6 (2014) 2884-2892.

[136] I.S. Nikolaev, P. Lodahl, W.L. Vos, Physical Review A, 71 (2005) 053813.

[137] E. Pavarini, L.C. Andreani, C. Soci, M. Galli, F. Marabelli, Physical Review B, 72 (2005) 045102.

[138] C. Soci, D. Comoretto, F. Marabelli, D. Moses, Physical Review B, 75 (2007) 11.

[139] L.P. Lu, D. Kabra, R.H. Friend, Advanced Functional Materials, 22 (2012) 4165-4171.

[140] B.-G. Kang, H. Kang, N.-G. Kang, C.-L. Lee, K. Lee, J.-S. Lee, Polymer Chemistry, 4 (2013) 969-977.

[141] J.-S. Kim, R.H. Friend, I. Grizzi, J.H. Burroughes, Applied Physics Letters, 87 (2005) 023506.

[142] G.M. Lazzerini, S. Mian, F. Di Stasio, A. Merari Masillamani, N. Crivillers, F. Reinders, M. Mayor, P. Samorì, F. Cacialli, Applied Physics Letters, 101 (2012) 153306.

[143] A. Petrozza, S. Brovelli, J.J. Michels, H.L. Anderson, R.H. Friend, C. Silva, F. Cacialli, Advanced Materials, 20 (2008) 3218-3223.

[144] G.M. Lazzerini, F. Di Stasio, C. Fléchon, D.J. Caruana, F. Cacialli, Applied Physics Letters, 99 (2011) 243305.

[145] M. Barth, A. Gruber, F. Cichos, Physical Review B, 72 (2005) 10.

[146] G. Mayonado, S. Mian, V. Robbiano, F. Cacialli, BFY Conference on Laboratory Instruction Beyond the First Year of College, College Park, MD, 2015, pp. 60-63.

[147] D. Cavallo, D. Comoretto, Self-Assembly of Polyelectrolytes for Photonic Crystal Applications, Ionic Interactions in Natural and Synthetic Macromolecules, John Wiley & Sons, Inc.2012, pp. 727-760.

[148] G.I.N. Waterhouse, M.R. Waterland, Polyhedron, 26 (2007) 356-368.

[149] D. Antonioli, S. Deregibus, G. Panzarasa, K. Sparnacci, M. Laus, L. Berti, L. Frezza, M. Gambini, L. Boarino, E. Enrico, D. Comoretto, Polymer International, 61 (2012) 1294-1301.

[150] K. Sparnacci, D. Antonioli, S. Deregibus, M. Laus, T. Poggio, V. Kapeliouchko, G. Palamone, G. Zuccheri, R. Passeri, Macromolecules, 42 (2009) 3518-3524.

[151] V. Morandi, F. Marabelli, V. Amendola, M. Meneghetti, D. Comoretto, Adv. Funct. Mater., 17 (2007) 2779-2786.

[152] P. Lodhal, A.F. vanDriel, I.S. Nikolaev, A. Irman, K. Overgaag, D. Vanmaekelbergh, W.L. Vos, Nature, 430 (2004) 654.

[153] L. Berti, M. Cucini, F. Di Stasio, D. Comoretto, M. Galli, F. Marabelli, N. Manfredi, C. Marinzi, A. Abbotto, J. Phys. Chem. C, 114 (2010) 2403-2413.

[154] F. Wooten, Optical properties of solids, Academic Press, Department of Applied Science, University of California, Davis, California, 1972.

[155] F. Cacialli, J.S. Wilson, J.J. Michels, C. Daniel, C. Silva, R.H. Friend, N. Severin, P. Samori, J.P. Rabe, M.J. O'Connell, P.N. Taylor, H.L. Anderson, Nat Mater, 1 (2002) 160-164.

[156] S. Brovelli, F. Cacialli, Small, 6 (2010) 2796-2820.

[157] S. Brovelli, G. Latini, M.J. Frampton, S.O. McDonnell, F.E. Oddy, O. Fenwick, H.L. Anderson, F. Cacialli, Nano Lett., 8 (2008) 4546-4551.

[158] F.E. Oddy, S. Brovelli, M.T. Stone, E.J.F. Klotz, F. Cacialli, H.L. Anderson, J. Mater. Chem., 19 (2009) 2846-2852.

[159] J.S. Wilson, M.J. Frampton, J.J. Michels, L. Sardone, G. Marletta, R.H. Friend, P. Samorì, H.L. Anderson, F. Cacialli, Adv. Mater., 17 (2005) 2659-2663.

[160] B. Fuhrmann, H.S. Leipner, H.-R. Höche, L. Schubert, P. Werner, U. Gösele, Nano Lett., 5 (2005) 2524-2527.

[161] N.W. Ashcroft, N.D. Mermin, Solid state physics, Saunders College Publishing, Philadelphia, 1976.

[162] F. Garcia-Santamaria, J.F. Galisteo-Lopez, P.V. Braun, C. Lopez, Phys. Rev. B, 71 (2005) 195112.

[163] A.S. Dimitrov, K. Nagayama, Langmuir, 12 (1996) 1303.

[164] B. O'Regan, M. Gratzel, Nature, 353 (1991) 737-740.

[165] A. Fujishima, K. Honda, Nature, 238 (1972) 37-38.

[166] F. Scotognella, A. Monguzzi, M. Cucini, F. Meinardi, D. Comoretto, R. Tubino, Int. J. Photoen., 2008 (2008) 389034.

[167] K. Yoshino, S. Tatsuhara, Y. Kawagishi, M. Ozaki, A.A. Zakhidov, Z.V. Vardeny, Appl. Phys. Lett., 74 (1999) 2590-2592.

[168] Y.R. Do, Y.-C. Kim, Y.-W. Song, Y.-H. Lee, J. Appl. Phys., 96 (2004) 7629-7636.

[169] X.-B. Shi, M. Qian, Z.-K. Wang, L.-S. Liao, Appl. Phys. Lett., 106 (2015) 223301.

[170] A. Mihi, M. Bernechea, D. Kufer, G. Konstantatos, Advanced Optical Materials, 1 (2013) 194-194.

[171] A. Mihi, M.E. Calvo, J.A. Anta, H. Miguez, J. Phys. Chem. C, 112 (2007) 13-17.

[172] A. Bozzola, V. Robbiano, K. Sparnacci, G. Aprile, L. Boarino, A. Proto, R. Fusco, M. Laus, L.C. Andreani, D. Comoretto, Advanced Optical Materials, 4 (2016) 147-155.

[173] M.T. Horantner, W. Zhang, M. Saliba, K. Wojciechowski, H.J. Snaith, Energy & Environmental Science, 8 (2015) 2041-2047.

[174] H.-S. Kim, C.-R. Lee, J.-H. Im, K.-B. Lee, T. Moehl, A. Marchioro, S.-J. Moon, R. Humphry-Baker, J.-H. Yum, J.E. Moser, M. Grätzel, N.-G. Park, Scientific Reports, 2 (2012) 591.

[175] C.-H. Chiang, C.-G. Wu, Nat Photon, 10 (2016) 196-200.

[176] J.M. Ball, M.M. Lee, A. Hey, H.J. Snaith, Energy & Environmental Science, 6 (2013) 1739-1743.

[177] M. He, D. Zheng, M. Wang, C. Lin, Z. Lin, Journal of Materials Chemistry A, 2 (2014) 5994-6003.

[178] J. Zhang, Y. Li, X. Zhang, B. Yang, Adv. Mater., 22 (2010) 4249-4269.

[179] P.N. Bartlett, J.J. Baumberg, P.R. Birkin, M.A. Ghanem, M.C. Netti, Chem. Mater., 14 (2002) 2199-2208.

[180] A. Mihi, M. Ocaña, H. Míguez, Adv. Mater., 18 (2006) 2244-2249.

[181] L.N.D. Kallepalli, C. Constantinescu, P. Delaporte, O. Utéza, D. Grojo, Journal of Colloid and Interface Science, 446 (2015) 237-243.

[182] M. Addamo, M. Bellardita, A. Di Paola, L. Palmisano, Chem. Commun., (2006) 4943-4945.

[183] V.M. Burlakov, G.E. Eperon, H.J. Snaith, S.J. Chapman, A. Goriely, Appl. Phys. Lett., 104 (2014) 091602.

[184] S. Mastroianni, F.D. Heinz, J.H. Im, W. Veurman, M. Padilla, M.C. Schubert, U. Wurfel, M. Gratzel, N.G. Park, A. Hinsch, Nanoscale, 7 (2015) 19653-19662.

[185] P. Qin, M. Paulose, M.I. Dar, T. Moehl, N. Arora, P. Gao, O.K. Varghese, M. Grätzel, M.K. Nazeeruddin, Small, 11 (2015) 5533-5539.

[186] K. Miyano, N. Tripathi, M. Yanagida, Y. Shirai, Accounts of Chemical Research, 49 (2016) 303-310.

[187] E.L. Unger, E.T. Hoke, C.D. Bailie, W.H. Nguyen, A.R. Bowring, T. Heumuller, M.G. Christoforo, M.D. McGehee, Energy & Environmental Science, 7 (2014) 3690-3698.

[188] H.J. Snaith, A. Abate, J.M. Ball, G.E. Eperon, T. Leijtens, N.K. Noel, S.D. Stranks, J.T.-W. Wang, K. Wojciechowski, W. Zhang, The Journal of Physical Chemistry Letters, 5 (2014) 1511-1515.

[189] V. Robbiano, A. Abdellah, L. Santarelli, A. Falco, S. El-Molla, L.V. Titova, D.N. Purschke, F.A. Hegmann, F. Cacialli, P. Lugli, Nanotechnology (IEEE-NANO), 2014 IEEE 14th International Conference on2014, pp. 650-654.

[190] M.S. White, M. Kaltenbrunner, E.D. Glowacki, K. Gutnichenko, G. Kettlgruber, I. Graz, S. Aazou, C. Ulbricht, D.A.M. Egbe, M.C. Miron, Z. Major, M.C. Scharber, T. Sekitani, T. Someya, S. Bauer, N.S. Sariciftci, Nat Photon, 7 (2013) 811-816.

[191] Q. Cao, J.A. Rogers, Adv. Mater., 21 (2009) 29-53.

[192] G. Gruner, J. Mater. Chem., 16 (2006) 3533-3539.

[193] L. Hu, D.S. Hecht, G. Grüner, Chemical Reviews, 110 (2010) 5790-5844.

[194] D. Zhang, K. Ryu, X. Liu, E. Polikarpov, J. Ly, M.E. Tompson, C. Zhou, Nano Lett., 6 (2006) 1880-1886.

[195] C. Yu-Mo, L. Florent, S. Ishiang, I. Ricardo, Nanotechnology, 21 (2010) 134020.

[196] R.C. Tenent, T.M. Barnes, J.D. Bergeson, A.J. Ferguson, B. To, L.M. Gedvilas, M.J. Heben, J.L. Blackburn, Adv. Mater., 21 (2009) 3210-3216.

[197] A.K.K. Kyaw, H. Tantang, T. Wu, L. Ke, C. Peh, Z.H. Huang, X.T. Zeng, H.V. Demir, Q. Zhang, X.W. Sun, Appl. Phys. Lett., 99 (2011) 021107.

[198] K. Aung Ko Ko, T. Hosea, W. Tao, K. Lin, W. Jun, D. Hilmi Volkan, Z. Qichun, S. Xiao Wei, Journal of Physics D: Applied Physics, 45 (2012) 165103.

[199] R.A. Hatton, N. Blanchard, L.W. Tan, G. Latini, F. Cacialli, S.R.P. Silva, Organic Electronics, 10 (2009) 388-395.

[200] M. Ha, Y. Xia, A.A. Green, W. Zhang, M.J. Renn, C.H. Kim, M.C. Hersam, C.D. Frisbie, ACS Nano, 4 (2010) 4388-4395.

[201] C. Wang, J. Zhang, C. Zhou, ACS Nano, 4 (2010) 7123-7132.

[202] J. Li, Y. Lu, Q. Ye, M. Cinke, J. Han, M. Meyyappan, Nano Lett., 3 (2003) 929-933.

[203] M. Penza, R. Rossi, M. Alvisi, G. Cassano, E. Serra, Sensors and Actuators B: Chemical, 140 (2009) 176-184.

[204] T.M. Brown, G.M. Lazzerini, L.J. Parrott, V. Bodrozic, L. Bürgi, F. Cacialli, Organic Electronics, 12 (2011) 623-633.

[205] J.S. Kim, M. Granström, R.H. Friend, N. Johansson, W.R. Salaneck, R. Daik, W.J. Feast, F. Cacialli, J. Appl. Phys., 84 (1998) 6859-6870.

[206] T.M. Brown, J.S. Kim, R.H. Friend, F. Cacialli, R. Daik, W.J. Feast, Appl. Phys. Lett., 75 (1999) 1679-1681.

[207] B. de Boer, A. Hadipour, M.M. Mandoc, T. van Woudenbergh, P.W.M. Blom, Adv. Mater., 17 (2005) 621-625.

[208] N. Crivillers, S. Osella, C. Van Dyck, G.M. Lazzerini, D. Cornil, A. Liscio, F. Di Stasio, S. Mian, O. Fenwick, F. Reinders, M. Neuburger, E. Treossi, M. Mayor, V. Palermo, F. Cacialli, J. Cornil, P. Samorì, Advanced Materials, 25 (2013) 432-436.

[209] C.-Y. Chen, K.-Y. Wu, Y.-C. Chao, H.-W. Zan, H.-F. Meng, Y.-T. Tao, Organic Electronics, 12 (2011) 148-153.

[210] Y. Zhou, C. Fuentes-Hernandez, J. Shim, J. Meyer, A.J. Giordano, H. Li, P. Winget, T. Papadopoulos, H. Cheun, J. Kim, M. Fenoll, A. Dindar, W. Haske, E. Najafabadi, T.M. Khan, H. Sojoudi, S. Barlow, S. Graham, J.-L. Brédas, S.R. Marder, A. Kahn, B. Kippelen, Science, 336 (2012) 327-332.

[211] F. Bausi, A. Schlierf, E. Treossi, M.G. Schwab, V. Palermo, F. Cacialli, Organic Electronics, 18 (2015) 53-60.

[212] L. Yan, Y. Song, Y. Zhou, B. Song, Y. Li, Organic Electronics, 17 (2015) 94-101.

[213] Z. Lin, J. Chang, J. Zhang, C. Jiang, J. Wu, C. Zhu, Journal of Materials Chemistry A, 2 (2014) 7788-7794.

[214] A. Abdellah, A. Yaqub, C. Ferrari, B. Fabel, P. Lugli, G. Scarpa, Nanotechnology (IEEE-NANO), 2011 11th IEEE Conference on2011, pp. 1118-1123.

[215] A. Abdellah, B. Fabel, P. Lugli, G. Scarpa, Organic Electronics, 11 (2010) 1031-1038.

[216] T. Teruo, T. Katsunori, Y. Hirofumi, I. Tadahiro, Japanese Journal of Applied Physics, 43 (2004) 3636.

[217] H.A. Atwater, A. Polman, Nat Mater, 9 (2010) 205-213.

[218] A. Zampetti, A.H. Fallahpour, M. Dianetti, L. Salamandra, F. Santoni, A. Gagliardi, M. Auf der Maur, F. Brunetti, A. Reale, T.M. Brown, A. Di Carlo, J. Polym. Sci. B: Polym. Phys., (2015) n/a-n/a.

[219] K. Ki-Beom, T. Yoon-Heung, H. Yoon-Soo, B. Kwang-Heum, Y. Myung-Hee, L. Moon-Ho, Japanese Journal of Applied Physics, 42 (2003) L438.

[220] G. Kavei, A.M. Gheidari, Journal of Materials Processing Technology, 208 (2008) 514-519.

[221] A. Naeemi, J.D. Meindl, IEEE Electron Device Letters, 28 (2007) 135-138.

[222] E. Pop, D.A. Mann, K.E. Goodson, H. Dai, Journal of Applied Physics, 101 (2007) 093710.

[223] S. Datta, Quantum Transport: Atom to Transistor, Cambridge University Press, Cambridge, 2005.

[224] A.A. Odintsov, Phys. Rev. Lett., 85 (2000) 150-153.

[225] J.W. Mintmire, C.T. White, Phys. Rev. Lett., 81 (1998) 2506-2509.

[226] T.M. Barnes, J.L. Blackburn, J. van de Lagemaat, T.J. Coutts, M.J. Heben, ACS Nano, 2 (2008) 1968-1976.

[227] L. Zhou, M.R. Zachariah, Chem. Phys. Lett., 525–526 (2012) 77-81.

[228] G. Heimel, L. Romaner, J.-L. Brédas, E. Zojer, Physical Review Letters, 96 (2006) 196806.

[229] C.B. René, S. Michael, K.H. Harold, Journal of Physics B: Atomic, Molecular and Optical Physics, 31 (1998) 3885.

[230] F. Buonocore, F. Trani, D. Ninno, A.D. Matteo, G. Cantele, G. Iadonisi, Nanotechnology, 19 (2008) 025711.